Simulation of Joule-Thomson Throttling of Gases

by

Amanda Bailey Hass

Thesis

for the award of

DOCTOR OF PHILOSOPHY

Supervised by Dr. Karl P. Travis

Department of Material Science and Engineering

University of Sheffield

9th of April 2019

"It's not a silly question if you can't answer it."

- Jostein Gaarder

Acknowledgements

Contents

List of Figures

List of Tables

Abstract

A complete general theory for non-equilibrium states is currently lacking. Non-equilibrium states are hard to reproduce experimentally, but creating computer simulations of relatively simple and non-equilibrium systems can act as a 'numerical laboratory', in which to study steady states far away from equilibrium.

The Joule-Thomson throttling experiment, being a system driven away from equilibrium during the throttling, was first performed by Lord Kelvin and Joule in 1852. They successfully cooled a gas in an adiabatic process. This study investigates the simulation of a Joule-Thomson throttling proposed by Hoover, Hoover and Travis (2014), who used a purely repulsive potential and successfully observed cooling. This was puzzling, as Van der Waals had noted that the Joule-Thomson experiment proved the presence of intermolecular attractive forces. It was found that the original simulation did not conserve enthalpy, which is a requirement of a Joule-Thomson throttling.

This study proposes the use of two families of pair potentials: the mn-family, first defined by Hoover and the LJ/s first defined by Holian and Evans. These potentials offer an attractive component, while being well suited for molecular dynamics simulations, by being continuous in its derivatives and smooth without the need for further corrections.

The phase diagrams for these potentials are unknown, but are required to perform a successful throttling. This study develops two methods of predicting liquid-vapour coexistence and Joule-Thomson inversion curves without any a priori knowledge of the phase diagram: (i) Virial coefficient theory and (ii) a Barker-Henderson perturbation theory.

The theories successfully predicted liquid-vapour coexistence and Joule-Thomson inversion curves for a range of members of each family in two and three dimensions. One potential was then selected, and used to perform a two dimensional Joule-Thomson throttling, which displayed cooling of the gas while keeping the enthalpy constant.

1 Introduction and Literature Survey

Thermodynamics is well established for systems at equilibrium, but in practice, particularly in engineering, many systems are never truly in equilibrium, but can be very far from it. However, some systems can attain a non-equilibrium steady state. A complete generalised theory of systems far from equilibrium is currently lacking. The main reason for this is a lack of well-defined experimental data for such systems. Non-equilibrium steady states are extremely rare in nature and hard to reproduce experimentally. Numerical simulation offers the best hope for making progress. To make advances in theoretical knowledge, there is a need to find systems far away from equilibrium which can be reproduced using computer simulations. Atomistic simulation methods such as Molecular Dynamics (MD) are essentially exact once a pair potential has been supplied. These methods can be regarded as numerical laboratories, supplying pseudo-experimental data with which to test new theories and advance knowledge.

1.1 Motivation: NEMD Simulations

The study of low dimensional systems is the study of systems where the movement of particles are severely restricted in one or more dimensions. A few general examples include: a two dimensional system like the 2D electron gas [1], graphene [2, 3], carbon nano tubes [4] and Langmuir-Blodgett films [5], the one dimensional system of a nano wire [6] and a zero dimensional system, the quantum dot [7]. Studies of low dimensional systems such as these have led to many advances in electronics, for example the understanding of light and molecules.

A single 1D Nosé-Hoover oscillator particle subjected to a coordinate dependent temperature $T(q)$ provides another example of a non-equilibrium steady state with low dimensionality which can result in chaotic behaviour [8].

The Galton Board, described by Francis Galton in his work *Natural Inheritance* [9, 10], is a simple experiment which illustrates how the chaotic movement of balls through several rows of pegs results in a normal distribution, as illustrated in figure

1.1. This system is of interest because it can be used to simulate a dilute electron gas in a metal, the periodic Lorentz gas [11, 12].
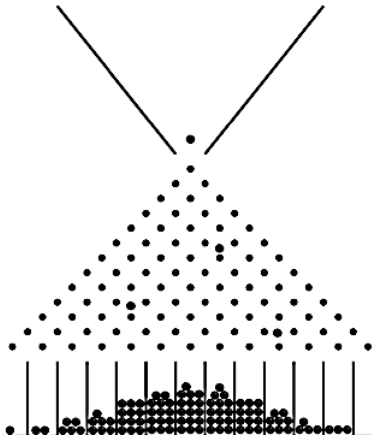
Figure 1.1: Illustration of the Galton Board, showing the resulting normal distribution [9, 10].
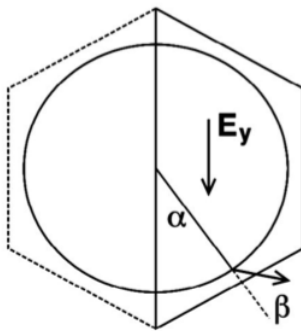
Figure 1.2: Diagram showing the computational cell with two outgoing angles α and β, when interacting with a single peg on the Galton board, while being in an applied external field in the y-direction [13].

A simple two dimensional computational realisation of the Galton Board uses hard disks in place of the pegs and a single point mass in place of the ball bearing. Like the real model, the computational variant has an applied external field (not necessarily gravitational). A deterministic thermostat completes the description of the computer model, preventing infinite acceleration and necessary to generate a NESS (Non Equilibrium Steady State).

Perhaps the simplest numerical Galton Board is the one conceived by Hoover [13]. Here, a triangular lattice of scatters is employed, with the field direction chosen as per figure 1.2. The thermostatted equations of motion for the position, $\mathbf{r}$, and momentum, $\mathbf{p}$, describing the motion of a point mass *between* collisions are:

$$\dot{\mathbf{r}} = \frac{\mathbf{p}}{m} \tag{1.1}$$

$$\dot{\mathbf{p}} = E_y\hat{\mathbf{i}} - \zeta\mathbf{p} \tag{1.2}$$

where E_y is the field strength and ζ is a Gaussian multiplier. This formulation avoids the need to include impulsive forces which operate at collisions where the hard disk scatters.

In two physical dimensions, there are four degrees of freedom but the thermostat reduces this to three because $p_x^2 + p_y^2 = \text{const}$. By using a Poincaré section, the phase space reduces to two dimensional. By following the trajectory of a randomly placed diffusant in time, the phase space distribution function can be obtained. Applying the field as discussed above, the simulation can be performed using only a half-hexagonal unit cell with the standard edge periodic boundaries, and the surface of an elastic semicircle (which represents one of the scattering particles). Changing from Cartesian to polar coordinates leads to an analytical solution for the free flight trajectories [11]. However, it is far simpler to work in Cartesian coordinates and obtain the trajectories numerically.
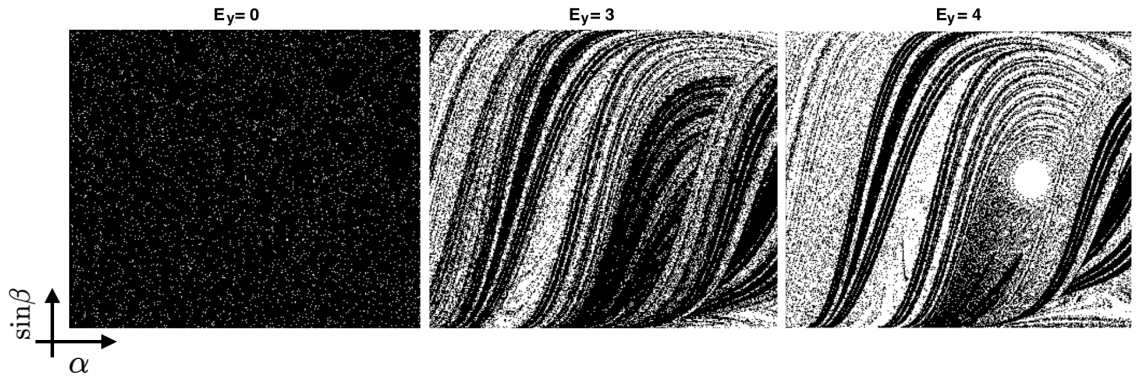
Figure 1.3: Phase space at different magnitudes of applied external fields of the Galton Board. α, β, p_z and past collision angles defined in figure 1.2 [14].

Figure 1.3 shows the reduced phase space distribution obtained using this model. The zero force field case shows a uniform coverage. With the field switched on, the phase space becomes striped with a fractal dimensionality that depends on E_y. This result implies that the Gibbs fine grained entropy, defined as

$$S = -k_B \int f(\Gamma) \ln f(\Gamma) d\Gamma \tag{1.3}$$

where $f(\Gamma)$ is the the probability distribution of all points Γ in phase space. It diverges to $-\infty$ because the phase space distribution function is multi fractal, meaning it has more than one scaling exponent. This result suggests it is futile to seek to develop a theory of NESS based on generalising linear irreversible thermodynamics [14].

An example of a NESS generated for a many-body system is provided by the simulation of planar Poiseuille flow, which is shown in figure 1.4. By using a constant
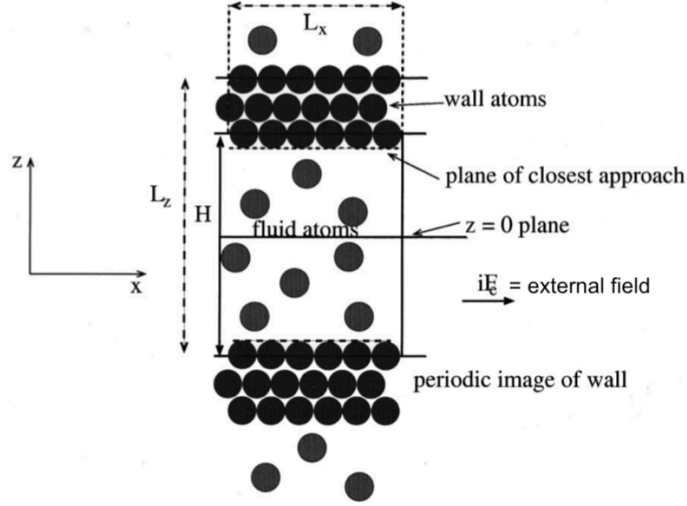
Figure 1.4: Simulation geometry for the planar Poiseuille flow [15].

applied field in the flow direction, Travis and Gubbins [16] were able to generate Poiseuille flow with a homogenous longitudinal pressure and density. Using the method of planes [17] they obtained local profiles with high spatial resolution. The strain rate profile was found to contain several zeros, this is shown in figure 1.5.

This result indicates that even a local generalisation of Newton's law of viscosity, as given in equation (1.4) is incorrect.

$$\eta(z) = \frac{-\Pi_{yx}(z)}{\gamma(z)} \tag{1.4}$$

Where η is the viscosity, Π the stress and γ the strain. Instead they postulated a

<table>
<tr><td>(a)</td><td>(b)</td></tr>
</table>
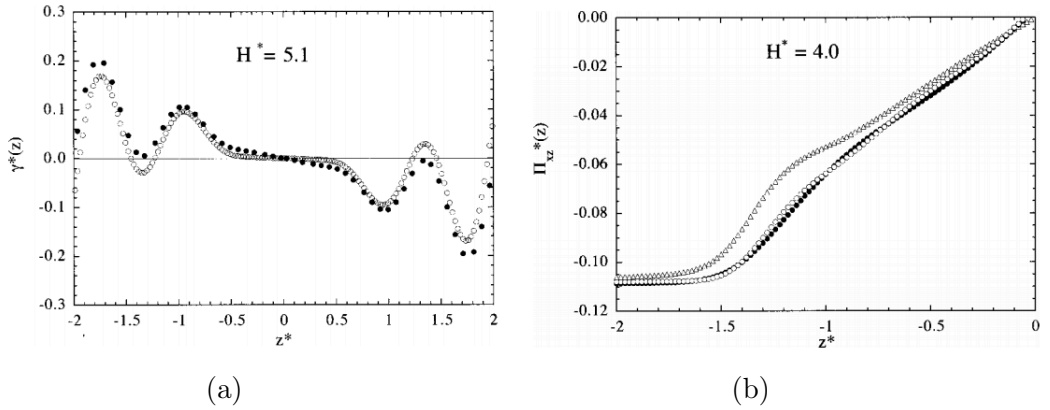
Figure 1.5: Where the vertical axes are strain rate $\gamma^*(z)$ at channel width $H* = 5.1$ and $\Pi^*(z)$ is stress, both in the reduced z* direction. The diagrams are: (a) Strain and (b) stress profiles for different systems: Weeks-Chandler-Anderson (filled circles), Lennard-Jones (open circles) and Weeks-Chandler-Anderson (fluid-fluid/solid-solid) and Lennard-Jones (fluid-solid) (open triangles) [15]. (see section 2 for more information on these potentials.)

non-local generalisation of Newton's law in the form of equation (1.5).

$$\Pi_{xz}(x) = -\int_0^z \eta(z; z - z')\gamma(z')dz' \qquad (1.5)$$

where $\gamma(z) = \partial u_x/\partial z$. Later work by Daivis, Todd and Travis [18] and Daivis and Todd [19] confirmed this generalised form of Newton's law.

A shock wave is a strong pressure wave propagating through an elastic medium such as air, water or solid. The wave front in a shock wave has a drastic change in stress, density and temperature. In figure 1.6, the density profile of a typical one dimensional shock wave from an MD simulation, propagating from left to right is shown [20]. It is shown that a low density region is following a higher density as the wave propagates. In reality, such a pressure wave can be caused by supersonic aircrafts, explosions and lightning. Simulating a shock wave is of interest because it generates a far from equilibrium state after only a few collision times. Transforming a cold liquid or solid into a hot compressed state [20].

Studying shock waves, which are far away from equilibrium, Hoover and Hoover [21] showed that Fourier's law of heat conduction also needs generalising. They studied two dimensional shock waves using molecular dynamics (MD), which showed that temperature is not a scalar, and that there are time delays between heat flux

5
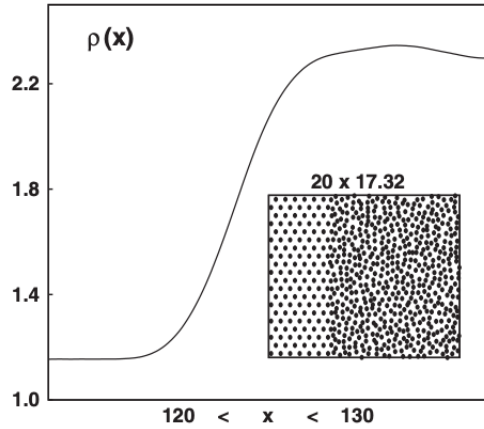
Figure 1.6: Density profile and snap shot from a typical 1D shock wave simulation [20]

and thermal gradient, as is shown in figure 1.7. A solution to temperature not being a scalar, is a modification of Fourier's law, where there are independent contributions from ∇T_{xx} and ∇T_{yy}.
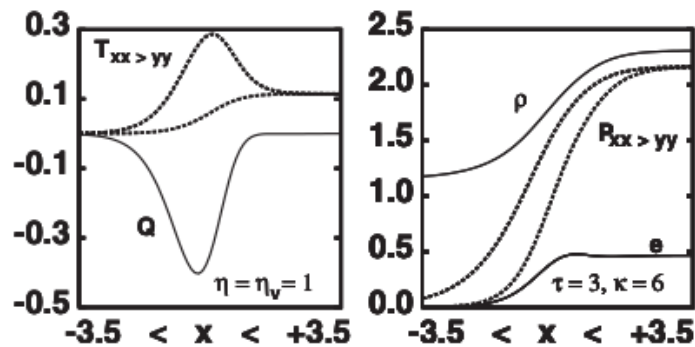
Figure 1.7: The y axis to the left is, from the top down: Temperature in the x-direction T_{xx}, temperature in the y-direction T_{yy} and heat flux Q. On the figure on the right the y-axis is, from the top down: density ρ, pressure in the x-direction and pressure in the y-direction. Solution of the generalised Navier-Stokes-Fourier equation, showing that temperature is not a scalar, as $T_{xx} > T_{yy}$, and that the heat flux Q only contributes to T_{xx} [22].

Hoover, Hoover and Travis [20] argued that the Joule Thomson effect could also be a simple system far away from equilibrium and could be used to study the breakdown of hydrodynamics.

1.1.1 Review of the Joule-Thomson effect

In 1852 Joule and Thomson discovered that it is possible to change the temperature in a gas by applying a sudden pressure change through a valve, later to be known

as the *Joule-Thomson effect* [23]. The experiment can simply be thought of as a cylinder which is thermally insulated and has an adiabatic piston at each end. In the middle of the cylinder is a porous plug as depicted in figure 1.8. The purpose of the porous plug is to enable the control of pressure while still allowing the flow of mass. Considering the initial state as seen in figure 1.8 (a), there is a gas with pressure P_i and volume V_i. The initial state can be considered to be in equilibrium, as the right hand piston prevents any gas from passing through the porous plug. The final state, as shown in figure 1.8 (b), is obtained by moving both pistons simultaneously to the right, in such a way that P_i is kept larger than P_f but both being constant, until all the gas has been passed through to the right hand side, when the system is now in a new equilibrium state.

(a) Initial state (b) Final state
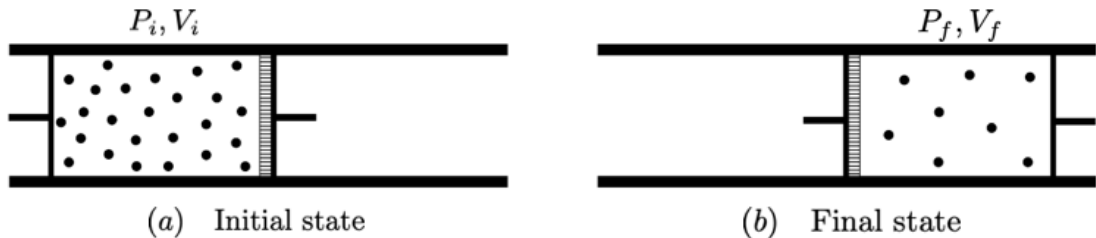
Figure 1.8: Experimental set-up for the Joule-Thomson throttling experiment, showing the initial and final states.

Whilst the pistons are moving the system is in a non-equilibrium state, and it cannot be described by thermodynamic coordinates. In contrast, since the initial and final states are in equilibrium, they can be described by thermodynamic coordinates. Consider the first law of thermodynamics, which states that the difference in final (U_f) and initial (U_i) internal energy is equal to the sum of the work done on the system (W) and the heat added to the system (Q)

$$\Delta U = Q + W \tag{1.6}$$

The cylinder is thermally insulated so that no heat enters or leaves the system, so that $Q = 0$. The work done on the pistons is given by the volume integral

$$W = -\int_0^{V_f} P_f dV - \int_{V_i}^0 P_i dV \tag{1.7}$$

Both pressures in the initial and final states are constant, so the result of the integral is simply

$$W = -(P_f V_f - P_i V_i) \tag{1.8}$$

Combining equations 1.6 and 1.8

$$(U_f - U_i) = -(P_f V_f - P_i V_i) \tag{1.9}$$

and rearranging so that all initial states are to the left, and final states to the right

$$U_i + P_i V_i = U_f + P_f V_f \tag{1.10}$$

In other words, the initial and final enthalpies are the same. It is worth noting that this does not imply that enthalpy remains constant during the non-equilibrium throttling process.

It is worth noting that for the most simple system, the ideal gas, constant enthalpy during throttling does not yield a drop in temperature. Recall that enthalpy is given by $H = U + PV$ and that for an ideal gas, the internal energy U is only dependent on temperature. By applying the equipartition theorem and the kinetic theory of particles, the internal energy of an ideal gas is written as

$$U = \frac{1}{2} N f k_B T \tag{1.11}$$

where N is the number of particles and f the number of active degrees of freedom. The ideal gas law

$$PV = N k_B T \tag{1.12}$$

yields an expression for the enthalpy of an ideal gas

$$H = \left(\frac{f+2}{2} \right) N k_B T \tag{1.13}$$

making the initial and finial enthalpies

$$H_i = H_f \tag{1.14a}$$

$$\left(\frac{f+2}{2}\right) N k_B T_i = \left(\frac{f+2}{2}\right) N k_B T_f \tag{1.14b}$$

Hence $T_i = T_f$, showing that for an ideal gas, if enthalpy is constant the temperature must also be constant. Therefore there will be no observed heating or cooling for a system where particles are not interacting, when being throttled.
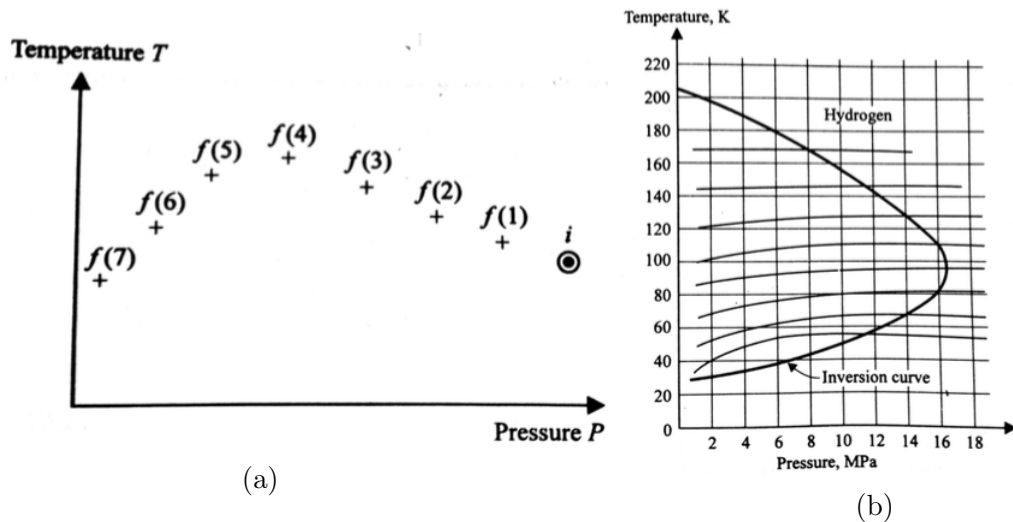
Figure 1.9: (a) A single isenthalp, showing its maximum. (b) A Joule-Thomson inversion curve superimposed on several isenthalps going through their maxima. Taken from the work of R. H. Pittman and M. W. Zemansky [24].

Now considering the Joule-Thomson throttling as an isenthalpic process, results for different rates of throttling from an initial state of pressure i and seven different final states of pressure, labelled $f(n)$, with $n = 1 \ldots 7$, are shown in figure 1.9a. As an illustrative example, full calculations of the JT inversion curve for the van der Waals system is given in appendix D. What one should note is that a throttling process can either result in an increase of the temperature ($n = [1; 6]$), or a decrease ($n = 7$). This phenomenon is described by the *Joule-Thomson coefficient* μ_{JT} and is the rate of change in temperature with changing pressure in an isenthalpic process.

$$\mu_{JT} = \left(\frac{\partial T}{\partial P}\right)_H \tag{1.15}$$

If $\mu_{JT} < 0$, heating will be observed while for $\mu_{JT} > 0$, cooling will be observed. For the purpose of performing a throttling with the desired result, knowing how to obtain cooling or heating is very useful. We can obtain this knowledge by finding the maxima of the isenthalps, i.e solving for when the Joule-Thomson coefficient vanishes. Repeating this calculation for several isenthalps gives rise to the *Joule-Thomson inversion curve*, as depicted for hydrogen in figure 1.9b. Hoover, Hoover and Travis [20] conducted a molecular dynamics (MD) simulation of the Joule-Thomson throttling, using a simple and purely repulsive pair potential $\phi(r < 1) = [1 - r^2]^4$ which was slightly modified by capping the force at the point of inflexion. Two regions of different density and pressure were separated by a potential barrier, which only allows particles with enough energy to overcome the barrier to pass through. Figure 1.10 shows the predicted density profile of the throttling process. The particles are driven from the left to the right, having the potential barrier placed directly in the middle of the system at $x = 0$. As expected, the density in the initial state is constant and the density in the final region is also constant but lower than the initial region.
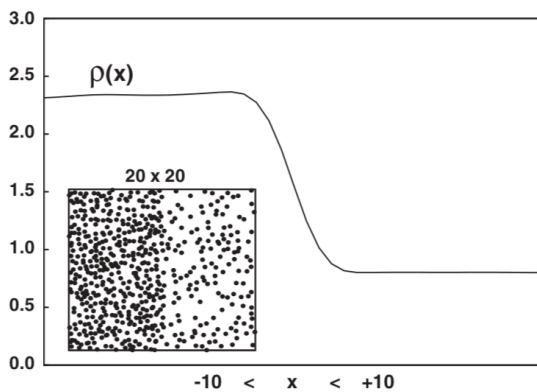
Figure 1.10: A Joule-Thomson snapshot. The motion is from left-to-right with cooled fluid exiting at the right boundary. Taken from *Hoover, Hoover & Travis (2014)*

Similarly, results in figure 1.11 for the remaining thermodynamic profiles show that pressure is constant in both regions, but $p_i > p_f$. Mass is kept constant throughout the system and there is a cooling observed in the temperature.

A puzzling feature of this work is the presence of a cooling effect despite the lack of attractive interactions in the pair potential for the fluid. The authors did not
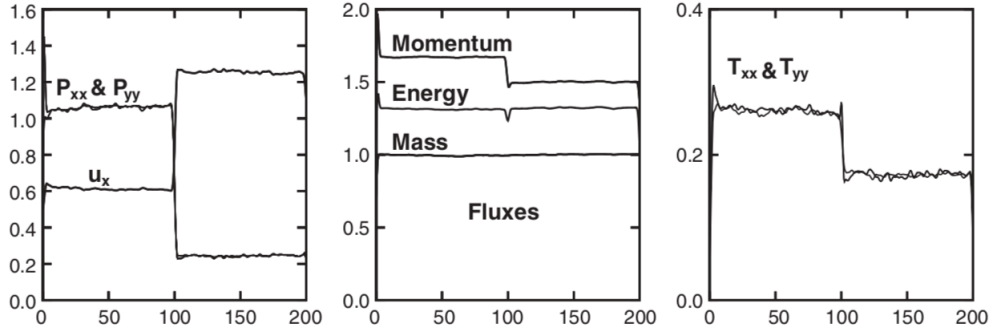
Figure 1.11: Time-averaged pressure tensor and velocity (left); time-averaged mass, momentum, and energy fluxes (centre); tensor temperature (right). Taken from Hoover, Hoover & Travis (2014).

explore this further.

Other simulation studies done in relation to the Joule-Thomson throttling are mainly aimed at determining the Joule-Thomson inversion curve. Empirical determination of inversion curves has to happen under extreme conditions, therefore there has not been much published experimental data for inversion curves. Simulations are not hindered by high temperatures and pressure and can therefore be used to obtain inversion curves. These curves are useful for testing equations of state and even predicting phase behaviour for real fluids in the critical region. Colina and Müller [25] performed an isothermal-isobaric Monte Carlo molecular simulation to obtain a Joule-Thomson inversion curve for the Lennard-Jones system. Kristóf *et al.* used a constant pressure and enthalpy Monte Carlo method (NPH-MC) to obtain the Lennard-Jones inversion curve. They produced isenthalps which were analysed to locate their maxima, which corresponds to $\mu_{LJ} = 0$.

In the original Joule-Thomson throttling experiment, the gas diffuses through a solid porous material, causing a decrease in the density of the gas. This effect is called permeation and has been simulated several times. Hoover, Hoover and Travis use 'conveyor belt' type boundary conditions [20] but other boundary driven simulations exist. Arya *et al.* [26] performed a molecular dynamic simulation of a permeating liquid, to obtain transport coefficients. Their simulated system consisted of a high and a low density region on either side of a porous material and by replacing molecules as they permeate they created a steady state. Furukawa *et*

al. [27] is another example of boundary driven non-equilibrium molecular dynamic simulations for a gas being forced through a porous material. They consider a flexible and an inflexible material as the porous material, to investigate what effect this has on the effusion flux. These simulations, like the Joule-Thomson simulation by Hoover, Hoover and Travis, rely on a streaming velocity and the insertion of new particles to maintain a flow. Furukawa *et al.* re-evaluated the streaming velocity after every 1000 MD time step, while Arya *et al.* maintains a constant replacement. The boundary conditions chosen by Furukawa *et al.* could seem like the better choice due to constant re-evaluation. However, the constant replacement of particles chosen by Arya *et al.* and Hoover, Hoover and Travis although simpler gives good results, as was proven by the 1D shock wave work [20]. It is worth noting that, despite the similarities, the Joule-Thomson simulation by Hoover, Hoover and Travis is independent of the structure of the porous material, even Joule and Thomson originally used several different materials and obtained the same results. What is important to the Joule-Thomson throttling is not the permeation itself, all this will do is increase the time it would take for a particle to reach the other side, rather it is the potential barrier particles experience before they enter the porous material.

Joule-Thompson throttling is a promising model for NEMD simulations to advance our understanding of far from equilibrium states. However, it requires a rethink of what potential to use. A suitable potential would be mathematically simple, have an attractive part and have a finite cut off to be useful for molecular dynamics simulations, as simulations can not truly consider infinite interactions. To ensure a successful throttling of a gas, it is important to know the chosen potential's phase diagram, in order to avoid throttling through the liquid-vapour coexistence region.

1.2   Literature Survey

First an overview is presented of some mathematically simple pair potentials which have been of interest for simulation purposes, from the simple purely repulsive hard

sphere potential, to the much softer Lennard-Jones. This is followed by an introduction to the purpose and meaning of phase diagrams and how to obtain them. This section concludes with a historical review of the development of analytical equations of state.

1.2.1 Pair potentials

In general, the particles of a system interact through conservative intermolecular forces. The total potential energy of a system can be written as a sum of one-body, two-body, three-body plus higher order terms, each of which depend on their coordinates [28–31]:

$$\Phi_{total} = \sum_i^N \Phi_1(\mathbf{r}_i) + \sum_{i,j}^N \Phi_2(\mathbf{r}_i, \mathbf{r}_j) + \sum_{i,j,k}^N \Phi_3(\mathbf{r}_i, \mathbf{r}_j, \mathbf{r}_k) + ... \quad (1.16)$$

The first term is zero in the absence of an external field (e.g gravity). The three body term is usually small compared to the two body term, so the total energy is often approximated by the two body term alone, the pair potential. The most significant part of the pair potential is the repulsion which occurs at short separation distances. The repulsion arises when there is an overlap of the outer electron shells. The attractive force dominates at larger separation distances and is significantly more slowly varying in comparison to the repulsion. The attraction has little impact on the structure of a fluid, but it does provide the cohesive energy which stabilises the liquid phase. Considering the importance of the repulsive part, the simplest possible pair potential is that of the hard sphere (HS).

The HS potential describes the repulsion between hard spherical particles that cannot overlap, imitating the behaviour of spherical molecules at very short distances [32]. If the particles are in contact (separation $= \sigma$) the energy becomes infinite, thus preventing any overlap. For separations greater than this, the energy is zero. The HS potential is given by

$$\phi_{HS}(r) = \begin{cases} \infty & r < \sigma \\ 0 & r \geq \sigma \end{cases} \quad (1.17)$$

and illustrated in figure 1.12.
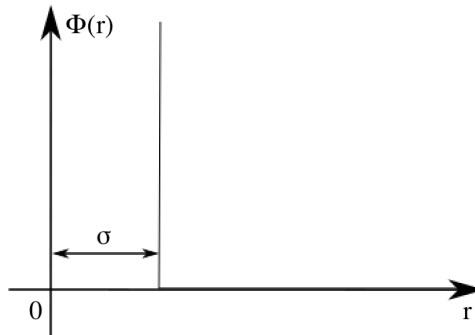
Figure 1.12: Hard sphere potential

Computational experiments using the HS potential have shown that there is no significant difference in the structure of the liquid, compared to calculations done using a more complicated, but still spherically symmetric potential [33–37]. The absence of any attractive force means that a HS system only has a single fluid phase [38], the HS potential therefore fails to describe a liquid phase.

By adding a small attraction to the HS potential, one obtains the square-well (SW) potential. Instead of the potential vanishing when $r = \sigma$, it takes a constant value of ϵ over the range $\sigma < r < \sigma(R-1)$ [39]. The SW potential is defined by

$$\phi_{SW}(r) = \begin{cases} \infty & r < \sigma \\ -\epsilon & \sigma \leq r \leq R\sigma \\ 0 & r > R\sigma \end{cases} \tag{1.18}$$

and depicted in figure 1.13.

In order to study and understand the effect of attractive forces, the hard-core repulsion of particles must be replaced with a softer repulsion. This allows the particles to overlap. The SW system has been well studied [40,41]. The SW potential does give rise to a true liquid. The structure of the square well lends itself to easy modifications in the attractive region, by changing the width of the well, the depth and the number of wells in the potential.

It is possible to combine a number of wells, to construct a stair like potential, as
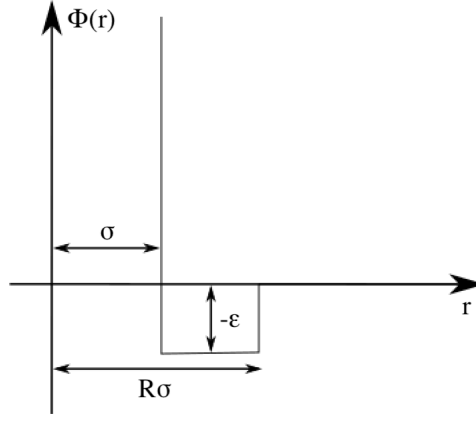
Figure 1.13: Square well pair potential

given by

$$
\phi_{Stair}(r) = \begin{cases} \infty & r < \sigma \\ \epsilon_0 & \sigma \leq r < r_0 \\ \epsilon_1 & r_0 \leq r < r_1 \\ \epsilon_2 & r_1 \leq r < r_2 \\ 0 & r \geq r_2 \end{cases} \tag{1.19}
$$

as depicted in figure 1.14 [42, 43]. This form has been used to simplify virial coefficients calculations for super critical fluids [44].
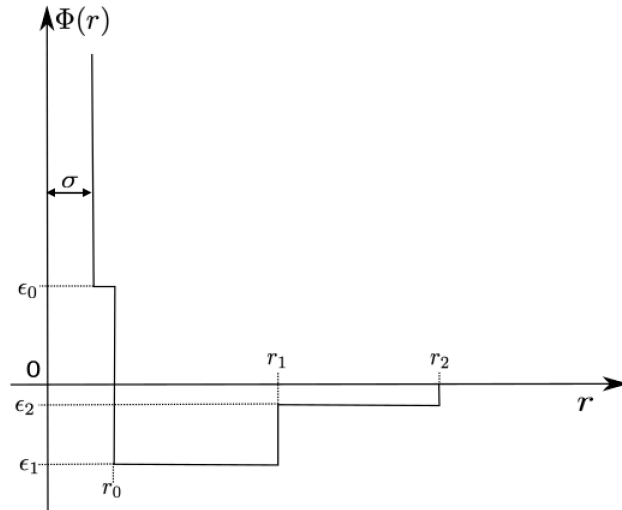
Figure 1.14: Four well potential.

A ramp shaped soft pair potential was proposed by Hemmer and Stell [45], where the steep repulsive core has been softened by a ramp. Such a potential is described

by

$$\phi_{Ramp}(r)/\epsilon = \begin{cases} \infty & r < r_0 \\ \frac{(r_0-r)}{(r_1-r_0)} & r_0 \leq r < r_1 \\ \frac{(r_2-r)}{(r_1-r_2)} & r_1 \leq r < r_2 \\ 0 & r \geq r_2 \end{cases} \tag{1.20}$$

and illustrated in figure 1.15.
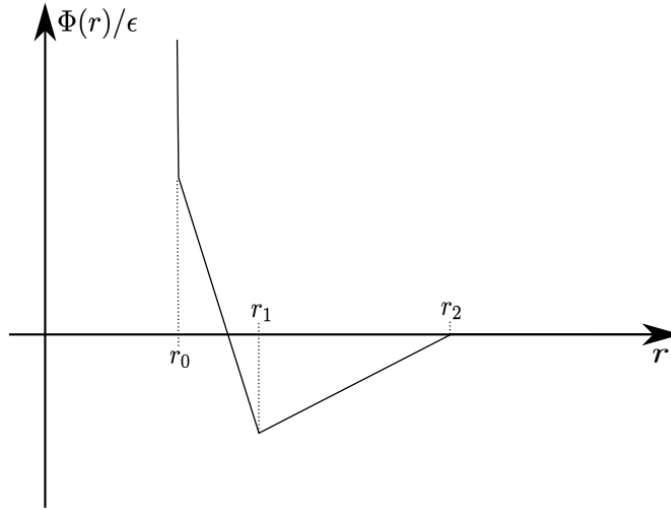
Figure 1.15: Ramp potential.

The ramp potential has been of special interest as it has a liquid-liquid critical point, like water [46, 47].

The Yukawa potential is an example of a hard core repulsion, but with a long range, smooth attraction. It has been shown to be effective for simulating colloids and plasmas [48]. The attractive Yukawa potential with a hard core is described by

$$\phi_{HS-Yukawa}/\epsilon = \begin{cases} \infty & r < \sigma \\ -\frac{e^{-kr}}{r/\sigma} & r \geq \sigma \end{cases} \tag{1.21}$$

for $r \geq \sigma$, where k is a parameter that controls the range of the attraction and ϵ is the attractive well depth. The HS-Yukawa potential is depicted in figure 1.16.

A potential which has been softened in the repulsive and attractive region can be constructed using quantum-mechanical calculations [32]. For particles at large separations, the contribution to the potential is largely dominated by multipole

16
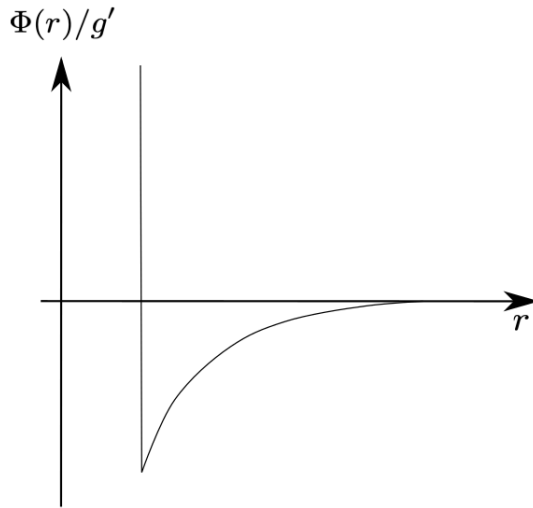
Figure 1.16: HS plus Yukawa potential.

dispersion interactions between the instantaneous electric moments of interacting atoms. All multipole interactions contribute, however the energy is dominated by the dipole-dipole interaction, which varies as r^{-6} [49]. Over short ranges the repulsive interaction can be represented in exponential form $\exp(-r/r_0)$, where r_0 is the range of the repulsion. Due to mathematical convenience, the convention has been to represent the repulsive contribution as an inverse power of r. The power can be chosen arbitrarily, as long as it is larger than the attractive contribution r^{-6}. Usually a value between 9 and 15 is chosen, but 12 has by far been the most used and well studied. This is the 12-6 Lennard-Jones (LJ) potential [50], which is given by

$$\phi_{LJ} = 4\epsilon \left[\left(\frac{\sigma}{r} \right)^{12} - \left(\frac{\sigma}{r} \right)^{6} \right] \tag{1.22}$$

and depicted in figure 1.17.

The LJ potential vanishes at infinite separation distances but becomes very large, rising to positive infinity, at the origin. For the purpose of simulations, potentials have to be capped at a certain distance, as calculating all interactions at very long range is computationally expensive. The LJ potential is sometimes shifted so it becomes zero at the cut off distance. However, only modifying the potential energy does not ensure that forces are continuous too [51].

A useful variant of the LJ potential is the Weeks-Chandler-Andersen (WCA). It

17
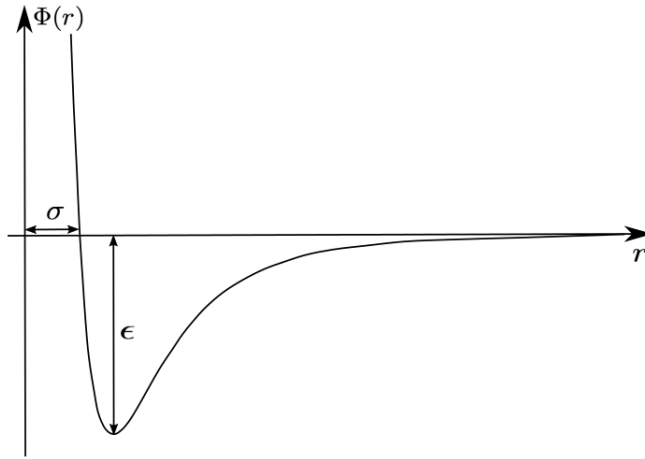
Figure 1.17: The Lennard-Jones potential.

is the LJ potential truncated at the LJ minimum at $2^{1/6}\sigma$ and shifted by the energy at the minimum, as given by

$$\phi_{WCA}(r) = \begin{cases} 4\epsilon\left[\left(\frac{\sigma}{r}\right)^{12} - \left(\frac{\sigma}{r}\right)^{6}\right] + \epsilon & r \leq 2^{1/6}\sigma \\ 0 & r > 2^{1/6}\sigma \end{cases} \qquad (1.23)$$

and displayed in figure 1.18. It still consists of the attractive and repulsive components, but, due to being shifted upwards and truncated, it is purely repulsive [52]. It's original purpose was to act as a reference system to the LJ system in perturbation theory [53].
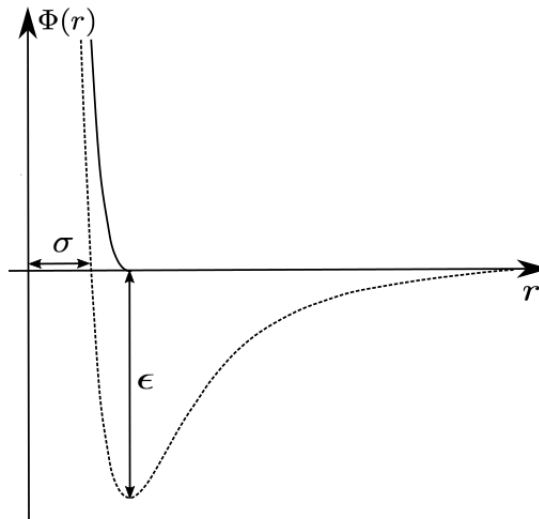
Figure 1.18: WCA potential (solid line) in comparison with the unshifted LJ (broken line).

Holian and Evans [54] introduced a variant of the LJ potential, the LJ spline

18

(LJ/s), in which the LJ potential is truncated at the point of maximum attractive force and then smoothly interpolated to zero via a cubic spline. This ensures the force and its derivatives are continuous at the cut off. The phase diagram for this system is currently unknown.

Hoover, in his textbook *Smooth Particle Applied Mechanics* [55], introduces another family of pair potentials which in their design are short ranged, vanish at a finite separation distance and are continuous in their derivatives. The phase diagrams for the members of this family are unknown known. Further details on this family of potentials, along with the LJ/s are given in Section 2.

1.2.2 Phase diagrams

A phase diagram shows the different phases that a substance can exist in under certain thermodynamic conditions such as temperature, pressure and density. An example of a phase diagram is shown in figure 1.19. It displays the following key features: (1) The liquid-vapour coexistence, the dome under which a gas and liquid coexist and are distinguishable. (2) The critical temperature, the maximum of the liquid-vapour coexistence dome. Above the critical temperature, a gas cannot be liquified by applying pressure as the kinetic energy of the particles is too high. (3) The triple point line, which appears as a horizontal line in the temperature-density plane. It defines the single state where solid, liquid and vapour all coexist. (4) The freezing line, where the liquid freezes. (5) The melting line where solids melt.

Along a phase boundary, two or more phases are able to co-exist. For two phases to be able to coexist they must be in thermal, mechanical and chemical equilibrium [56].

$$T_\alpha = T_\beta \quad ; \quad p_\alpha = p_\beta \quad ; \quad \mu_\alpha = \mu_\beta \tag{1.24}$$

Under the dome, liquid and vapour coexist, the borders making up the dome are referred to as saturation lines. This is where a phase transition happens, either from a homogeneous gas to liquid-vapour, or from the liquid-vapour to a homogeneous
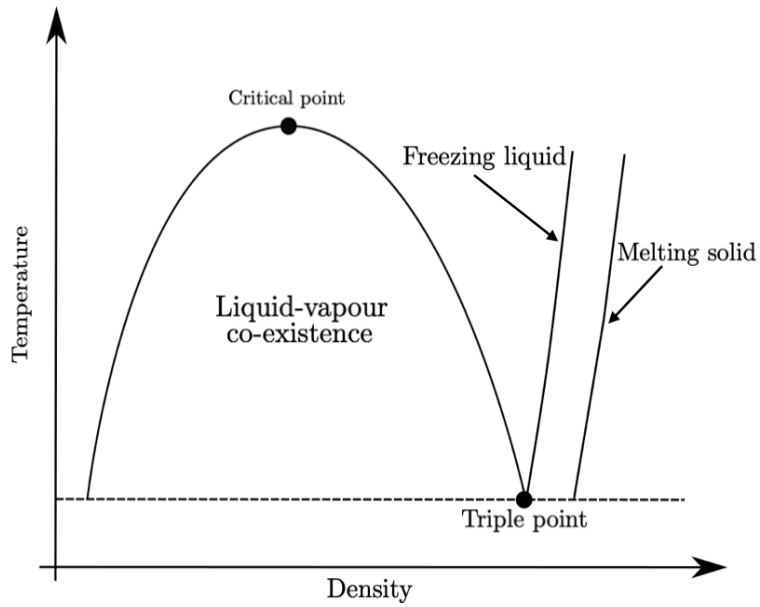
Figure 1.19: Illustration of a typical single component substance temperature-density phase diagram. Showing the liquid-vapour coexistence dome and the freezing-melting line.

liquid. Homogeneous refers to a phase in which the substance has the same chemical and physical constitution throughout.

Consider the two phase change process illustrated on the temperature vs. specific volume plot in figure 1.20. State (1) is the state of a homogenous liquid. Heating
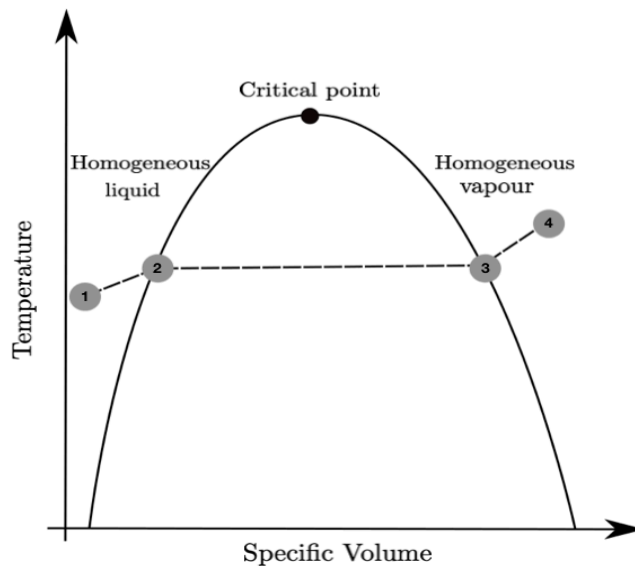
Figure 1.20: Two phase changes in the liquid vapour phase (1) Homogeneous liquid. (2) Saturated vapour (3) Saturated liquid (4) Homogeneous vapour.

the system at constant pressure raises the temperature, and the specific volume. Eventually it reaches the saturated liquid line, at state (2). The substance continues

to be heated, but within the liquid-vapour dome, heating results in no change in temperature, but increases the specific volume. Between state (2) and (3) the system exists as two phases. Continued heating will lead to vaporisation of all liquid in the mixed state, arriving at state (3), the saturated vapour line. At state (3) further heating will result in a change in temperature as well as specific volume.

There are well established simulation methods for obtaining phase diagrams, but they each have limitations and can therefore not necessarily provide a full calculation of a systems' phase diagram on their own. The most theoretically simple method is that of simulating explicit interfaces [57,58], but several simulations are required to obtain a single coexistence point, it is therefore very computationally expensive. A popular method is the Gibbs ensemble [59,60], which requires only one simulation for each pair of coexistence points. Since it simulates two homogenous phases, it performs badly near the critical point when the two phases becomes less distinguishable. As it relies on particle insertions as well, it requires modifications to work in the solid region where such events are rare [61,62]. Kofke integration is based on integrating the Clausius-Clapeyron equation along a saturation line [63], which in a single simulation calculates the coexistence line. However, it is very dependent on a well defined initial point on the saturation line, to start the calculations [64]. Histogram reweighting is a way of extracting more information from a single simulation, about a state very close to the one simulated [65–67]. This method still requires a significant number of simulations, to yield a whole phase diagram.

Having discussed the homogeneous liquid's place on the phase diagram, it is worth mentioning that the conditions which make and define a liquid, are not fully understood. While there is a qualitative distinction between a solid and a fluid phase, the same is not true for a gas and liquid phase. Indeed, Van der Waals pointed out the continuity between the liquid and the gas phase [68]. Whether a system allows a stable liquid phase to be formed depends on the intermolecular potential, as was briefly mentioned in section 2, when reviewing the need to introduce an attraction.

In a letter to Nature in 1993 [69], Hage et al. considered the system of C_{60}. As its relatively short ranged potential greatly differs from that of noble gases. The LJ

potential has with success been used to model noble gases, but the potential for C_{60} differs greatly, the most significant difference being the width of the attractive well. They questioned the effect a short ranged potential might have on the predicted phase diagram and concluded that the shorter ranged potential results in a triple point lying above the critical temperature, indicating that C_{60} cannot exist in a homogenous liquid state.

At the same time, Cheng *et. al.* [70] obtained a contradictory result when studying the phase diagram of C_{60}. They concluded that a homogenous liquid region does exist, but only in a very narrow temperature range compared to the LJ system.

In 2003 *Chen et. al.* confirmed the existence of the narrow liquid phase in C_{60}, by Gibbs ensemble Monte Carlo simulations. They extended their studies into investigating two other types of carbon, C_{70} and C_{96}, as the molecular weight of the carbon molecules becomes larger, the width of the potential wells becomes narrower.

They found that C_{60} has a narrow liquid phase, as does C_{70}, but the "triple line" has disappeared for C_{96}, indicating that this system will not have a homogenous liquid phase. These studies show that solely introducing an attraction to a potential is not sufficient for that system to show a detectable homogenous liquid phase. The existence of such a phase is highly dependent on the location of the triple point in relation to the critical point on the phase diagram. The location of the triple point and critical point have a strong dependence on the width of the attractive well of the potentials.

1.2.3 Analytical equations of state.

In the construction of phase diagrams it is desirable to have a simple, general and accurate relationship between the thermodynamical properties of a given substance. Any such equation is referred to as an *equation of state* (EoS) [71]. For a one-component system a general EoS takes the form [72]

$$f(p, V, T) = 0 \tag{1.25}$$

Equations of state have existed for centuries, starting from the very simple EoS, like the the ideal gas law, stated by Clapeyron in 1834 [73]

$$PV = nRT \tag{1.26}$$

where P is the pressure, V is the volume, T is the temperature, n the number of moles of gas and R the universal gas constant. Although the ideal gas law describes a hypothetical gas, it provides a good approximation to real gases at low pressures and moderate temperatures. Importantly the ideal gas EoS fails at higher pressures and lower temperatures and cannot predict a gas-liquid phase transition.

Later, in 1873 Van der Waals proposed a new equation of state (VdW EoS) in his thesis. It was more accurate than the ideal gas EoS [74], because it accounted for particle size and particle interactions

$$\left(P + \frac{a}{V^2}\right)(V - b) = RT \tag{1.27}$$

where a and b are constants which depend on the nature of the gas. The term a/V^2 is known as the internal pressure and originates from the attractive forces between gas molecules, whilst b is the VdW co-volume and accounts for the finite size of molecules. The VdW equation may be written explicitly in terms of volume

$$V^3 - V^2 \left[\frac{RT}{p} + b\right] + aV - \frac{ab}{p} = 0 \tag{1.28}$$

which is a cubic polynomial equation. This equation has three solutions, all of which can be real or one is real and two are complex. The case of three real solutions to a VdW isotherm is displayed in figure 1.21. Above the critical temperature, the VdW isotherms behaves like an ideal gas. When applying the VdW equation of state to temperatures below the critical temperature, the isotherm displays unphysical behaviour. Recalling the liquid-vapour dome in figure 1.20, in the liquid-vapour coexistence region, during heating, there is no change to the pressure or volume. Experimentally obtained isotherms are displayed in figure 1.22, taken from [75].

Clearly the VdW model fails to predict the observed isotherms. The cubic nature of the VdW EoS displays a loop, as it must have three solutions, indicating pressure would change with volume.
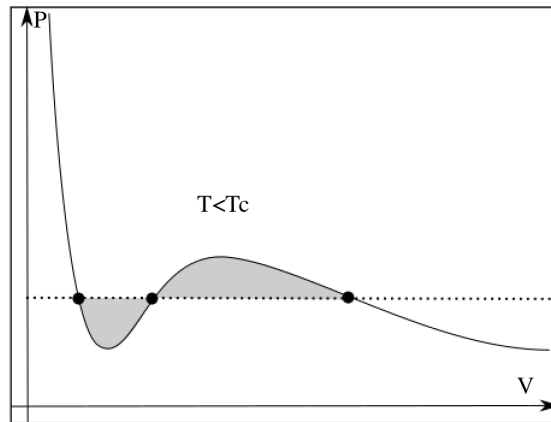
Figure 1.21: VDW isotherm at a temperature above the critical point. Displaying the three solutions to the cubic equation of state, and the shaded area for the Maxwell construction.
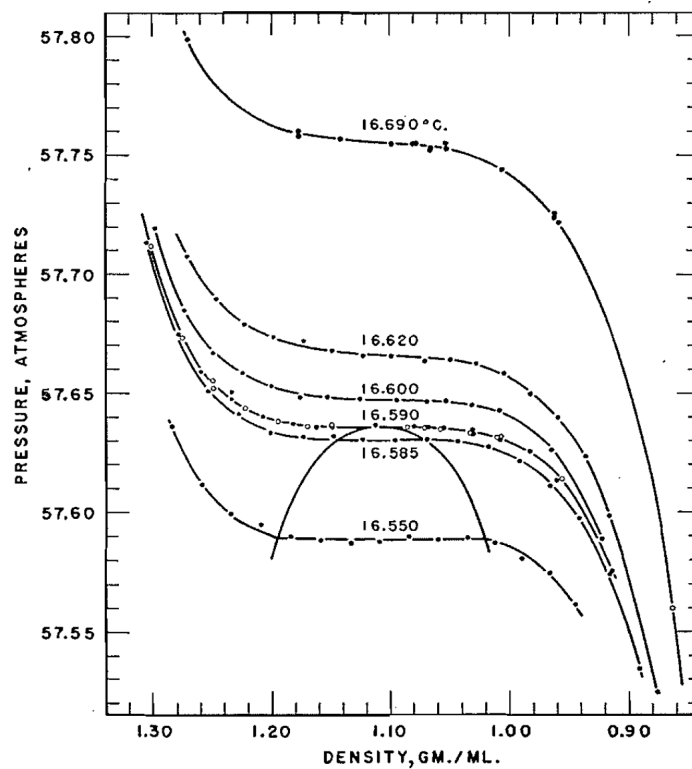
Figure 1.22: Pressure-density isotherms of xenon, displaying the binodal (gas-liquid coexistence) and the experimentally measured isotherms above, at and below the critical temperature [75].

The unphysical feature of the VdW loop can be corrected by performing a *Maxwell Construction*. As it is an isothermal process, the two phases have already

24

satisfied the equal temperature condition for equilibrium and they exist at equal pressure. The remaining condition to be satisfied is equal chemical potential. Using the conditions of coexistence: equal temperature, equal pressure and equal chemical potential, it is found that changes in pressure while keeping temperature constant gives the following expression for the change in chemical potential

$$d\mu = \left(\frac{\partial \mu}{\partial P}\right)_T dp \tag{1.29}$$

The chemical potential is simply the Gibbs free energy per particle, $\mu_i = (\partial G/\partial N_i)_{j,k...}$ which for a one-component system becomes $\mu = G/N$ and, from thermodynamics,

$$\left(\frac{\partial G}{\partial p}\right)_T = V \tag{1.30}$$

Integrating along the path of the isotherm, the chemical potential is given by the integral

$$\mu(p, T) = \mu_{liquid} + \int_{p_{liquid}}^{p} \frac{V(p', T)}{N} dp' \tag{1.31}$$

Graphically, the Maxwell construction corresponds to constructing equal areas, which are the shaded regions displayed in figure 1.21.
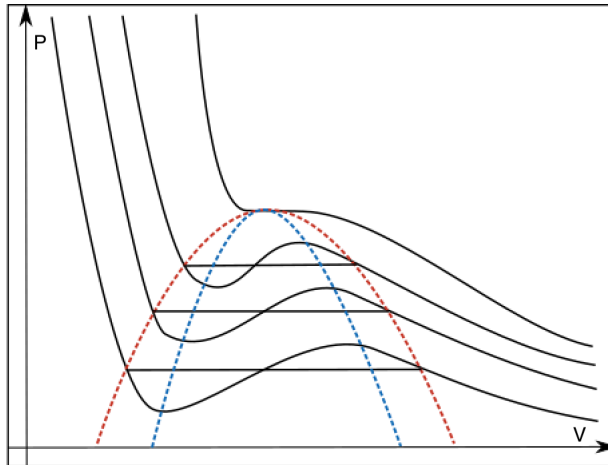
Figure 1.23: Van der Walls isotherms with Maxwell construction (black lines), showing the binodal, coexistence points of gas and liquid (red broken lines) and within the coexistence region, the spinodal (blue broken lines).

Producing multiple isotherms and performing the Maxwell construction to obtain

the coexistence densities will result in a curve which defines the coexistence states known as the *binodal*, this is the red broken line shown in figure 1.23. From the Van der Waals loops we also observe that there are a set of stationary states within the coexistence region $dP/dV = 0$. These points construct a curve, the *spinodal*, shown in figure 1.23 (blue broken line). The states contained between the binodal and spinodal curves are metastable. These states are very sensitive to changes, but if a gas is slowly compressed, or a liquid slowly expanded, the substance can exist in this metastable state as supercooled vapour or superheated liquid.

The conditions for the critical temperature are

$$\left(\frac{\partial P}{\partial V}\right)_T = 0 \quad ; \quad \left(\frac{\partial^2 P}{\partial V^2}\right)_T = 0 \tag{1.32}$$

Using the Van der Waals equation we can derive the critical volume, critical pressure and critical temperature.

$$V_c = 3b \quad ; \quad P_c = \frac{1}{27}\frac{a}{b^2} \quad ; \quad T_c = \frac{8}{27}\frac{a}{bR} \tag{1.33}$$

There is no denying the usefulness of the VDW EoS, which is satisfying given its simplicity. However, it is limited to the lower density region. It is therefore not a surprise that modifications and expansions to the VDW EoS have been made to increase the region of applicability. In 1928 the Beattie-Bridgeman EoS was proposed, it expresses the VdW EoS on a unit-mole basis by replacing the molar volume V with $\bar{\nu}$ (specific volume $= 1/\rho$) and the ideal gas constant R with the universal gas constant R_u, where the universal gas constant is $R = R_u/M_{gas}$, M_{gas} being the mass of the gas. It is based on five experimentally determined constants [71]

$$P = \frac{R_u T}{\bar{\nu}^2}\left(1 - \frac{c}{\bar{\nu}T^3}\right)(\bar{\nu} + B) - \frac{A}{\bar{\nu}^2} \tag{1.34}$$

where $A = A_0\left(1 - \frac{a}{\nu}\right)$ and $B = B_0\left(1 - \frac{b}{\nu}\right)$. The Beattie-Bridgeman EoS is accurate up to densities around $0.8\rho_c$, where ρ_c is the critical density. In 1940 Benedict, Webb and Rubin [71] increased the number of constants to eight and thereby raised the

26

accuracy of the equation to around $2.5\rho_{cr}$. Other cubic equations of states are the Redlich-Kwong EoS formulated in 1949 [76], which because of its relatively simple form is still used today, but it does not perform well in predicting the liquid phase. It does well in the gas phase, and is superior to the VdW EoS in this region. The disadvantage of the cubic EoS is that the predicted molar volume V of the liquid phase is significantly less accurate than the molar volume predicted for the gas phase. In 1976 Peng and Robinson [77] set out to develop an EoS to satisfy four criteria. 1) Parameters should be expressed in terms of the critical property's acentric factor (measure of the non-sphericity of molecules). 2) It should provide good accuracy at the critical point. 3) The mixing parameter should not be using more than a single binary interaction parameter. 4) The EoS should work in the fluid and gas region. The Peng-Robinson EoS provides a good description of the liquid phase, but has an inaccuracy in the VdW repulsive term. In 1982 Peneloux *et al.* [78] made a correction to V to address that problem. They introduced an additional fluid component parameter that changes the molar volume. Statistical associating fluid theory (SAFT) equations of state use statistical mechanics methods like perturbation theory, to describe intermolecular interactions [79–81]. The SAFT equations of state are found to be more accurate than cubic EoS in the liquid and solid region [82, 83].

H. Kamerlingh Onnes had, in the early 1900s, attempted to construct EoS, but found that every one of them failed to have good agreement with experimental data, and when there was a good agreement, the same knowledge could be obtained theoretically by the VdW EoS. He therefore changed strategy and sought to construct an EoS that would be completely independent of theory, only taking experimental values into account. This materialised into an equation of state expressed as a power series in inverse volume: the virial EoS [84]

$$Z = pV/RT = A + B(T)/V + C(T)/V^2 + D(T)/V^3 + \cdots \qquad (1.35)$$

where Z is a dimensionless compressibility factor, which denotes the deviation of

a real fluid from the ideal gas. The coefficients, A, B, C and D, are the virial coefficients. A is always 1, because any fluid at low densities behaves like an ideal gas. The rest of the coefficients are dependent on temperature. A more detailed discussion of Onnes initial work on the virial EoS is provided in section 3. The result was an equation of state that included over twenty terms, so not as simple as could be hoped for. However, it was an EoS successfully describing a theoretical substance.

Onnes calculated virial coefficients by fitting the EoS to empirical isotherms. Ursell introduced a more mathematical approach to determine virial coefficients. From statistical mechanics it is known that the pressure is related to the partition function Z_N by [39]

$$P = k_B T \left(\frac{\partial \ln Z_N}{\partial V} \right) \tag{1.36}$$

for a non ideal gas, the partition function Z_N can be written as

$$Z_N = \frac{1}{N! \lambda^{3N}} \int W_N(\mathbf{r}^N) d\mathbf{r}^N. \tag{1.37}$$

where λ is the thermal wavelength. Ursell showed that the Boltzmann factor $W_N(\mathbf{r}^N)$, could be expressed as a sum of what he termed U-functions. A few examples of U-functions written in terms of W_N [85] are

$$U_1(\mathbf{r}_i) = W_1(\mathbf{r}_i) \tag{1.38a}$$

$$U_2(\mathbf{r_i}, \mathbf{r}_j) = W_2(\mathbf{r}_i, \mathbf{r}_j) - W_1(\mathbf{r}_i) W_1(\mathbf{r}_j) \tag{1.38b}$$

then W_N can be expressed as a sum

$$W_N(\mathbf{r}^N) = \sum_{(\sum l m_l = N)} \prod U_l(\mathbf{r}^\lambda) \tag{1.39}$$

where m_l denotes a group with l number of particles. The configurational integral written in terms of W_N (mathematical details of the following results can be found

in appendix A) can then be solved

$$Q_N = \frac{1}{N!} \int W_N(\mathbf{r}^N) d\mathbf{r}^N = \sum \prod_{l=1}^{N} (Vb_l)^{m_l} / m_l! \tag{1.40}$$

where b_l is the cluster integral

$$b_l = (Vl!)^{-1} \int U_l(\mathbf{r}_1, \mathbf{r}_2, \ldots, \mathbf{r}_l) d\mathbf{r}_1 d\mathbf{r}_2 \ldots d\mathbf{r}_l \tag{1.41}$$

which considers the connections between the particles in a m_l group.

Mayer contributed with a further improvement to the mathematical approach of determining virial coefficients, by introducing the *f-function*, which is the U-function shifted by -1.

$$f_{ij}(\mathbf{r}_{ij}) = [e^{-\phi_{ij}/k_B T} - 1] \tag{1.42}$$

This has the advantage that the f-function is non zero only if the two molecules under consideration are within the cut off distance of the potential.

The f-function are related to the U-functions by

$$U_1(\mathbf{r}_1) = 1 \tag{1.43a}$$

$$U_2(\mathbf{r}_1, \mathbf{r}_2) = f_{12} \tag{1.43b}$$

$$U_3(\mathbf{r}_1, \mathbf{r}_2, \mathbf{r}_3) = f_{12} f_{23} f_{13} + f_{12} f_{23} + f_{23} f_{13} + f_{12} f_{13} \tag{1.43c}$$

The f-bonds configuration for the m_3 group is given as an example of the graphical representation of the terms relevant for the cluster integral relating to the third virial coefficient, in figure 1.24.
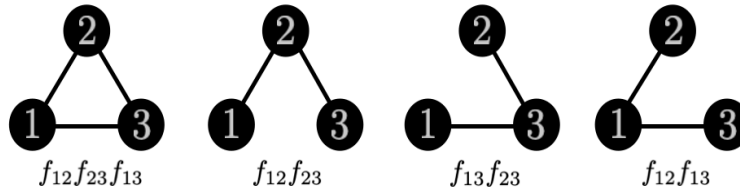
Figure 1.24: Diagrams showing the Mayer f-bonds for clusters relating to the U-bond $U_3((\mathbf{r}_1, \mathbf{r}_2, \mathbf{r}_3))$.

The Mayer cluster integral then becomes

$$b_l = (Vl!)^{-1} \int \sum f_{1,2,...} f_{l+1} d\mathbf{r}_1 \mathbf{r}_2 \ldots d\mathbf{r}_{l+1} \tag{1.44}$$

A more detailed derivation of Mayer-diagrams and cluster integrals, can be found in section 3.

For the LJ potential, the highest order virial coefficients that have been calculated is the sixteenth, B_{16} [86]. For the parallel hard-cube potential the sixth virial coefficient B_6 has been calculated [87]. For the HD/HS system, the highest order virial calculated is the twelfth B_{12} [88].

EoS are theoretically a powerful tool to gain knowledge about any substance's phase diagram, but in the pursuit of accuracy, especially cubic and SAFT EoS's become impractical to implement, because they require experimentally determined data of the chosen substance, prior to using it. Therefore the virial EoS has its obvious appeal, as the virial coefficients can be determined numerically.

A weakness of the virial equation of state, is the fact that knowledge of the virial coefficients is required and they differ for each system. Its accuracy also depends on the number of terms calculated, which become increasingly difficult to determine. Perturbation theory of the free energy is a way to avoid rigorous calculations of virial coefficients. From an expression of free energy, the pressure and chemical potential can be found from

$$P = -\left(\frac{\partial F}{\partial V}\right)\bigg|_{T,N} \qquad \mu = \left(\frac{\partial F}{\partial N}\right)\bigg|_{T,V}. \tag{1.45}$$

The basic premise of all perturbation theories is the separation of the pair potential into two terms

$$u(r) = u_0(r) + u_1(r) \tag{1.46}$$

where u_0 is the pair potential of a reference system and $u_1(r)$ is the perturbation. The effect of the perturbation on the thermodynamic properties of the reference system is calculated in either of two ways. The first involves an expansion of the

free energy in powers of inverse temperature (the 'λ' expansion), or a parameter which measures the range of the perturbation (the 'γ' expansion). In the former case, a coupling parameter, λ, is introduced:

$$u(r) = u_0(r) + u_1(r; \lambda) \tag{1.47}$$

λ connects the reference potential to the perturbation potential and can take a value between 0 and 1. When $\lambda = 0$ the perturbation potential becomes equal to that of the reference system. When $\lambda = 1$ it becomes equal to that of the system being studied. Using the coupling constant, the Helmholtz free energy can be expressed as a power series.

$$F(\lambda) = F_0 + \left.\frac{\partial F}{\partial \lambda}\right|_{\lambda=0} \lambda + \frac{1}{2}\left.\frac{\partial^2 F}{\partial \lambda^2}\right|_{\lambda=0} \lambda^2 + ..., \tag{1.48}$$

The first order perturbation when $\lambda = 0$, is given by

$$\frac{F}{Nk_BT} = \frac{F_0}{Nk_BT} + \frac{2\pi}{k_BT}\rho \int_0^\infty u_1(r)g_0(r)r^2 dr \tag{1.49}$$

$g_0(r)$ being the radial distribution function for hard spheres.

There are different ways of splitting the potential into the reference potential u_0 and the perturbed potential u_1. Two ways of doing it, by Barker-Henderson and WCA, are illustrated in figure 1.25.
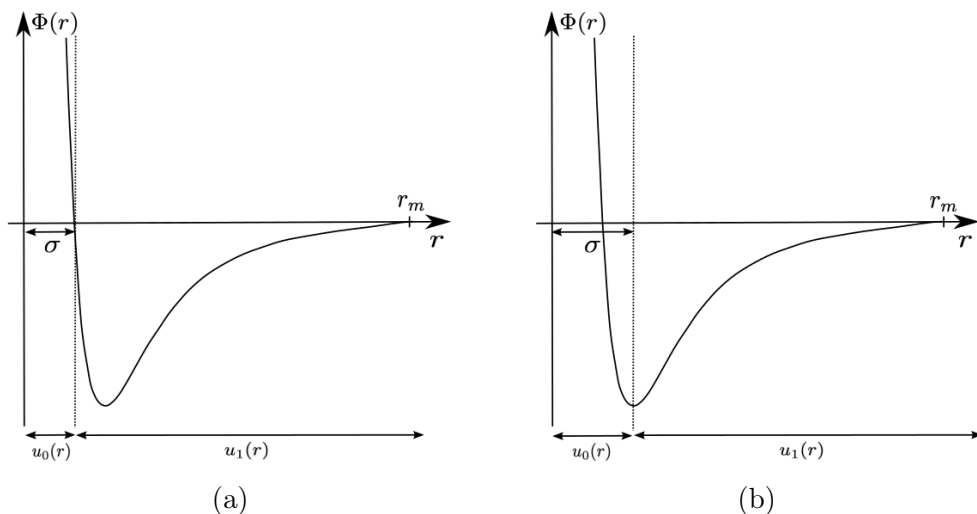
Figure 1.25: (a) Barker-Henderson split. (b) Weeks-Chandler-Andersen split.

Barker and Henderson split it in the following way

$$u_0(r) = \begin{cases} u(r) & r \leq \sigma \\ 0 & r > \sigma \end{cases} \tag{1.50}$$

$$u_1(r) = \begin{cases} 0 & r < \sigma \\ u(r) & r > \sigma \end{cases} \tag{1.51}$$

where σ is the first point at which $u(\sigma) = 0$ and r_m the cut-off distance. The problem is that the radial distribution function and equation of state, is not known for the reference system. This was accommodated by approximating the reference state by that of the HS system, using a temperature dependent hard sphere diameter

$$d = \int_0^\sigma [1 - e^{-\beta u(r)}] dr \tag{1.52}$$

The WCA potential split is given in the following way [89, 90]

$$u_0(r) = \begin{cases} u(r) - u(r_m) & r \leq \sigma \\ 0 & r > \sigma \end{cases} \tag{1.53}$$

$$u_1(r) = \begin{cases} u(r_m) & r \leq r_m \\ u(r) & r > \sigma \end{cases} \tag{1.54}$$

Choosing to split at the minima, rather than when $u_0(r) = 0$, has the advantage that the reference state includes all of the repulsive forces. The Song-Mason approximation uses the same split as WCA, but expands from the truncated, $N = 2$, virial EoS [91]. This is advantageous as it only requires knowledge of the potential and the virial EoS truncated at B_2.

Finally, it is worth noting that a popular and very practical method of obtaining the relation between thermodynamic properties of a substance are property tables [71]. They are empirically obtained values and are therefore very accurate. However, each point on the phase diagram requires a separate measurement. Constructing

property tables for infinitely many points to obtain absolute accuracy is highly impractical, making property tables limited to the range of values in which it was obtained. Despite its practicality of use, constructing an equation of state would be preferable.

1.2.4 Conclusion

Developing a MD Joule-Thomson throttling algorithm would provide a useful tool to further investigate non-equilibrium steady states. For the simulation to be successful, it needs to display constant enthalpy. This could most certainly be achieved using a well known potential such as the LJ, but potentials such as the LJ/s and mn-family may prove themselves much better suited for MD simulations, as they have been designed to have a finite cut off and maintain continuity in their forces, without requiring further modifications. Unfortunately the phase diagrams for these potentials are unknown, therefore it is necessary to investigate methods for obtaining an equation of state.

This work aims to produce a working Joule-Thomson MD algorithm, by employing one of the potentials from the mn-family, after having first obtained theoretical estimates of the phase diagram and Joule-Thomson inversion curves.

2 Mathematical properties of the mn and LJ/s potentials

This chapter reviews two families of pair potentials which have useful mathematical properties (short ranged and smoothness) for use in MD simulations of Joule Thomson throttling.

2.1 mn-pair potentials

The mn-family of potentials was first introduced in 2006 by Hoover and Hoover [55]. It was chosen for the purpose of simulating a ball plate penetration problem using MD. A generalised version of this family is defined by

$$\phi_{m-n}(r) = \begin{cases} \frac{m}{n-m}(r_c^2 - r^2)^n - \frac{n}{n-m}(r_c^2 - r^2)^m & 0 < r < r_c \\ 0 & r \geq r_c \end{cases} \tag{2.1}$$

The potential is in a dimensionless form, meaning ϕ is actually ϕ/ϵ and r is really r/σ, where ϵ and σ are suitable energy and length scales. m and n are positive integers and $n > m$. It is also clear that when the separation distance becomes equal to the cut-off distance the potential vanishes.

Hoover used a cut-off distance of $r_c = \sqrt{2}$, giving the expression for a family of potentials with a specific cut-off

$$\phi_{m-n}(r) = \begin{cases} \frac{m}{n-m}(2 - r^2)^n - \frac{n}{n-m}(2 - r^2)^m & 0 < r < \sqrt{2} \\ 0 & r \geq \sqrt{2} \end{cases} \tag{2.2}$$

The minimum occurs at $\phi(r = 1) = -1$ for all values of m and n.

In order to maintain accuracy of energy calculations in MD, the derivatives of the potential must also be continuous [30]. Considering the first derivatives of the potential

$$\phi_{m-n}^{(1)}(r < \sqrt{2}) = \frac{2mnr}{m-n}(2 - r^2)^{(n-1)} - \frac{2mnr}{m-n}(2 - r^2)^{(m-1)} \tag{2.3}$$

it can be seen that the force,

$$\mathbf{F}(r) = -\frac{\partial\phi(r)}{\partial\mathbf{r}} \tag{2.4}$$

is continuous, as desired. Similarly, we can see that the second derivative

$$\phi_{m-n}^{(2)}(r < \sqrt{2}) = \frac{2mn}{m-n}(2-r^2)^{(n-1)} - \frac{2mn}{m-n}(2-r^2)^{(m-1)}$$
$$+\frac{4mnr^2}{m-n}(2-r^2)^{(m-2)}(m-1) \tag{2.5}$$
$$-\frac{4mnr^2}{m-n}(2-r^2)^{(n-2)}(n-1)$$

is also continuous so that the configurational temperature which depends on both the first and second derivative of the potential [92]

$$k_B T_{conf} = \frac{\left\langle \sum_{i=1}^{N}(\partial\phi/\partial\mathbf{r}_i)^2 \right\rangle}{\left\langle \sum_{i=1}^{N}\partial^2\phi/\partial\mathbf{r}_i^2 \right\rangle} \tag{2.6}$$

will also be continuous. The desire to have continuity in the higher order differentials poses another restriction on m and n. The next three differentials of ϕ are given by

$$\phi_{m-n}^{(3)}(r < \sqrt{2}) = \frac{12mnr}{m-n}(2-r^2)^{(m-2)}(m-1)$$
$$-\frac{12mnr}{m-n}(2-r^2)^{(n-2)}(n-1)$$
$$-\frac{8mnr^3}{m-n}(2-r^2)^{(m-3)}(m-1)(m-2) \tag{2.7}$$
$$+\frac{8mnr^3}{m-n}(2-r^2)^{(n-3)}(n-1)(n-2)$$

$$\phi_{m-n}^{(4)}(r < \sqrt{2}) = \frac{12mn}{m-n}(2-r^2)^{(m-2)}(m-1)$$
$$-\frac{12mn}{m-n}(2-r^2)^{(n-2)}(n-1)$$
$$-\frac{48mnr^2}{m-n}(2-r^2)^{(m-3)}(m-1)(m-2)$$
$$+\frac{48mnr^2}{m-n}(2-r^2)^{n-3}(n-2)(n-2) \tag{2.8}$$
$$+\frac{16mnr^4}{m-n}(2-r^2)^{(m-4)}(m-1)(m-2)(m-3)$$
$$-\frac{16mnr^4}{m-n}(2-r^2)^{(n-4)}(n-1)(n-2)(n-3)$$

35

$$\phi^{(5)}_{m-n}(r < \sqrt{2}) = \frac{120mnr}{m-n}(2-r^2)^{(n-3)}(n-1)(n-2)$$
$$-\frac{120mnr}{m-n}(2-r^2)^{(m-3)}(m-1)(m-2)$$
$$+\frac{160mnr^3}{m-n}(2-r^2)^{(m-4)}(m-1)(m-2)(m-3)$$
$$-\frac{160mnr^3}{m-n}(2-r^2)^{(n-4)}(n-1)(n-2)(n-3)$$
$$+\frac{32mnr^5}{m-n}(2-r^2)^{(n-5)}(n-1)(n-2)(n-3)(n-4)$$
$$-\frac{32mnr^5}{m-n}(2-r^2)(m-5)(m-1)(m-2)(m-3)(m-4)$$

(2.9)

The pattern in the differentials shows that each member of the family is continuous up to the $(m-1)^{th}$ derivative. Therefore the higher the value of m, the higher the order of derivatives that are continuous at the cut off. Although most current calculations will not require more than three continuous derivatives, it is worth noting that if the value of n is not too large, causing the value at the origin to become too high, a reasonable number of accurate derivatives are available at no extra cost. The potentials are maximal at the origin ($r = 0$), therefore

$$\phi_{max} = \frac{2^m n}{m-n} - \frac{2^n m}{m-n}$$

(2.10)

Due to the condition $n > m$, the magnitude of the potential at the origin is largely dominated by the 2^n term. For the first derivative, the magnitude at $r = 0$ is zero.

Three members of the mn family have been chosen for this study, each with $n = 2m$, and m values: $m = 4$, 5, and 6. The member with $m = 4$ was chosen as it has already been used by Hoover [55]. Mathematically, a much lower value of m will cause lower order derivatives to no longer vanish when reaching the cut off length, therefore, higher values of m were chosen. It was mathematically pleasing to select them in ascending order.

$$\phi_{4-8} = (2-r^2)^8 - 2(2-r^2)^4$$

(2.11)

36

$$\phi_{5-10} = (2 - r^2)^{10} - 2(2 - r^2)^5 \tag{2.12}$$

$$\phi_{6-12} = (2 - r^2)^{12} - 2(2 - r^2)^6 \tag{2.13}$$

These potentials are illustrated in figure 2.1. Their corresponding forces are displayed in figure 2.2.
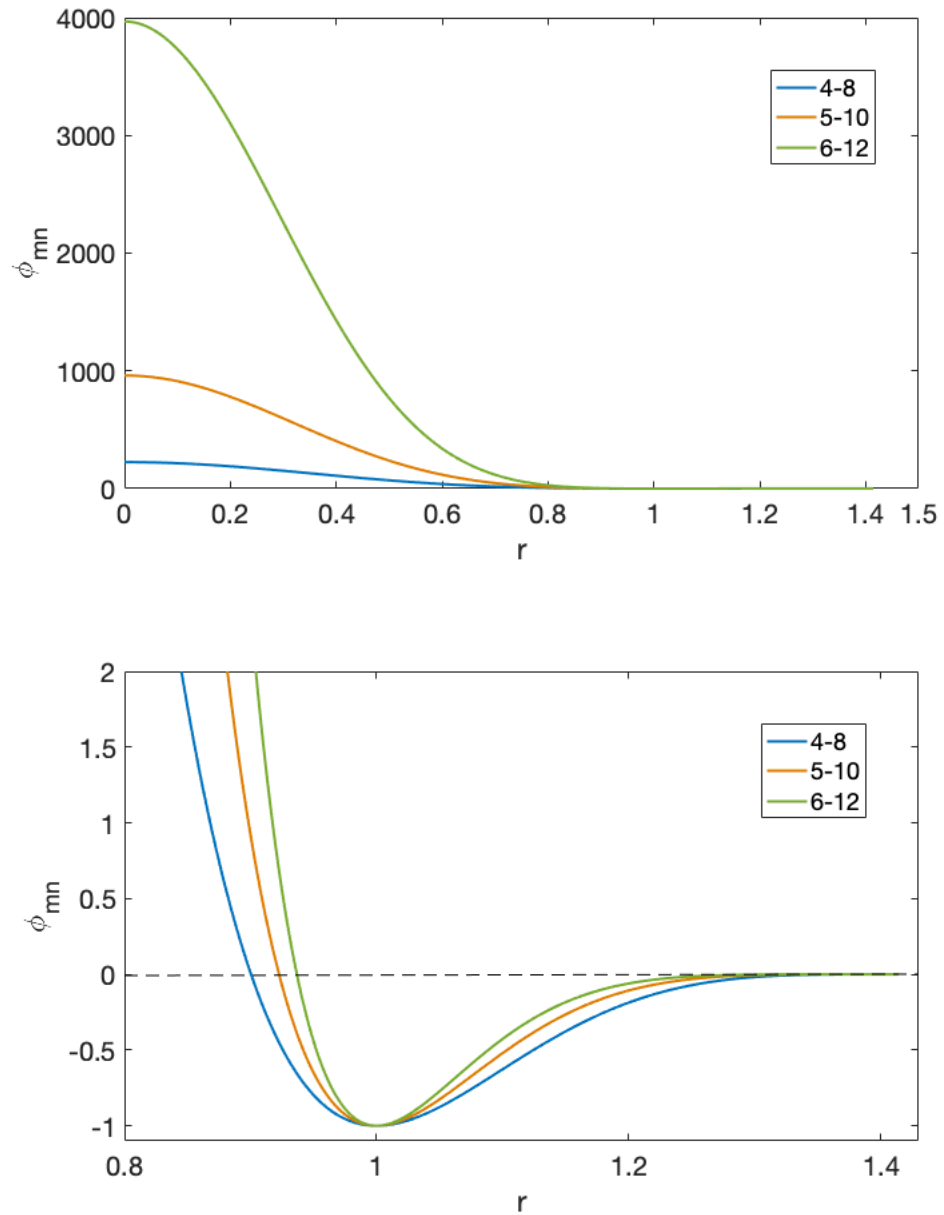
Figure 2.1: Selected members of the mn family of potentials showing the potentials value at the origin (top) and their potential well (bottom)
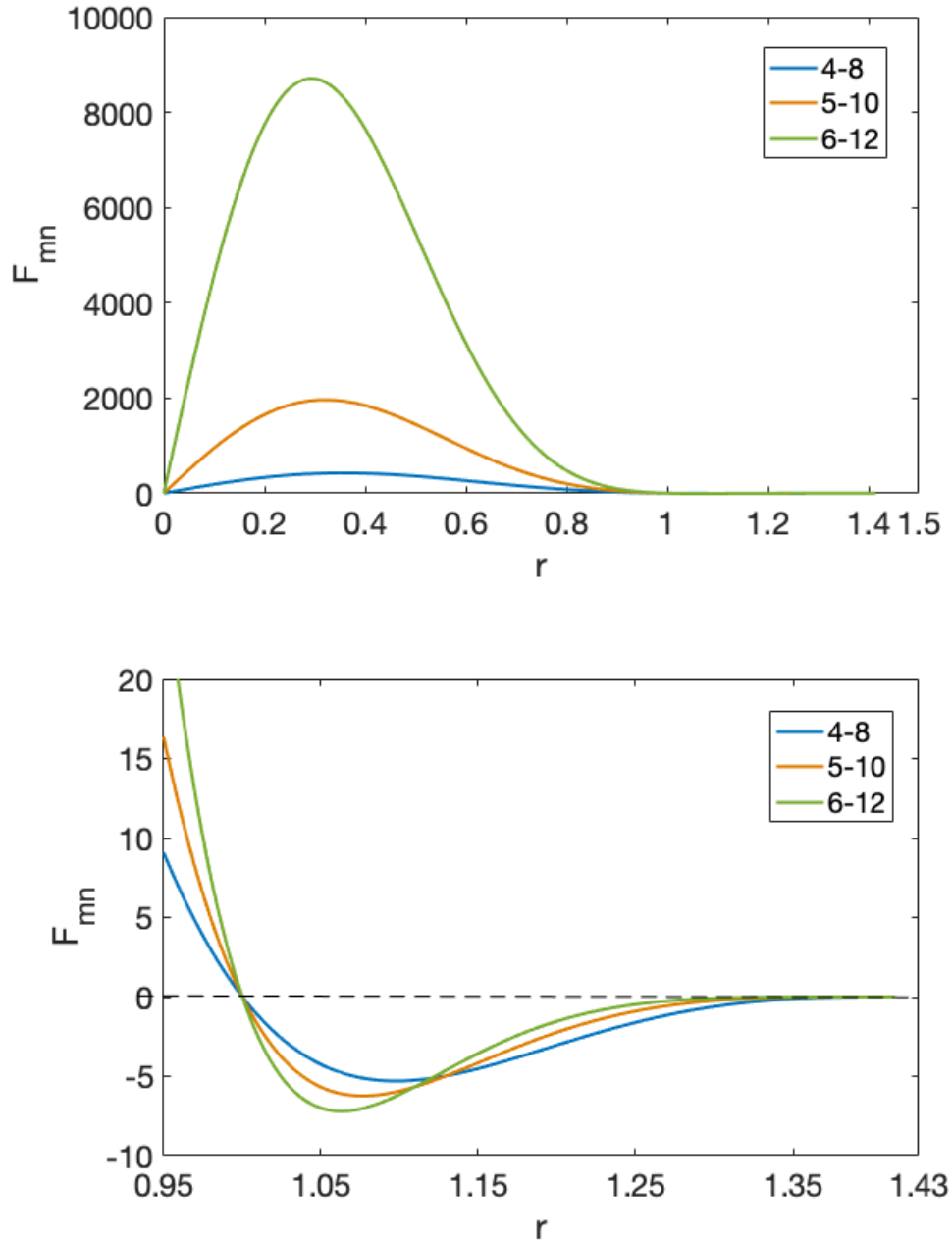
Figure 2.2: Force of the three selected members of the *mn*-family showing their maxima (top) and minima (bottom).

2.2 Lennard Jones spline family

The LJ/s potential as formulated by Holian and Evans is defined piecewise by [93]

$$
\Phi_{LJ/s}(r) = \begin{cases} 4\epsilon[(\sigma/r)^{12} - (\sigma/r)^6] & 0 < r < r_s \\ a(r - r_c)^2 + b(r - r_c)^3 & r_s \leq r \leq r_c \\ 0 & r > r_c \end{cases} \tag{2.14}
$$

The potential is split at the inflexion point r_s and smoothly extrapolated to zero at $r = r_c$ by a cubic spline function. At the point of inflexion the second derivative of the potential is zero, $\phi(r_s)'' = 0$. The first derivative is

$$
\phi' = 4\epsilon\left[-\frac{12}{r}\left(\frac{\sigma}{r}\right)^{12} + \frac{6}{r}\left(\frac{\sigma}{r}\right)^6\right] \tag{2.15}
$$

whilst the second derivative is

$$
\begin{aligned}
\phi'' &= 4\epsilon\left[\frac{12 \times 13}{r^2}\left(\frac{\sigma}{r}\right)^{12} - \frac{6 \times 7}{r^2}\left(\frac{\sigma}{r}\right)^6\right] \\
&= \left[\frac{12 \times 13}{r_s^2}\left(\frac{\sigma}{r_s}\right)^{12} - \frac{6 \times 7}{r_s^2}\left(\frac{\sigma}{r_s}\right)^6\right] \\
&= 0
\end{aligned} \tag{2.16}
$$

Hence

$$
\frac{12 \times 13}{6 \times 7}\left(\frac{\sigma}{r_s}\right)^6 = 1 \tag{2.17}
$$

yielding an expression for the inflexion point r_s

$$
r_s = \sigma \times \left(\frac{26}{7}\right)^{1/6} \tag{2.18}
$$

At the joining point, the cubic spline and its derivative are

$$
S(r_s) = a(r_s - r_c)^2 + b(r_s - r_c)^3 \tag{2.19}
$$

$$
S'(r_s) = 2a(r_s - r_c) + 3b(r_s - r_c)^2. \tag{2.20}
$$

The LJ part at the point of inflexion is given as

$$\phi_{LJ}(r_s) = 4\epsilon\left[\left(\frac{\sigma}{r_s}\right)^{12} - \left(\frac{\sigma}{r_s}\right)^{6}\right] = -\frac{133}{169}\epsilon \tag{2.21}$$

and the first derivative of the LJ at the inflexion point is

$$\phi'_{LJ} = 4\epsilon\left[-\frac{12}{r_s}\left(\frac{7}{26}\right)^2 + \frac{6}{r_s}\left(\frac{7}{26}\right)\right] = \frac{504}{169r_s}\epsilon \tag{2.22}$$

Let the inflexion point r_s be related to the cut off distance r_c by the constant γ, which will be determined later.

$$r_c = \gamma r_s \tag{2.23}$$

Rewriting the cubic spline in terms of r_s and γ

$$S(r_s) = ar_s^2(1-\gamma)^2 + br_s^3(1-\gamma)^3 \tag{2.24}$$

and its first derivative

$$S'(r_s) = 2ar_s(1-\gamma) + 3br_s^2(1-\gamma)^2. \tag{2.25}$$

Equating equations (2.21) with (2.24) and (2.22) with (2.25) yields two equations in two unknowns

$$-\frac{133\epsilon}{169} = ar_s^2(1-\gamma)^2 + br_s^3(1-\gamma)^3 \tag{2.26}$$

$$\frac{504\epsilon}{169r_s} = 2ar_s(1-\gamma) + 3br_s^2(1-\gamma)^2 \tag{2.27}$$

This enables the determination of the cubic spline coefficients a and b by multiplying equation (2.27) by $r_s(1-\gamma)$

$$\frac{504\epsilon}{169}(1-\gamma) = 2ar_s^2(1-\gamma)^2 + 3br_s^3(1-\gamma)^3. \tag{2.28}$$

followed by subtracting $2 \times$ equation (2.26) from equation (2.28)

$$
\begin{aligned}
br_s^3(1-\gamma)^3 &= \frac{504\epsilon(1-\gamma)}{169} + \frac{266\epsilon}{169} \\
&= \frac{\epsilon}{169}\big[504(1-\gamma) + 266\big]
\end{aligned}
\tag{2.29}
$$

yielding an expression for the cubic spline coefficient b

$$
b = \frac{\epsilon}{169r_s^3(1-\gamma)}\bigg[504(1-\gamma) + 266\bigg]
\tag{2.30}
$$

or

$$
\frac{br_s^3}{\epsilon} = \frac{(504(1-\gamma) + 266)}{169(1-\gamma)^3}.
\tag{2.31}
$$

The cubic spline coefficient a, is then found from equation (2.26) - 3 $\times$ equation (2.28)

$$
-ar_s^2(1-\gamma)^2 = \frac{504\epsilon(1-\gamma)}{169} + \frac{399\epsilon}{169}
\tag{2.32}
$$

or

$$
\frac{ar_s^2}{\epsilon} = -\frac{(504(1-\gamma) + 399)}{(1-\gamma)^2 \times 169}
\tag{2.33}
$$

For the spline defined by Hafskjöld and Ikeshoji [94], a cut off $r_c = 67/48 \times r_s = 67/48 \times (26/7)^{1/6} \approx 1.7371$ was chosen, equivalent to $\gamma = 67/48$. With this choice of γ, it is the case that $(1-\gamma)^2 = 19^2/48^2$. This yields a and b cubic spline coefficients relating to the specified cut off

$$
\frac{ar_s^2}{\epsilon} = -\frac{24192}{3211}
\tag{2.34}
$$

$$
\frac{br_s^3}{\epsilon} = -\frac{387072}{61009}
\tag{2.35}
$$

In reduced units ($\epsilon = 1$) the coefficients become

$$
a \approx -4.8649
\tag{2.36a}
$$

$$
b \approx -3.2920
\tag{2.36b}
$$

Using the same method, it is possible to obtain variants of the original LJ/s by using different values for the cut off distance r_c, thereby obtaining different values for the cubic spline coefficients a and b.

By setting the condition that the LJ potential part $\phi_{LJ}(r)$ must equal the spline part $S(r)$ at the inflexion point and the same for their derivatives, it is possible to calculate new values of a and b for different cut offs.

$$
\begin{cases}
\phi_{LJ}(r_s) = S_{LJ/s}(r_s) \\
\phi'_{LJ}(r_s) = S'_{LJ/s}(r_s)
\end{cases}
\tag{2.37}
$$

where $S = a(r - r_c)^2 + b(r - r_c)^3$.

With the use of different cut off distances for the spline, a whole family of spline potentials, with different ranges and well widths can be defined. As was discussed in section 1.2, varying the width of the attractive well has an effect on the observed homogeneous liquid phase. It is therefore of interest to see if by varying the well widths of the LJ/s similar results to those found for fullerenes would be observed for the LJ/s system. This study introduces two further different splines, besides the one defined in [94], with $r_c = 1.4142$ and $r_c = 2.2$. The values for γ and the spline constants a and b are given in table 1. The cut off at $r_c = 1.7371$ was chosen as there already exists an interest in investigating this potential from Hafskjöld. The cut off at $r_c = 1.4142$ was chosen at it is approximately equal to $\sqrt{2}$, the collective cut off chosen for the mn-family members. Since a cut off for the spline at 1.4142 is rather short, the last potential chosen was a longer one with $r_c = 2.2$.

r_c	$r_c/r_s = \gamma$	a	b
1.4142	1.1364	-67.8215	-238.6428
1.7371	1.3958	-4.8649	-3.2920
2.2	1.7678	-0.0780	0.8206

Table 1: Values for three different splines. r_c is the distance at which the potential disappears. r_s is the point at inflexion and a and b are the constants used for the cubic spline.

The three splines are displayed in figure 2.3, compared with the LJ potential, all having the same inflexion point ($r_s = 1.2445$). The minimum, common to all the

members, occurs at $r = 2^{1/6}\sigma \approx 1.12\sigma$.
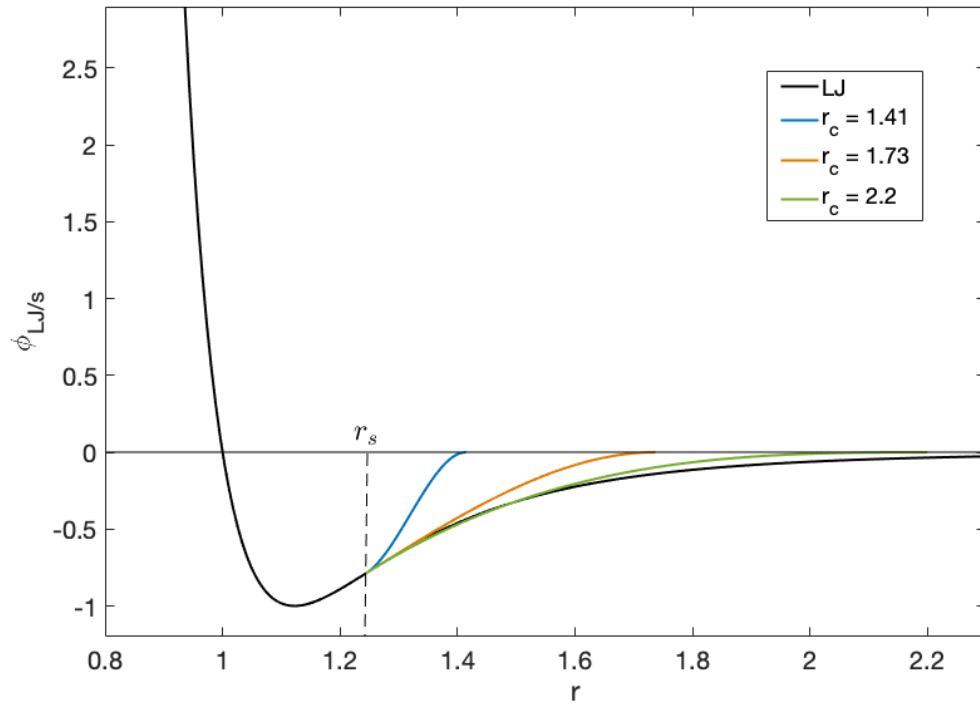
Figure 2.3: Three selected members of the LJ/s family of pair potentials, compared to the LJ potential (black). The three members have different cut off distances at $r_c = 1.41$ (blue) 1.73 (red) and 2.2 (green).

3 Calculation of thermodynamic properties from virial coefficients

The idea of a virial equation of state was formulated by Onnes [95], with the aim of creating a relatively simple equation of state that would be valid in as wide a range of temperatures as possible. Prior to this, equations of state were limited to low temperatures.

Onnes' virial equation of state was based on three existing concepts, the virial theorem, van der Waals equation of state and the law of corresponding states. The virial theorem simply states that for a stable spherical distribution of equal masses, the potential energy must be equal to the kinetic energy within a factor of two [96]. The law of corresponding states refers to the assumption that all gases at the same state should display similar behaviour [97]. Onnes revisited the VdW equation of state to write it as a series expansion [84].

$$P\nu = T\left[1 + \frac{1}{\nu}\left(\frac{1}{8} - \frac{27}{64T}\right) + \frac{1}{64\nu^2} + \frac{1}{512\nu^3} + \dots\right] \tag{3.1}$$

It became clear to him, however, that the above equation was unable to describe experimental data. Therefore he changed the series expansion to

$$P\nu = A + \frac{B}{\nu} + \frac{C}{\nu^2} + \frac{D}{\nu^4} + \frac{E}{\nu^6} + \frac{F}{\nu^8} \tag{3.2}$$

where the coefficients $A, B, C, \dots$ are virial coefficients dependent on temperature. However Onnes was only able to obtain a limited number of terms for this series.

Instead, experimental data was used to determine the coefficients in equation (3.2), now referred to as virial coefficients, as a function of inverse temperature [98].

$$B = b_1 + \frac{b_2}{T} + \frac{b_3}{T^2} + \frac{b_4}{T^3} + \frac{b_5}{T^4} \tag{3.3}$$

Onnes determined the value of the virial coefficients by using experimental data from hydrogen, oxygen, nitrogen and ether [99]. The resulting equation of state contained

25 parameters, but was an equation of state describing an arbitrary substance [95].

Later it was shown that statistical mechanics can be used to derive virial coefficients in terms of deviations away from the ideal gas, when particles interact via a pair potential. The interactions of particles can be represented by cluster integrals, each virial coefficient representing the collision of two, three, four and so on particles.

In this section, a Monte Carlo (MC) hit and miss algorithm is developed for the calculation of virial coefficients up to the fifth virial coefficient B_5, using Mayer and Ree-Hoover diagrams. The algorithm is tested against well known systems, the HD, HS and square well. It was found to accurately predict the first five virial coefficients for HD and HS system using both Mayer and Ree-Hoover diagrams. It also correctly predicted diagrams known analytically for the three dimensional square well.

Being satisfied that the algorithm is working correctly, virial coefficients were calculated for all selected potentials in two and three dimensions and then fitted by an inverse temperature fit. Using the coefficients for the inverse temperature fit, liquid-vapour domes and JT inversion curves were calculated. It was observed that, in general, the critical temperature would decrease with the decrease of the length of the potential, but having the density region, especially the critical density, remain much the same, as well as being significantly smaller in two dimensions compared to three. The predicted JT inversion curves are significantly narrower in their temperature range in two dimensions compared to three dimensions and seem to have an overall tendency to narrow when decreasing the cut off range.

3.1 Virial equation of state from Mayer cluster expansion

A virial EoS can be developed from statistical mechanics, where the relation between pressure P and the partition function Z is considered. This section will use the statistical mechanics approach, starting from the partition function for a classical gas of N identical particles.

$$Z_N = \frac{1}{N!\lambda^{3N}} \int W_N(\mathbf{r}^N) d\mathbf{r}^N = W_N/\lambda^{3N} \tag{3.4}$$

where $\lambda^2 = h^2/2\pi m k_B T$ with h being Planck's constant, $W_N = \exp(-\phi(\mathbf{r}^N)/k_B T)$ being the Boltzmann factor and $Z_N = \frac{1}{N} \int W_N(\mathbf{r}^N) d\mathbf{r}^N$ the configurational integral. The main concern is to develop the configurational integral, which depends on the number of particles and the Boltzmann factor. The configurational integral cannot be analytically calculated for a general potential. A method of approximating the configurational integral is by using Mayer-cluster expansions, which are corrections to the ideal gas. Mayer f-functions, which are the connection between two interacting particles, are defined by.

$$f_{ij} = e^{-\beta\phi(r_{ij})} - 1 \tag{3.5}$$

and shown schematically in figure 3.1 for an arbitary potential. The effect of f_{ij} on the configurational integral will always be small, as either the potential is small, or it is short ranged. The Boltzmann factor W_N in the partition function depends
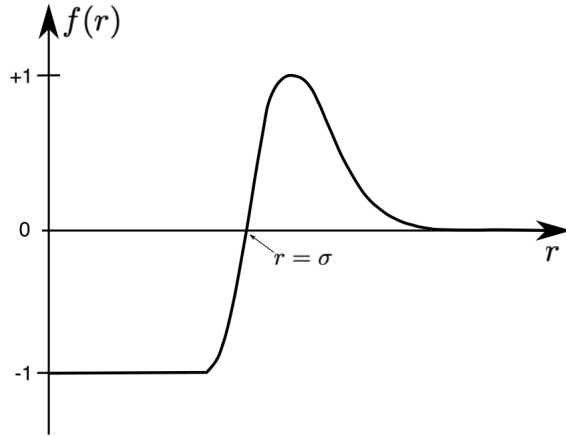
Figure 3.1: Mayer f-bond for an arbitrary potential.

on the potential. For a pairwise additive potential, it is possible to write the total potential energy as a sum, $\frac{1}{2}\sum_{i=1} \phi_i$, so that the Boltzmann factor can be written in terms of the Mayer f-functions

$$e^{-\beta\phi} = e^{-\beta\sum\phi_i} = \prod_i e^{-\beta\phi_i} = \prod_{i<j}(1 + f_{ij}) \tag{3.6}$$

In the micro-canonical ensemble (NVE ensemble), the configurational integral can be expressed in terms of Mayer f-functions

$$Z_N = \int \cdots \int \prod_{i<j} (1 + f_{ij}) d^{3N} r \qquad (3.7)$$

Expanding the product in the integrand, this becomes

$$Z_N = \int \cdots \int \left[1 + \sum_{i<j} f_{ij} + \sum_{i<j,k<l;i,j\neq l,k} f_{ij} f_{lk} + \ldots \right] d^{3N} r. \qquad (3.8)$$

For example, for $N = 3$,

$$Z_3 = \int_V \left[1 + f_{12} + f_{13} + f_{23} + f_{13} f_{12} + f_{12} f_{23} + f_{13} f_{23} + f_{12} f_{23} f_{13} \right] d^3 r \qquad (3.9)$$

When integrating Z_3 over all volume the first term simply becomes V^3. If the volume available is greater than the range of the potential, integrating f_{12}, f_{13} and f_{23} gives a value proportional to V^2. If the volume is large, terms proportional to V^2 become significantly smaller than the initial term proportional to V^3. The remaining terms are only non zero if all three particles interact [100]. It is now possible to relate the partition function to the pressure

$$\frac{PV}{K_B T} = \ln Z_N = \ln \left[\sum_{N=0}^{\infty} \frac{1}{N!} \left(\frac{Z}{\lambda^3} \right)^N W_N \right]. \qquad (3.10)$$

The natural logarithm of the micro-canonical partition function is then given by the sum

$$\ln Z = \sum (\text{counting factor}) \times (\text{cluster integral}). \qquad (3.11)$$

where the counting factors eliminate overcounting. This gives rise to the pressure being expressed as a power series in density

$$P/k_B T = \rho \left[1 - \sum_{l=1}^{\infty} \frac{l}{l+1} \beta_l \rho^l \right] \qquad (3.12)$$

where $\beta_l = (1/l!)(\sum \text{connected, irreducible cluster diagrams})$ with the position of particle 1 fixed. An example of cluster diagrams with particle 1 fixed in position for

three particles were shown in section 1.2 in figure 1.24. An irreducible diagram is one where removing any one connection does not result in separating the diagram. A virial coefficient B_N is then related to the cluster β_l by

$$B_N = \frac{l}{l+1}\beta_l \tag{3.13}$$

It is now possible to write the virial EoS as an infinite power expansion in density

$$P/k_B T = \rho + \sum_{N \geq 2}^{\infty} B_N(T)\rho^N \tag{3.14}$$

In this study, the virial equation of state has been truncated at the fifth virial coefficient, giving the expression

$$\frac{P}{\rho k_B T} = 1 + B_2(T)\rho + B_3(T)\rho^2 + B_4(T)\rho^3 + B_5(T)\rho^4 \tag{3.15}$$

All that remains is the calculation of the individual virial coefficients, using the cluster diagrams.

3.2 Calculating individual virial coefficients

Each virial coefficient can be represented by a diagram of N particles connected by Mayer f-functions. Lower order coefficients for some simple pair potentials like HS and SW, can be calculated analytically. For the pair potentials chosen for this study, an analytical approach is not possible. Each individual diagram contributing to a coefficient is calculated using a MC hit and miss algorithm. The basis of any MC algorithm is a random number generator. The one used for these calculations is given in appendix B. The calculations of the virial coefficients will be considered separately using Mayer diagrams, only the fourth and fifth coefficient will employ Ree-Hoover diagrams to reduce the number of diagrams required.

3.2.1 The second virial coefficient

For the second virial coefficient, the interaction between two particles is considered. There is only one way two points can be connected to each-other, therefore the only contribution to B_2 is the diagram shown in figure 3.2. The integral to which the

Figure 3.2: Mayer diagram contributing to B_2

diagram corresponds is

$$B_2 = -2\pi \int_0^\infty \left(e^{-\phi(r_{ij})/k_B T} \right) r^2 \mathrm{d}r \tag{3.16}$$

This integral may be evaluated for any potential, by numerical integration. In this work a 16 point Gauss Legendre curvature was used.

3.2.2 The third virial coefficient

Only one diagram contributes to B_3 in the cluster integral

$$b_2 = \frac{1}{2} \iint f_{12} f_{13} f_{23} \mathrm{d}r_{12} \mathrm{d}r_{13} \tag{3.17}$$

It is shown in figure 3.3. B_3 can still be calculated using numerical integration, but here it was done using MC hit and miss. It is clear from the diagram that the bonds
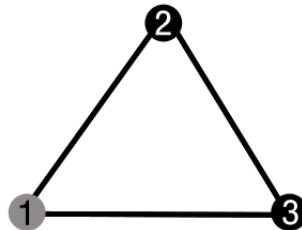
Figure 3.3: Mayer diagram contributing to B_3, having particle 1 fixed at the origin. The solid lines represent a Mayer f-bond.

making up the diagram are f_{12}, f_{13} and f_{23}. Calculating the diagram via MC hit and miss was done by placing particle 1 at the origin (0,0). Particle 2 and 3 were

randomly placed within a circle of radius r_{cut}, centred at particle 1, as illustrated in figure 3.4.
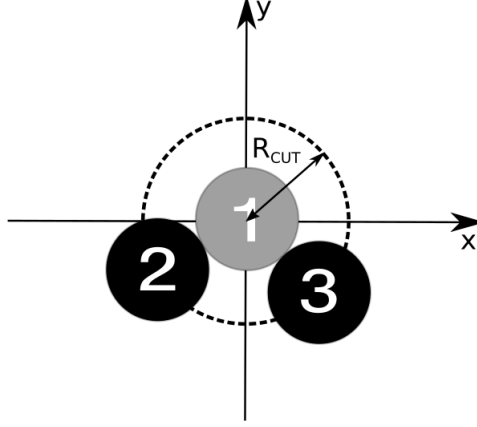
Figure 3.4: Monte Carlo Hit and Miss placement of the third viral coefficient B_3 in two dimensions, which particle 1 fixed at the origin.

Since particle 2 and 3 are deliberately placed within the cut-off distance of particle 1, their Mayer f-bond with particle 1 will always be non zero. The Mayer f-bond corresponding to the interaction of particles 2 and 3 could, however, be zero. The random placement of particles making up the diagram is repeated in the region of 10^{10} times and averaged. The averages have the following relation to B_3

$$\frac{\langle f_{12} f_{13} f_{23} \rangle}{\langle f_{12} f_{13} \rangle} = \frac{-3B_3}{4B_2^2} \tag{3.18}$$

The left hand side is the result of the MC hit and miss algorithm, the value of B_2 is known from numerical integration. B_3 is therefore

$$\frac{B_3}{B_2^2} = -\frac{4\langle f_{12} f_{13} f_{23} \rangle}{3\langle f_{12} f_{13} \rangle} \tag{3.19}$$

This general approach is repeated for the following higher order virials.

3.2.3 The fourth virial coefficient

Considering the connection of four particles, when particle one is in a fixed position, there are three different relevant diagrams D_1, D_2 and D_3 contributing to B_4, as illustrated in figure 3.5.

51
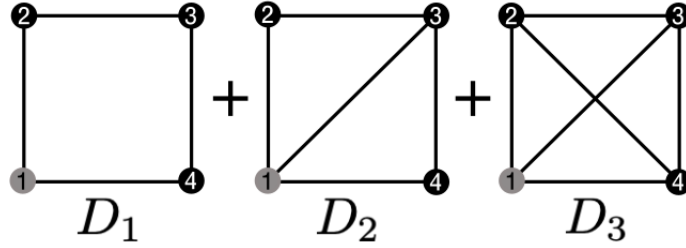
Figure 3.5: The three diagrams contributing contributing to the fourth virial coefficient B_4. In each case the position of particle 1 is fixed during hit and miss Monte Carlo calculations.

Similar to the calculation of B_3, although with a fourth particle added, B_4 is determined by placing particle 1 at the origin, particle 2 within the cut-off distance of particle 1, particle four within cut-off of particle 1 and lastly particle 3 placed within cut-off of particle 2, as illustrated in figure 3.6. The MC hit and miss ratio
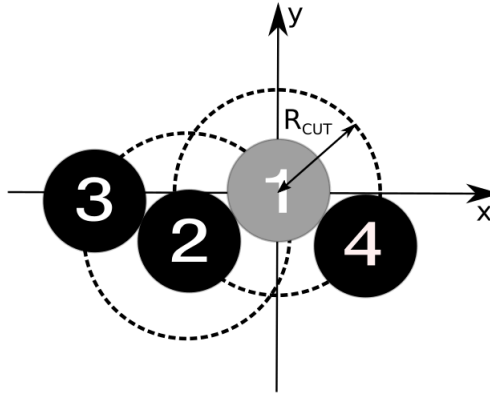
Figure 3.6: MC placements of four particles. Particle 1 placed at origin (0,0) and particle 4 and 2 always within the cut-off of particle 1.

results have the following relation to the three diagrams: The first diagram D_1 has only four Mayer f-bonds

$$D_1 = -\frac{3}{8} \iiiint_V f_{12} f_{23} f_{34} f_{14} \mathrm{d}r_{12} \mathrm{d}r_{23} \mathrm{d}r_{34} \mathrm{d}r_{14} \tag{3.20}$$

relating the diagram to the hit and miss MC

$$\frac{\langle f_{12} f_{23} f_{34} f_{14} \rangle}{\langle f_{12} f_{23} f_{14} \rangle} = \frac{D_1}{3B_2^3} \tag{3.21}$$

The second diagram D_2 has five Mayer f-bonds

$$D_2 = -\frac{6}{8} \iiint \iint_V f_{12} f_{13} f_{14} f_{23} f_{34} \mathrm{d}r_{12} \mathrm{d}r_{13} \mathrm{d}r_{14} \mathrm{d}r_{23} \mathrm{d}r_{34} \tag{3.22}$$

$$\frac{\langle f_{12} f_{13} f_{14} f_{23} f_{34} \rangle}{\langle f_{12} f_{14} f_{23} \rangle} = \frac{D_2}{6 B_2^3} \tag{3.23}$$

Finally the third diagram D_3 is a full star diagram, having six Mayer f-bonds

$$D_3 = -\frac{1}{8} \iiint \iiint_V f_{12} f_{13} f_{14} f_{23} f_{24} f_{34} \mathrm{d}r_{12} \mathrm{d}r_{13} \mathrm{d}r_{14} \mathrm{d}r_{23} \mathrm{d}r_{24} \mathrm{d}r_{34} \tag{3.24}$$

$$\frac{\langle f_{12} f_{13} f_{14} f_{23} f_{24} f_{34} \rangle}{\langle f_{12} f_{14} f_{23} \rangle} = \frac{D_3}{B_2^3} \tag{3.25}$$

B_4 only has three diagrams contributing, but as will be seen in the next section for the fifth virial coefficient, the number of contributing diagrams steadily increases, heavily impacting on computation time.

Ree and Hoover [101] introduced the Ree-Hoover bonds $\tilde{f}$-bonds, in connection with the Mayer bonds, to not only consider particles which are connected but also those which are not. This method reduced the number of diagrams contributing to higher order virials. The relation between and f-bonds and $\tilde{f}$-bonds is

$$\tilde{f}_{ij} = f_{ij} + 1 \tag{3.26}$$

For each pair of particles not connected, the integrand is multiplied by $(\tilde{f}_{ij} - f_{ij}) = 1$. This trick reduced the diagrams contributing to B_4 by one, which might not sound significant but the effect for higher coefficients is much larger. The two Ree-Hoover diagrams contributing are shown in figure 3.7. Note that the naming of the diagrams have changed to Ree-Hoover notation, the number in brackets represents the number of particles in the diagram and the subscript the number of Ree-Hoover bonds (shown as broken lines).

The Ree-Hoover diagrams contributing to B_4 contains of the following products of f- and $\tilde{f}$-bonds

$$\langle 4 \rangle_0 = f_{12} f_{13} f_{14} f_{23} f_{24} f_{34} \tag{3.27}$$

$\langle 4 \rangle_0 \qquad \langle 4 \rangle_2$
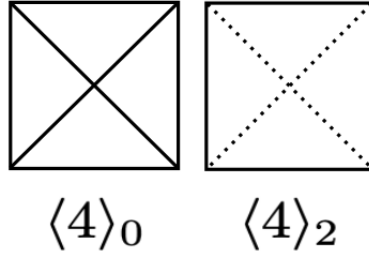
Figure 3.7: The two Ree-Hoover diagrams contributing to the calculation of B_4, having the same particle numbering as the Mayer-Diagrams.

$$\langle 4 \rangle_2 = f_{12}\tilde{f}_{13}f_{14}f_{23}\tilde{f}_{24}f_{34} \tag{3.28}$$

The MC hit and miss calculation remains much the same when using Ree-Hoover diagrams, particle 1 is still placed at the origin and the remaining particles placed around it.

3.2.4 The fifth virial coefficient

There are ten relevant Mayer diagrams for B_5, which are displayed in figure 3.8. The placement of the five particles is shown in figure 3.9.
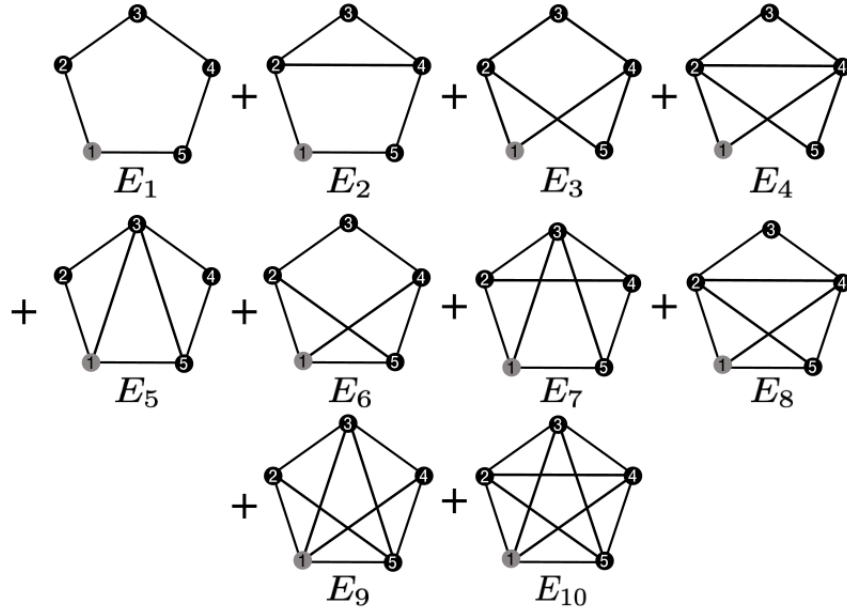
Figure 3.8: Mayer diagrams contributing to the fifth virial coefficient. In each case the position of particle 1 is fixed.

The ten integrals and MC hit and miss ratios for the Mayer diagrams are given
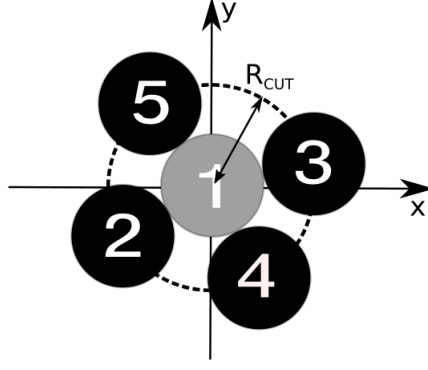
Figure 3.9: Placement of five particles calculating diagrams relating to the fifth virial coefficient. Particle 1 placed at origin and the remaining four all placed within cut off distance R_{CUT} of particle 1.

by

$$E_1 = -\frac{12}{30} \iiint\int \int_V f_{12}f_{15}f_{23}f_{34}f_{45}\mathrm{d}r_{12}\mathrm{d}r_{15}\mathrm{d}r_{23}\mathrm{d}r_{34}\mathrm{d}r_{45} \tag{3.29}$$

$$\frac{\langle f_{12}f_{15}f_{23}f_{34}f_{45}\rangle}{\langle f_{12}f_{13}f_{14}f_{15}\rangle} = \frac{30E_1}{12B_2^4} \tag{3.30}$$

$$E_2 = -2 \iiint \iiint_V f_{12}f_{15}f_{23}f_{24}f_{34}f_{45}\mathrm{d}r_{12}\mathrm{d}r_{15}\mathrm{d}r_{23}\mathrm{d}r_{34}\mathrm{d}r_{24}\mathrm{d}r_{34}\mathrm{d}r_{45} \tag{3.31}$$

$$\frac{\langle f_{12}f_{15}f_{23}f_{24}f_{34}f_{45}\rangle}{\langle f_{12}f_{13}f_{14}f_{15}\rangle} = \frac{E_2}{2B_2^4} \tag{3.32}$$

$$E_3 = -\frac{1}{3} \iiint \iiint_V f_{12}f_{14}f_{23}f_{25}f_{34}f_{45}\mathrm{d}r_{12}\mathrm{d}r_{14}\mathrm{d}r_{23}\mathrm{d}r_{25}\mathrm{d}r_{34}\mathrm{d}r_{45} \tag{3.33}$$

$$\frac{\langle f_{12}f_{14}f_{23}f_{25}f_{34}f_{45}\rangle}{\langle f_{12}f_{13}f_{14}f_{15}\rangle} = \frac{3E_3}{B_2^4} \tag{3.34}$$

$$E_4 = -\frac{1}{3} \iiiint \iiint_V f_{12}f_{14}f_{23}f_{24}f_{25}f_{34}f_{45}\mathrm{d}r_{12}\mathrm{d}r_{14}\mathrm{d}r_{23}\mathrm{d}r_{34}\mathrm{d}r_{25}\mathrm{d}r_{34}\mathrm{d}r_{45} \tag{3.35}$$

$$\frac{\langle f_{12}f_{14}f_{23}f_{24}f_{25}f_{34}f_{45}\rangle}{\langle f_{12}f_{13}f_{14}f_{15}\rangle} = \frac{3E_4}{B_2^4} \tag{3.36}$$

$$E_4 = -2 \iiiint \iiint_V f_{12}f_{13}f_{15}f_{23}f_{34}f_{35}f_{45}\mathrm{d}r_{12}\mathrm{d}r_{13}\mathrm{d}r_{15}\mathrm{d}r_{23}\mathrm{d}r_{34}\mathrm{d}r_{35}\mathrm{d}r_{45} \tag{3.37}$$

$$\frac{\langle f_{12}f_{13}f_{15}f_{23}f_{34}f_{35}f_{45}\rangle}{\langle f_{12}f_{13}f_{14}f_{15}\rangle} = \frac{E_4}{2B_2^4} \tag{3.38}$$

$$E_6 = - \iiiint \iiint_V f_{12}f_{14}f_{15}f_{23}f_{25}f_{34}f_{45}\mathrm{d}r_{12}\mathrm{d}r_{14}\mathrm{d}r_{15}\mathrm{d}r_{23}\mathrm{d}r_{25}\mathrm{d}r_{34}\mathrm{d}r_{45} \tag{3.39}$$

$$\frac{\langle f_{12}f_{14}f_{15}f_{23}f_{25}f_{34}f_{45}\rangle}{\langle f_{12}f_{13}f_{14}f_{15}\rangle} = \frac{E_6}{B_2^4} \tag{3.40}$$

$$E_7 = -\frac{1}{2} \iiiint \iiiint \int_V f_{12}f_{13}f_{15}f_{23}f_{24}f_{34}f_{35}f_{45}\mathrm{d}r_{12}\mathrm{d}r_{13}\mathrm{d}r_{15}\mathrm{d}r_{23}\mathrm{d}r_{24}\mathrm{d}r_{34}\mathrm{d}r_{35}\mathrm{d}r_{45}$$

$$(3.41)$$

$$\frac{\langle f_{12}f_{13}f_{15}f_{23}f_{24}f_{34}f_{35}f_{45}\rangle}{\langle f_{12}f_{13}f_{14}f_{15}\rangle} = \frac{2E_7}{B_2^4} \qquad (3.42)$$

$$E_8 = -\frac{30}{30} \iiiint \iiiint_V f_{12}f_{14}f_{15}f_{23}f_{24}f_{25}f_{34}f_{45}\mathrm{d}r_{12}\mathrm{d}r_{14}\mathrm{d}r_{15}\mathrm{d}r_{23}\mathrm{d}r_{24}\mathrm{d}r_{25}\mathrm{d}r_{34}\mathrm{d}r_{45}$$

$$(3.43)$$

$$\frac{\langle f_{12}f_{14}f_{15}f_{23}f_{24}f_{25}f_{34}f_{45}\rangle}{\langle f_{12}f_{13}f_{14}f_{15}\rangle} = \frac{E_8}{B_2^4} \qquad (3.44)$$

$$E_9 = -\frac{10}{30} \iiiint \iiiint \int_V f_{12}f_{13}f_{14}f_{15}f_{23}f_{25}f_{34}f_{35}f_{45}\mathrm{d}r_{12}\mathrm{d}r_{13}\mathrm{d}r_{14}\mathrm{d}r_{15}\mathrm{d}r_{23}\mathrm{d}r_{25}$$

$$\mathrm{d}r_{34}\mathrm{d}r_{35}\mathrm{d}r_{45}$$

$$(3.45)$$

$$\frac{\langle f_{12}f_{13}f_{14}f_{15}f_{23}f_{25}f_{34}f_{35}f_{45}\rangle}{\langle f_{12}f_{13}f_{14}f_{15}\rangle} = \frac{3E_9}{B_2^4} \qquad (3.46)$$

$$E_{10} = -\frac{1}{30} \iiiint \iiiint \iint^V f_{12}f_{13}f_{14}f_{15}f_{23}f_{24}f_{25}f_{34}f_{35}f_{45}\mathrm{d}r_{12}\mathrm{d}r_{13}\mathrm{d}r_{14}\mathrm{d}r_{15}$$

$$\mathrm{d}r_{23}\mathrm{d}r_{24}\mathrm{d}r_{25}\mathrm{d}r_{34}\mathrm{d}r_{35}\mathrm{d}r_{45}$$

$$(3.47)$$

$$\frac{\langle f_{12}f_{13}f_{14}f_{15}f_{23}f_{24}f_{25}f_{34}f_{35}f_{45}\rangle}{\langle f_{12}f_{13}f_{14}f_{15}\rangle} = \frac{30E_{10}}{B_2^4} \qquad (3.48)$$

The benefit of switching to Ree-Hoover diagrams when calculating B_5 is much more obvious, as the number of diagrams contributing reduces by a factor of two. The Ree-Hoover diagrams contributing to B_5 are shown in figure 3.10.
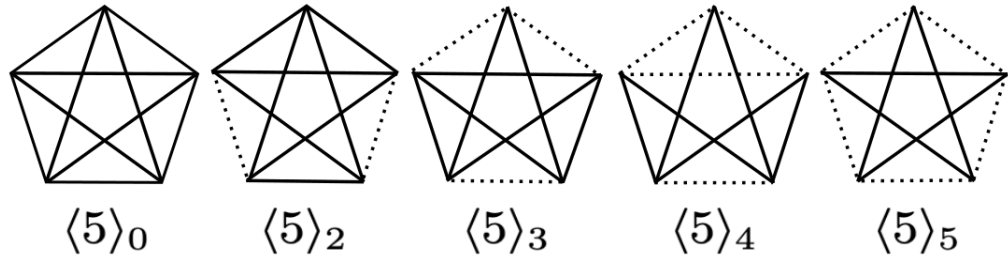
Figure 3.10: Ree-Hoover diagram contributing to B_5, having the same particle numbering as the Mayer diagrams.

The diagram $\langle 5\rangle_0$ contains no Ree-Hoover bonds and is essentially equal to the Mayer diagram E_{10}. It cannot be modified into a Ree-Hoover bond as it is already

fully connected.

$$\langle 5 \rangle_0 = E_{10} \tag{3.49}$$

The remaining Ree-Hoover diagrams have the following integrals and MC calculated ratios

$$\langle 5 \rangle_2 = -\frac{1}{24} \iiiint \iiiint \iint^V \tilde{f}_{12} f_{13} f_{14} f_{15} f_{23} f_{24} f_{25} f_{34} f_{35} \tilde{f}_{45}$$
$$\mathrm{d}r_{12}\mathrm{d}r_{13}\mathrm{d}r_{14}\mathrm{d}r_{15}\mathrm{d}r_{23}\mathrm{d}r_{24}\mathrm{d}r_{25}\mathrm{d}r_{34}\mathrm{d}r_{35}\mathrm{d}r_{45} \tag{3.50}$$

$$\frac{\langle \tilde{f}_{12} f_{13} f_{14} f_{15} f_{23} f_{24} f_{25} f_{34} f_{35} \tilde{f}_{45} \rangle}{\langle f_{13} f_{14} f_{25} f_{35} \rangle} = \frac{-24\langle 5 \rangle_2}{B_2^4} \tag{3.51}$$

$$\langle 5 \rangle_3 = \frac{1}{32} \iiiint \iiiint \iint^V f_{12} f_{13} f_{14} \tilde{f}_{15} \tilde{f}_{23} f_{24} f_{25} \tilde{f}_{34} f_{35} f_{45}$$
$$\mathrm{d}r_{12}\mathrm{d}r_{13}\mathrm{d}r_{14}\mathrm{d}r_{15}\mathrm{d}r_{23}\mathrm{d}r_{24}\mathrm{d}r_{25}\mathrm{d}r_{34}\mathrm{d}r_{35}\mathrm{d}r_{45} \tag{3.52}$$

$$\frac{\langle f_{12} f_{13} f_{14} \tilde{f}_{15} \tilde{f}_{23} f_{24} f_{25} \tilde{f}_{34} f_{35} f_{45} \rangle}{\langle f_{13} f_{14} f_{25} f_{35} \rangle} = \frac{32\langle 5 \rangle_3}{B_2^4} \tag{3.53}$$

$$\langle 5 \rangle_4 = -\frac{3}{16} \iiiint \iiiint \iint^V f_{12} f_{13} f_{14} \tilde{f}_{15} \tilde{f}_{23} \tilde{f}_{24} f_{25} \tilde{f}_{34} f_{35} f_{45}$$
$$\mathrm{d}r_{12}\mathrm{d}r_{13}\mathrm{d}r_{14}\mathrm{d}r_{15}\mathrm{d}r_{23}\mathrm{d}r_{24}\mathrm{d}r_{25}\mathrm{d}r_{34}\mathrm{d}r_{35}\mathrm{d}r_{45} \tag{3.54}$$

$$\frac{\langle f_{12} f_{13} f_{14} \tilde{f}_{15} \tilde{f}_{23} \tilde{f}_{24} f_{25} \tilde{f}_{34} f_{35} f_{45} dr_{12} \rangle}{\langle f_{13} f_{14} f_{25} f_{35} \rangle} = -\frac{16\langle 5 \rangle_4}{3B_2^4} \tag{3.55}$$

$$\langle 5 \rangle_5 = -\frac{5}{32} \iiiint \iiiint \iint^V \tilde{f}_{12} f_{13} f_{14} \tilde{f}_{15} \tilde{f}_{23} f_{24} f_{25} \tilde{f}_{34} f_{35} \tilde{f}_{45}$$
$$\mathrm{d}r_{12}\mathrm{d}r_{13}\mathrm{d}r_{14}\mathrm{d}r_{15}\mathrm{d}r_{23}\mathrm{d}r_{24}\mathrm{d}r_{25}\mathrm{d}r_{34}\mathrm{d}r_{35}\mathrm{d}r_{45} \tag{3.56}$$

$$\frac{\langle \tilde{f}_{12} f_{13} f_{14} \tilde{f}_{15} \tilde{f}_{23} f_{24} f_{25} \tilde{f}_{34} f_{35} \tilde{f}_{45} \rangle}{\langle f_{13} f_{14} f_{25} f_{35} \rangle} = \frac{-32\langle 5 \rangle_5}{5B_2^4} \tag{3.57}$$

Although the overall algorithm for calculating Ree-Hoover diagrams remains the same, the common denominator used in the ratio for the MC calculations has to change. If a f bond in the denominator also appears as a $\tilde{f}$, divisions by zero will happen as particles always connected by f bonds are never connected when being a $\tilde{f}$-bond, hence always zero. Figure 3.11 shows the MC placement of particles for the Ree-Hoover non zero bonds. Extra care must be taken in programming to ensure

that particles are allowed to be placed in the entire region of the integral. This can either be achieved by extending the cut-off region to correspond to the furthest particles placement, in the case of B_5 that being three times the normal cut-off distance. A more computationally economical way is to place each particle so that it is within the cut off radius of the particle to which it must be connected according to the diagram. In other words, for B_5 only particles 3 and 4 are connected to particle 1. Particle 5 is placed to be within the cut off distance from particle 3, and similarly, particle 2 placed to be within the cut off distance from particle 5. This increases the number of successfully placed particles. As illustrated in figure 3.11.
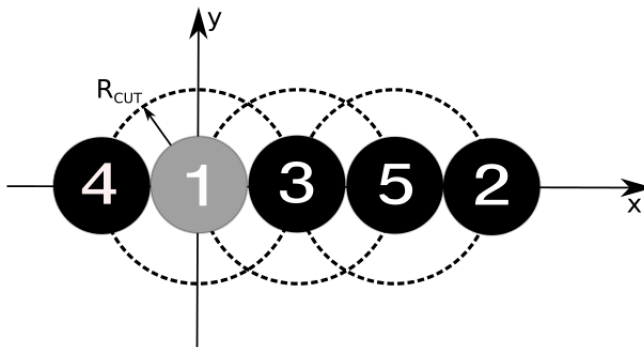
Figure 3.11: Random placement of Monte Carlo particles for non-zero connecting particles, for Ree-Hoover diagrams.

3.3 Verification of virial coefficients

To test the validity of the MC hit and miss algorithm for calculating virial coefficients, a couple of tests were done. Firstly it was tested on the HS and HD system, as these coefficients are known very accurately, most notably in the work by Kratky [88, 102] and Hoover [101].

3.3.1 The Hard Sphere test

Comparing the MC hit and miss algorithm's performance to the HS and HD system is convenient as this system has well known virial coefficients. Values were obtained for B_3, B_4 and B_5 using Mayer diagrams compared to values obtained by Kratky [88], which are shown in table 2. B_4 and B_5 were also calculated using Ree-Hoover diagrams, compared to values obtained by Ree and Hoover [101], shown in table 3.

Individual values for the five Ree-Hoover diagrams contributing to B_5 are included in table 5.

B_n/B_2^{n-1}	HD Kratky	This work	HS Kratky	This work
B_3/B_2^2	0.7820044	0.7820008 ± 0.0014	0.625	0.625 ± 0.003
B_4/B_2^3	0.5322318	0.5321862 ± 0.05	0.2869495	0.2869886 ± 0.053
B_5/B_2^4	0.3335561	0.3335183 ± 0.924	0.110252	0.110539 ± 0.770

Table 2: Mayer Diagram comparison with values obtained by Kratky [88].

B_n/B_2^{n-1}	HD Ree-Hoover	This work	HS Ree-Hoover	This work
B_4/B_2^3	0.5327	0.5322 ± 0.019	0.28695	0.28699 ± 0.040
B_5/B_2^4	0.338	0.334 ± 0.026	0.1103	0.1103 ± 0.1057

Table 3: Ree-Hoover Diagram comparison with using values obtained by Ree and Hoover [101].

Diagram	HD Ree-Hoover	This work
$\langle 5 \rangle_0$	(1.809 ± 0.002)	(1.809 ± 0.034)
$\langle 5 \rangle_2$	$(1.77 \pm 0.01) \times 10^{-2}$	$(1.77 \pm 0.05) \times 10^{-2}$
$\langle 5 \rangle_3$	$-(5.11 \pm 0.05) \times 10^{-3}$	$(-5.09 \pm 0.05) \times 10^{-3}$
$\langle 5 \rangle_4$	0	0
$\langle 5 \rangle_5$	$-(2.15 \pm 0.03) \times 10^{-2}$	$(-2.11 \pm 0.05) \times 10^{-2}$

Table 4: Values of individual Ree-Hoover diagrams, contributing to B_5 for HD [101].

Diagram	HS Ree-Hoover	This work
$\langle 5 \rangle_0$	(0.711 ± 0.01)	0.711 ± 0.058
$\langle 5 \rangle_2$	$(2.092 \pm 0.009) \times 10^{-2}$	$(2.108 \pm 0.113) \times 10^{-2}$
$\langle 5 \rangle_3$	$-(8.25 \pm 0.05) \times 10^{-3}$	$(-8.27 \pm 0.193) \times 10^{-3}$
$\langle 5 \rangle_4$	$(7.1 \pm 0.04) \times 10^{-4}$	$(7.3 \pm 0.8) \times 10^{-4}$
$\langle 5 \rangle_5$	$-(4.05 \pm 0.03) \times 10^{-2}$	$(-4.11 \pm 0.19) \times 10^{-2}$

Table 5: Values of individual Ree-Hoover diagrams, contributing to B_5 for HS [101].

It is seen that the MC hit and miss algorithm calculates the virial coefficients from B_2 to B_5 which agree well with the literature, both using Mayer and Ree-Hoover diagrams. It's to be expected that the values obtained in this study should compare well with literature, but not be identical, as they have obtained even more accurate values by using the symmetry of the HS/HD potential, to reduce the number of diagrams contributing even further. This symmetry is not present for the potentials studied in this work, therefore the reduction in diagrams was not made. Only a very

small increase is observed in accuracy switching to Ree-Hoover diagrams. However, it improves computational time, since only half the number of Mayer diagrams need to be calculated. A typical calculation time for one temperature for B_5 using Mayer diagrams is about an hour in CPU cost.

3.3.2 The Square Well test.

The MC hit and miss algorithm performed well for the HS and HD system, but this did not test its performance on a temperature dependent system. The three dimensional square well is ideal as a test system, as it has a temperature dependence and analytical expressions are known for the second and third virial coefficients for the square well. Analytical expressions are known only for D_1 and D_2 from the work of Barker and Monaghan [103]. The second virial coefficient is easily derived and given as

$$B_2(T) = \frac{2\pi\sigma^3}{3}[1 + h(\lambda^3 - 1)] \tag{3.58}$$

where $h = 1 - e^{\beta\epsilon}$. The third virial coefficients is given by

$$
\begin{aligned}
B_3(T) = -\frac{B_2(T)^2}{8}(-5 + 17h + h^2[-32\lambda^3 + 18\lambda^2 + 48] \\
+ h^3[5\lambda^6 - 32\lambda^3 + 18\lambda^2 + 26])
\end{aligned}
\tag{3.59}
$$

Analytical expressions for D_1 and D_2 for $\lambda = 2$ are

$$D_1 = -(B_2^3/560)(544 - 4075h + 35007h^2 - 99687h^3 + 139215h^4); \tag{3.60}$$

$$
\begin{aligned}
D_2 = -(B_2^3/4480)(-6347 + 27369h - 184156h^2 + 594272h^3 \\
-1518980h^4 + 918540h^5);
\end{aligned}
\tag{3.61}
$$

The analytical virials compared to results obtained by MC hit and miss algorithm are shown in figure 3.12. Recall that B_2 is not calculated using the hit and miss algorithm, but the chosen integration scheme yields excellent agreement with the analytical result. Good agreement is also observed for B_3, D_1 and D_2.
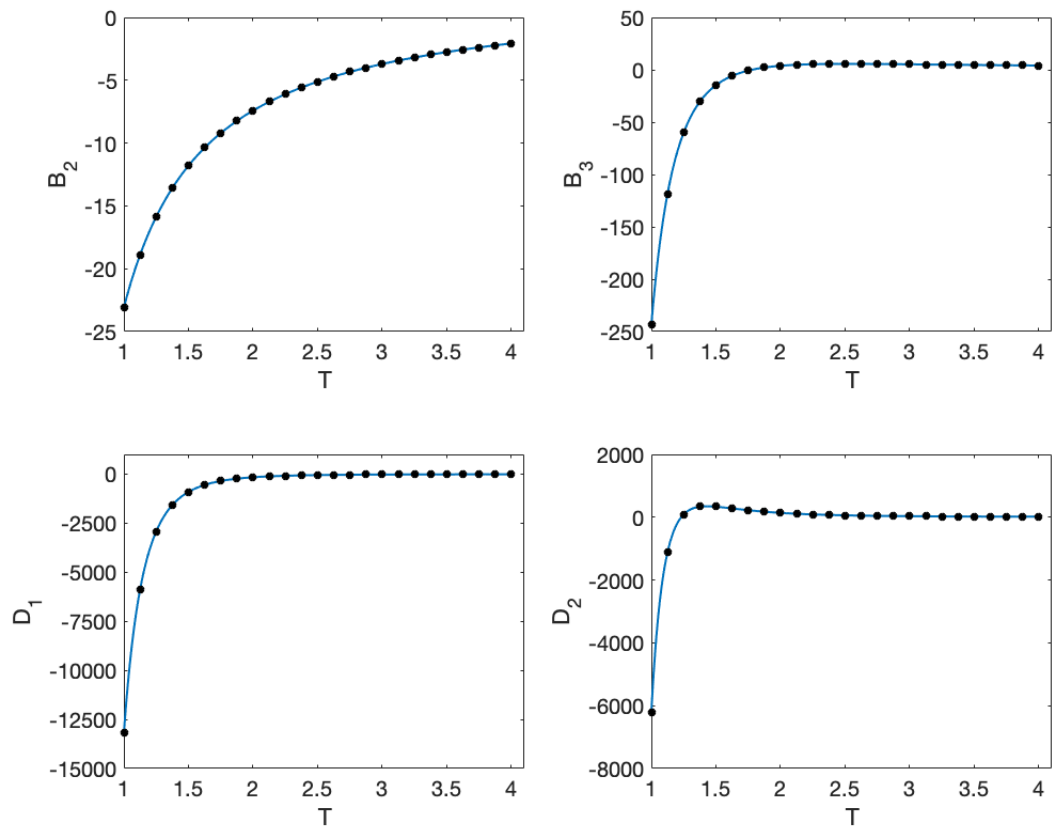
Figure 3.12: 3D square well results, analytical solution (solid line) and MC hit and miss calculations (dots), showing results for the second, third virial coefficient and two out of three Mayer diagrams D_1 and D_2 which contribute to the fourth virial coefficient. The unit temperatures are in LJ reduced units.

3.4 Virial coefficient results for inverse fit of temperature.

The hit and miss MC algorithm calculates a single virial coefficient for a set temperature, typically requiring 10^{10} MC iterations for a temperature range in LJ reduced units $0.1 \leq T \leq 0.9$ with between $150 - 300$ intermediate temperatures, dependent on whether or not features like a steep peak appear, which required more points. To then obtain the coefficient for a given potential for a range of temperatures, each virial coefficient can be expressed as an inverse temperature fit, which can be then be inserted into a virial equation of state. The inverse temperature fit is given by the polynomial

$$B_N(T) = \sum_{i=1}^{11} a_i \times T^{-i}. \tag{3.62}$$

The curve fitting was done using the MATLAB (R2018b) curve fitting tool, the goodness of fit [104] being determined by the sum of squares due to error (SSE), with a value closer to zero indicating that the fit predicts the data better. The alternative measure, R^2, takes a value between 0 and 1, where a value closer to 1 indicates that a greater percentage of the data is explained by the fit. It is worth noting that if a high number of coefficients are used for the fit, R^2 will tend to 1 without the fit actually improving. Therefore it is a good idea to use the adjusted R^2, which accounts for the large number of coefficients. The Root Mean Squared Error (RMSE) can also be used, where a value closer to 0 indicates a good fit.

The individual coefficients for each of the members of the mn and LJ/s families in two and three dimensions will be plotted against temperature. Associated with each B_n vs. T plot is a table to show the goodness of fit and a table of a_i coefficient values.

The three members of the mn-potential family are identified by their m value. The LJ/s potentials are identified by their cut-off range (r_c). Section 3.5.3 provides a comparison of how the liquid-vapour coexistence dome and Joule-Thomson inversion curves varies with changing well width, cut off range and dimension.

3.4.1 Virial coefficients for the *mn*-family

The virial results for 2D and 3D for the five virial coefficients for the *mn*-potential with $m = 4$, are displayed against temperature in figure 3.13 and their respective inverse temperature fits in table 6.
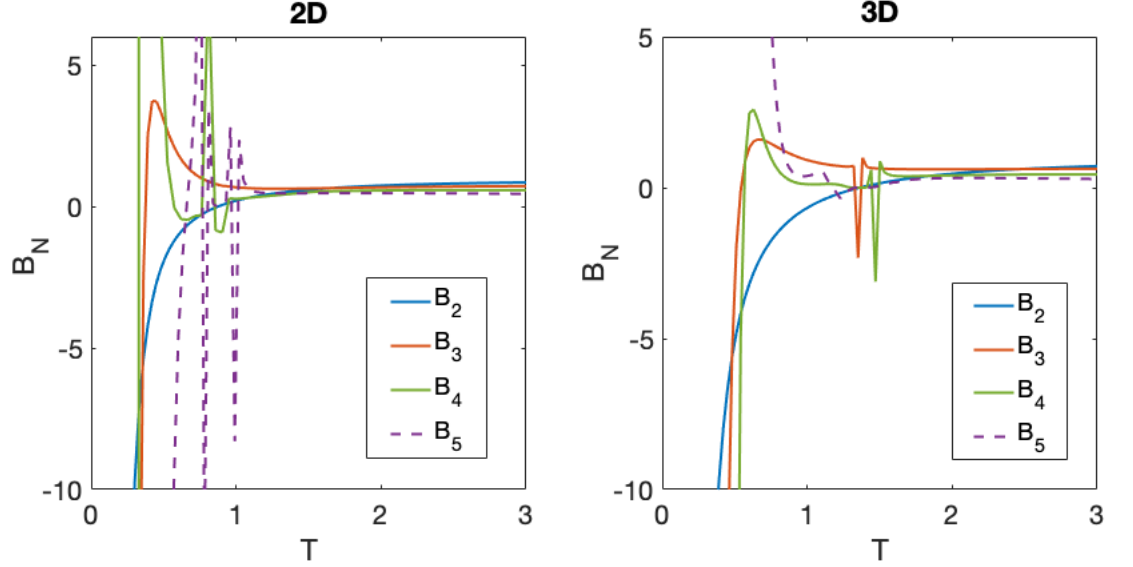
Figure 3.13: Virial coefficients for 2 and 3 dimension m=4 potential.

	2D			3D		
	B_2	B_3	B_4	B_2	B_3	B_4
a_0	0.8823	0.2465	-1.04	0.8938	0.1773	-1.262
a_1	0.2756	5.653	26.77	0.02662	5.075	27.07
a_2	-1.272	-24.73	-184.5	-1.921	-21.94	-178.5
a_3	0.4344	52.63	668.2	0.4457	47.76	610.2
a_4	-0.1101	-62.9	-1391	-0.09201	-58.85	-1170
a_5		43.98	1755	-0.01463	41.12	1294
a_6		-17.63	-1387		-11.9	-820.7
a_7		3.789	691.6		-3.107	278
a_8		-0.3443	-211.7		3.491	-39.12
a_9			36.44		-1.017	
a_{10}			-2.7		0.1015	
SSE	0.02422	0.07886	1.379	0.07716	0.003575	0.9083
R^2	1	1	1	1	1	1
adjusted R^2	1	1	1	1	1	1
RMSE	0.009236	0.01681	0.07413	0.0164	0.003612	0.05757

Table 6: Inverse temperature fit coefficients for m=4 potential.

In both 2 and 3 dimensions B_2 yields a good inverse temperature fit, the same can be observed for B_3, despite it encountering the Boyle Temperature, which potentially

causes a disturbance, as the hit and miss MC algorithm calculates the ratio B_N/B_2. The Boyle temperature is the temperature at which the second virial coefficient becomes zero. However, this can be ignored (note that for 2D, points disturbed by the Boyle temperature have been removed) when performing the inverse temperature fit. B_4 in 2D has a very steep peak (≈ 200) making a good fit difficult, which is reflected in its SSE value. In 3D B_4 is only disturbed by the Boyle temperature, but it is sufficiently far away from the peak to still yield a good fit. In both dimensions, B_5 is encountering the Boyle temperature in the critical area of the peak, making a fit impossible.

The virial results for 2D and 3D for the five virial coefficients for the mn-potential with $m = 5$, are displayed against temperature in figure 3.14 and their respective inverse temperature fits in table 7.
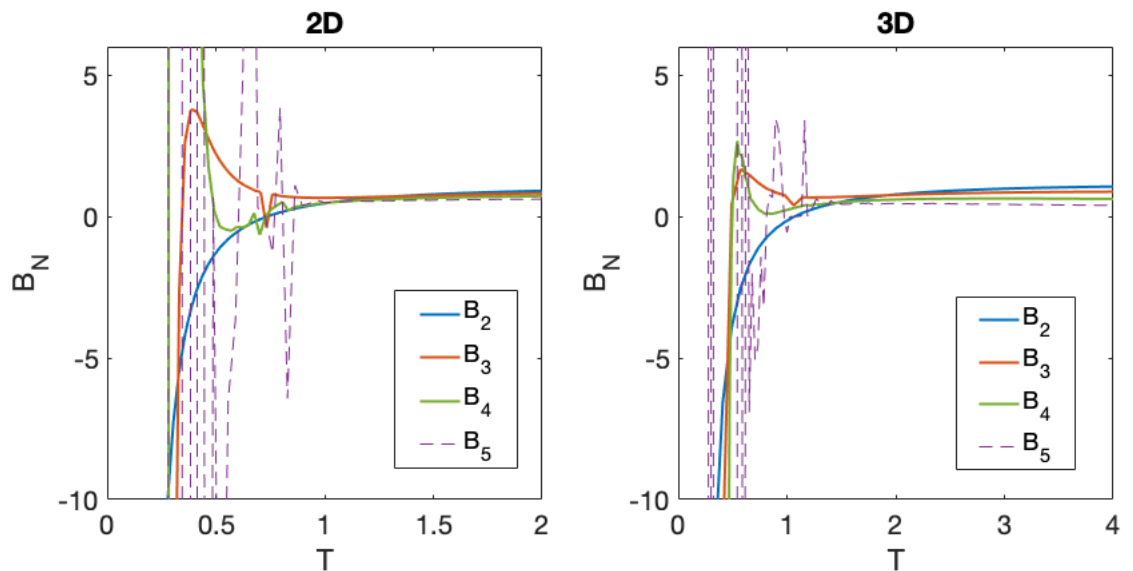
Figure 3.14: Virial dependence on temperature for m=5 potential.

For both dimensions B_2 yields a good inverse temperature fit. The effect of the Boyle temperature in B_3 is sufficiently far away from the peak not to disturb the fit and good fits in both dimensions are obtained. In the same way as was seen for $m = 4$, in 2D the peak in B_4 is very steep and difficult to fit. B_4 in 3D in has a narrow peak which negatively affects the fitting, although it isn't as steep as in 2D. B_5 is unable to be fitted in both dimensions as was seen for $m = 4$, although this seems not just to be due to an unfortunate position of the Boyle temperature but

	2D			3D		
	B_2	B_3	B_4	B_2	B_3	B_4
a_0	1.01	2.144	-210.4	1.149	1.894	1.847
a_1	0.3301	-10.35	2421	0.03068	-10.1	-12.41
a_2	-1.231	33.17	-1.128e+04	-1.778	40.21	34.44
a_3	0.4579	-54.18	2.815e+04	0.6163	-84.15	51.48
a_4	-0.1056	47.28	-4.196e+04	-0.1718	95.84	-497.5
a_5		-22.4	3.937e+04		-60.99	1219
a_6		5.519	-2.376e+04		21.56	-1568
a_7		-0.557	9185		-3.819	1182
a_8			-2194		0.2304	-524.4
a_9			294.7			127
a_{10}			-17			-13
SSE	0.05002	0.1758	358.6	0.006004	0.07908	0.302
R^2	1	1	1	1	1	0.9999
adjusted R^2	1	1	1	1	1	0.9999
RMSE	0.01911	0.03664	1.642	0.01196	0.04623	0.04877

Table 7: Inverse temperature fit coefficients for m=5 potential.

also due to noise.

The virial results for 2D and 3D for the five virial coefficients for the mn-potential with $m = 6$, are displayed against temperature in figure 3.15 and their respective inverse temperature fits in table 8.
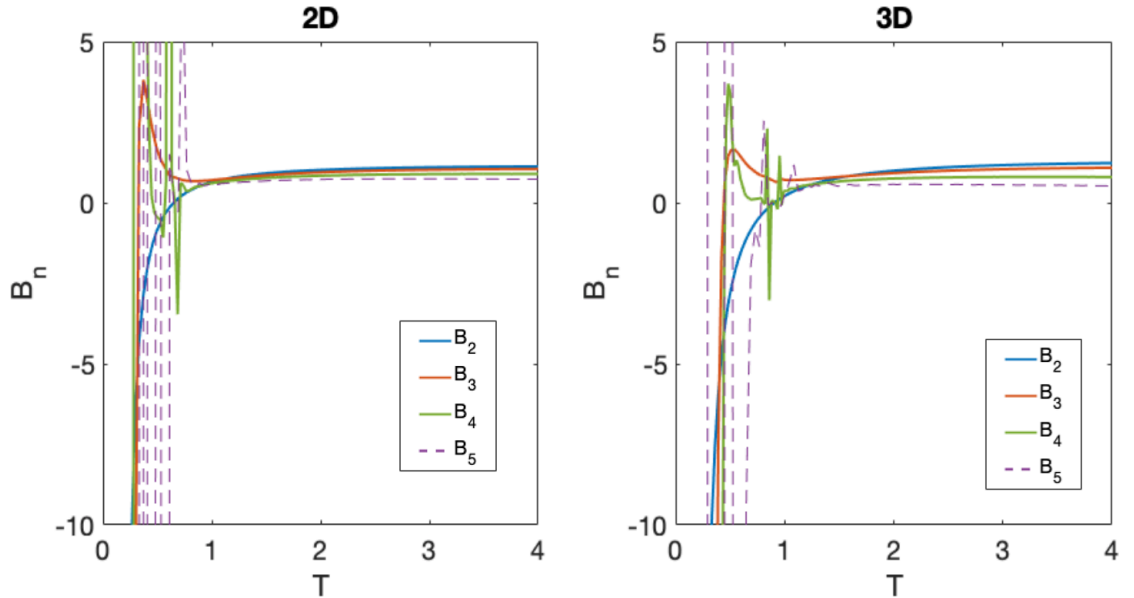
Figure 3.15: Virial temperature dependence for the potential $m = 6$.

For both dimensions B_2 yields a good inverse temperature fit as well as B_3 despite the presence of the Boyle temperature. B_4 in 2D has a very steep peak making fitting

	2D			3D		
	B_2	B_3	B_4	B_2	B_3	B_4
a_0	1.076	0.3743	-2.612	1.281	0.8146	0.7755
a_1	0.4202	6.832	47.54	0.1592	3.62	-7.441
a_2	-1.227	-25.73	-263	-1.683	-16.12	27.55
a_3	0.4687	46.59	783.2	0.6008	31.72	-51.32
a_4	-0.09999	-48.27	-1399	-0.1551	-37.19	52.6
a_5		29.61	1572		27.04	-30.31
a_6		-10.55	-1132		-11.68	-30.31
a_7		2.036	519.6		2.777	9.184
a_8		-0.166	-146.3		-0.2899	-1.201
a_9			22.95			
a_{10}			-1.531			
SSE	0.05261	0.01115	25.02	0.04992	0.01289	0.02786
R^2	0.9999	1	0.9999	1	1	1
adjusted R^2	0.9999	1	0.9999	1	1	1
RMSE	0.02418	0.01152	0.4387	0.01317	0.006785	0.01255

Table 8: Inverse temperature fit coefficients for m=6 potential.

difficult, which is clearly seen by the high SSE value of 25.02. B_4 in 3D managed a reasonable fit despite the presence of the Boyle temperature and a narrow peak. B_5 in both dimensions also seem affected by the Boyle temperate and noise.

3.4.2 Virial coefficients for the LJ/s-family

The virial results for 2D and 3D for the five virial coefficients for the LJ/s potential with $r_c = 1.4142$, are displayed against temperature in figure 3.16 and their respective inverse temperature fits in table 9.
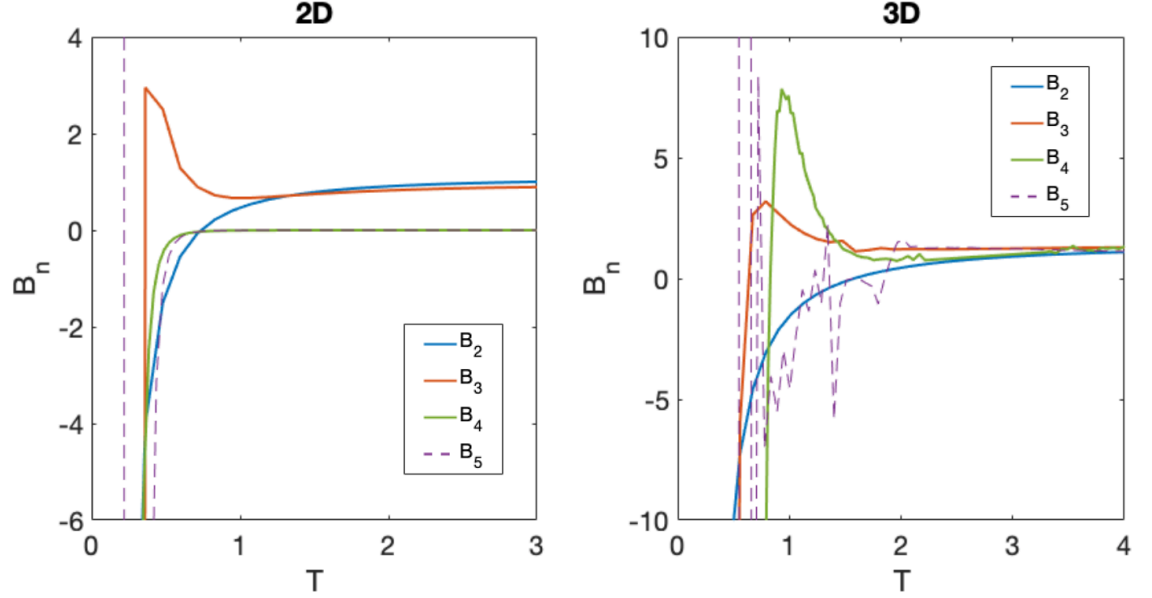
Figure 3.16: Virial dependence on temperature for the LJ/s potential with $r_c = 1.4142$.

	2D			3D		
	B_2	B_3	B_4	B_2	B_3	B_4
a_0	-0.04697	0.1904	-0.6658	0.5485	10.54	-64.64
a_1	-0.03921	-1.426	6.278	2.091	-62.85	1057
a_2	-0.3227	3.841	-22.83	-5.739	176.8	-7252
a_3	0.09733	-4.896	42.03	2.044	-274.6	2.803e+04
a_4	-0.01929	3.27	-43.33	-0.48	256	-6.761e+04
a_5		-1.179	26		-140.5	1.065e+05
a_6		0.2176	-9.017		42.89	-1.112e+05
a_7		-0.01648	1.679		-5.977	7.621e+04
a_8			-0.1315			8149
a_9						-878.8
a_{10}						
SSE	0.02018	0.01522	0.0341	0.4106	0.137	0.9951
R^2	0.9999	1	1	1	1	0.9998
adjusted R^2	0.9999	1	1	1	1	0.9998
RMSE	0.01205	0.01062	0.01446	0.05686	0.03629	0.09782

Table 9: Inverse temperature fit coefficients for $r_c = 1.4142$ potential.

For both dimensions, B_2 again yields a good inverse temperature fit and the

same is true for B_3. B_4 in 2D has lost its peak, which is unusual when compared to the B_4 results for the mn-family. Nothing in this study indicated that there was anything wrong with the calculation of the 2D B_4 for the $r_c = 1.4142$, but there is no obvious reason for the missing peak. B_4, in 3D, displays a peak and it not being too narrow, resulted in a good fit. In 2D, B_5 seems affected by the Boyle temperature and in 3D it appears very noisy as well, making a good fit impossible.

The virial results for 2D and 3D for the five virial coefficients for the LJ/s potential with $r_c = 1.73$, are displayed against temperature in figure 3.17 and their respective inverse temperature fits in table 10.
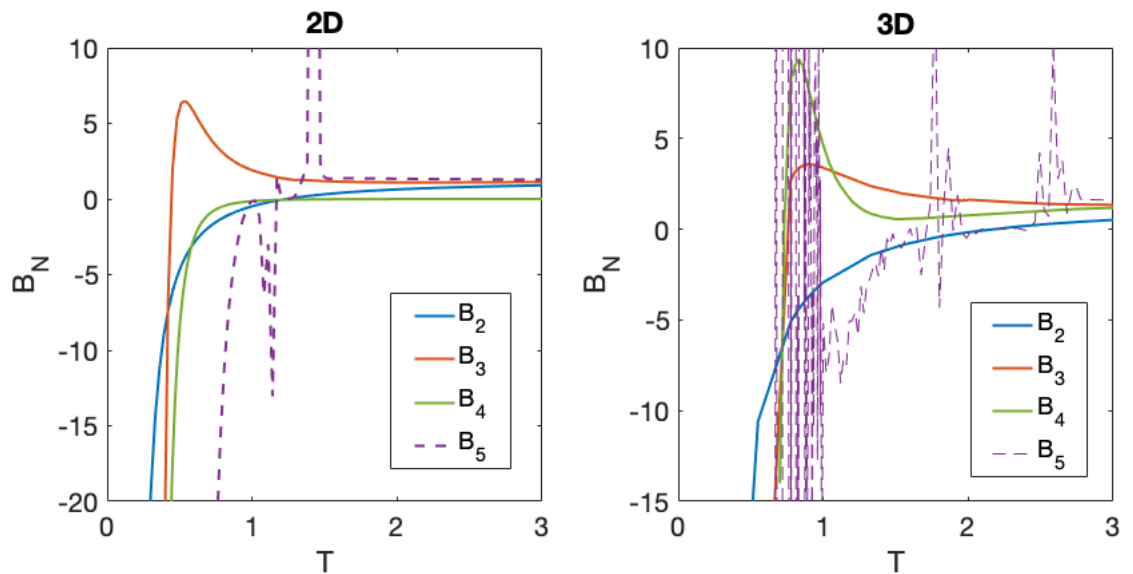
Figure 3.17: Virial temperature dependence for the LJ/s potential with $r_c = 1.73$

For both dimensions B_2 yields a good inverse temperature fit as does B_3 in both dimensions (note that the data points affected by the Boyle temperature have been omitted). B_4 in 2D, similarly to the case of the $r_c = 1.4142$, does not display a peak. In 3D B_4 has a very narrow peak which does affect its SSE value. B_5 is again affected by Boyle temperature and noise, making a fit impossible.

The virial results for 2D and 3D for the five virial coefficients for the LJ/s potential with $r_c = 1.73$, are displayed against temperature in figure 3.18 and their respective inverse temperature fits in table 11.

For both dimensions, B_2 yields a good inverse temperature fit and the same is the case for B_3 (note that, again, data points affected by the Boyle temperature

68

	2D			3D		
	B_2	B_3	B_4	B_2	B_3	B_4
a_0	1.257	0.8601	0.7754	1.429	1.299	0.9201
a_1	-0.8873	4.191	-7.44	-1.874	-0.771	-8.079
a_2	-0.5374	-19.05	27.54	-2.906	5.834	196.1
a_3	-0.4036	35.12	-51.32	0.7282	-15.04	-1510
a_4	0.1466	-30.42	52.6	-0.3097	22.54	6106
a_5	-0.03649	13.74	-30.3		-10.5	-1.494e+04
a_6		-2.513	9.184			2.306e+04
a_7			-1.201			-2.255e+04
a_8						1.354e+04
a_9						-4550
a_{10}						651.6
SSE	0.07354	0.1462	0.02786	0.006659	0.03478	2.579
R^2	1	0.9999	1	1	1	0.9971
adjusted R^2	1	0.9999	1	1	1	0.9967
RMSE	0.01598	0.02293	0.01255	0.009361	0.02168	0.1962

Table 10: Inverse temperature fit coefficients for $r_c = 1.73$ potential.
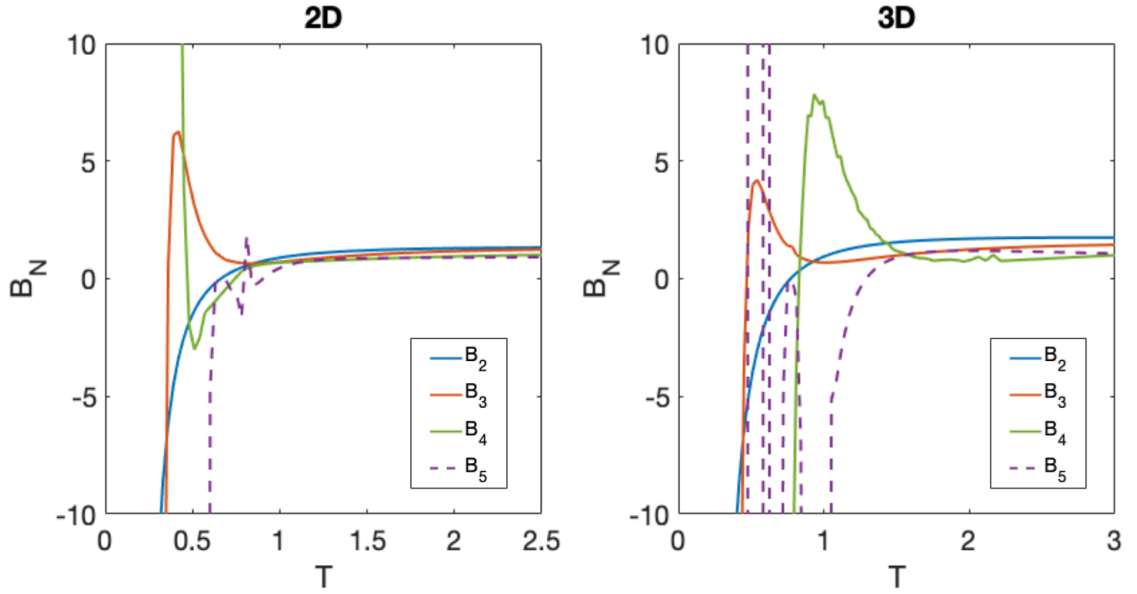
Figure 3.18: Virial temperature dependence for the LJ/s potential with $r_c = 2.2$.

has been omitted). B_4 in 3D results in a reasonable fit (data points affected by the Boyle temperature have been omitted), but B_4 in 2D is apparently affected by the Boyle temperature and a fit has not been attempted. As is the case with most of the virials, B_5 is too affected by Boyle temperature and noise to yield a fit.

As this study aims to make a comparison of the liquid-vapour coexistence and inversion curve, only B_3 is used, as it is the only coefficient that is consistent across

	2D		3D		
	B_2	B_3	B_2	B_3	B_4
a_0	1.191	0.8296	1.401	1.26	64.39
a_1	0.9831	5.644	2.112	0.946	-1493
a_2	-1.788	-25.22	-3.68	5.201	1.444×10^4
a_3	0.6663	55.21	1.708	-33.06	-7.615×10^4
a_4	-0.1771	-71.07	-0.6673	55.23	2.446×10^5
a_5		53.68	0.05721	-43.34	-5.046×10^5
a_6		-23.27		17.25	6.821×10^5
a_7		5.447		-2.786	-6.003×10^5
a_8		-0.5396			3.309×10^5
a_9					-1.037×10^5
a_{10}					1.408×10^4
SSE	0.0807	0.04181	0.01386	0.09791	6.034
R^2	1	1	1	1	0.999
adjusted R^2	1	1	1	1	0.9988
RMSE	0.01677	0.01222	0.006998	0.01873	0.3254

Table 11: Inverse temperature fit coefficients for $r_c = 2.2$ potential.

different families of potentials, members and dimensions. The choice of truncation of the virial EoS matters for the predicted thermodynamics, as is illustrated in figure 3.19 (the method of calculation is given in section 3.5). As can be seen, including the fourth virial coefficients lowers the entire liquid-vapour dome.
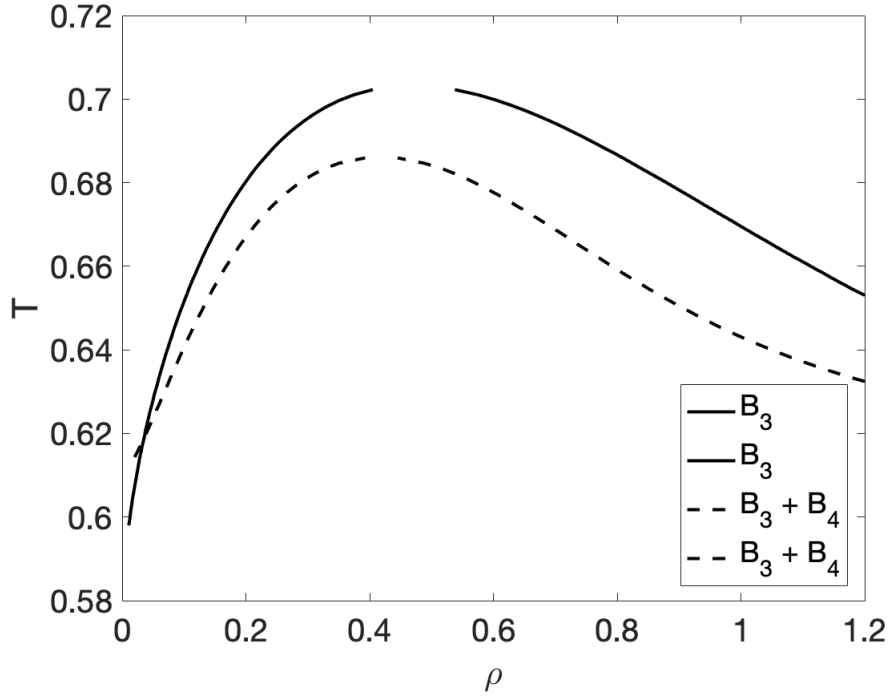
Figure 3.19: Liquid-vapour coexistence dome, predicted by virial coefficient theory for the m=4 pair potential, in 3D. Density and temperature is are in LJ reduced units.

3.5 Calculation of selected thermodynamic properties

Having obtained an equation of state, it is possible to derive thermodynamic properties, like the liquid-vapour coexistence dome and the Joule-Thomson inversion curve. This section provides the general derivation of these two thermodynamic quantities.

3.5.1 Liquid-vapour coexistence

The starting points for calculating liquid-vapour coexistence domes are the coexistence conditions and the truncated virial equation of state as a series expansion in density

$$\beta P = \rho + B_2\rho^2 + B_3\rho^3 + B_4\rho^4 + B_5\rho^5. \tag{3.63}$$

An expression for the chemical potential in terms of the truncated virial series is also required. The relation between chemical potential and pressure is given by

$$\beta\mu = \beta F + \beta P/\rho \tag{3.64}$$

where F is the full Helmholtz free energy $F = F_{ideal} + F_{excess}$, where the excess free energy is related to the virial EoS via the thermodynamic relation $(\partial F / \partial T)_{V,N} = -P$. The ideal and excess contribution to the free energy are given by

$$\beta F_{ideal} = \ln(\rho \Lambda^2) - 1 \qquad (3.65)$$

where Λ is the thermal de Broglige wavelength.

$$\beta F_{excess} = B_2 + \frac{1}{2}B_3\rho^2 + \frac{1}{3}B_4\rho^3 + \frac{1}{4}B_5\rho^4 \qquad (3.66)$$

Expressing the chemical potential μ in terms of virial coefficients, using the total free Helmholtz energy and the truncated virial EoS, results in

$$\beta\mu = 2B_2\rho + \frac{3}{2}B_3\rho^2 + \frac{3}{2}B_4\rho^3 + \frac{5}{4}B_5\rho^4 + \ln(\rho) + 2\ln(\Lambda) \qquad (3.67)$$

There exists several approaches to solve for coexistence. A graphical method involves plotting an isotherm on a chemical potential and pressure diagram, as displayed in figure 3.20. The point at which the isotherm crosses itself is the point where pressure and chemical potential for a single temperature are equal. Knowing the value of pressure and chemical potential, values for the high coexistence densities can be found, looking at the separate P, ρ and μ, ρ isotherms. Although the method is simple, it is tedious to implement.
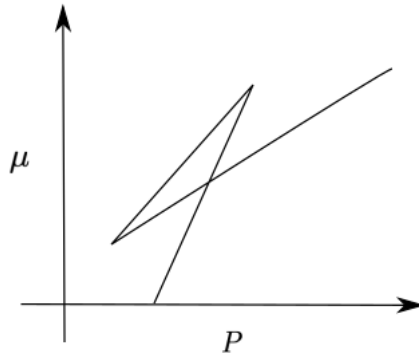
Figure 3.20: Isotherm on a μ,P diagram showing coexistence point where the line crosses itself. Where pressure P and chemical potential μ are both functions of density ρ.

It is also possible to solve the coexistence numerically, by solving the set of simultaneous equations.

$$P_{\text{gas}} = P_{\text{liquid}} \tag{3.68a}$$

$$\mu_{\text{gas}} = \mu_{\text{liquid}} \tag{3.68b}$$

Although equations (3.68a) and (3.68b) can be solved by existing software, such as MatLab, they are non linear, which makes the success of solving dependent on an initial good guess of the solution. Another method is the Maxwell equal area construction of equal area, which is described in section 1.2.3, which is the method used in this study.

3.5.2 The Joule-Thomson Inversion curve

The Joule-Thomson inversion curve is the value at which the Joule-Thomson coefficient vanishes. The process is performed under constant enthalpy, which can be described as a function of pressure P and temperature T.

$$H = f(P, T) \tag{3.69}$$

A change in enthalpy is given by

$$\partial H = \left(\frac{\partial H}{\partial P} \right)_T \partial P + \left(\frac{\partial H}{\partial T} \right)_P \partial T \tag{3.70}$$

using the second law of thermodynamics $\partial H = T\partial S + V\partial P$, equation (3.70) can be written as

$$\left(\frac{\partial H}{\partial P} \right)_T = T \left(\frac{\partial S}{\partial P} \right)_T + V \tag{3.71}$$

Utilising the Maxwell relationship

$$\left(\frac{\partial S}{\partial P} \right)_T = - \left(\frac{\partial V}{\partial T} \right)_P \tag{3.72}$$

equation (3.71) then becomes

$$\left(\frac{\partial H}{\partial P}\right)_T = -T\left(\frac{\partial V}{\partial T}\right)_P + V \tag{3.73}$$

In an isenthalpic process the enthalpy is constant $\partial H = 0$, therefore the Joule-Thomson coefficient can be written as

$$\mu_{JT} = \left(\frac{\partial T}{\partial P}\right)_H = \frac{-\left(\frac{\partial H}{\partial P}\right)_T}{\left(\frac{\partial H}{\partial T}\right)_P}$$
$$= \frac{1}{c_p}\left[T\left(\frac{\partial V}{\partial T}\right)_P - V\right] \tag{3.74}$$
$$= \frac{V}{c_p}(\alpha T - 1)$$

using the expression for μ_{JT} as given in [105], where the coefficient of thermal expansion is $\alpha = \frac{1}{V}(\partial V/\partial T)_P$ and c_P is the heat capacity of constant pressure. It is the case that

$$\left(\frac{\partial V}{\partial T}\right)_P = -\left(\frac{\partial P}{\partial T}\right)_V \times \left(\frac{\partial P}{\partial V}\right)_T^{-1} \tag{3.75}$$

employing the condition that μ_{JT} must be zero, the condition for a Joule-Thomson inversion curve must satisfy (let $V = 1/\rho$)

$$T\left(\frac{\partial P}{\partial T}\right)_\rho - \rho\left(\frac{\partial P}{\partial \rho}\right)_T = 0 \tag{3.76}$$

where the partial differentials of pressure are given by

$$T\left(\frac{\partial P}{\partial T}\right)_\rho = k_B T(\rho + \rho^2 B_2 + \rho^3 B_3 + \rho^4 B_4 + \rho^5 B_5) + k_B T^2(\rho^2 B_2' + \rho^3 B_3' + \rho^4 B_4' + \rho^5 B_5') \tag{3.77}$$

and

$$\rho\left(\frac{\partial P}{\partial \rho}\right)_T = k_B T\left(\rho + 2\rho^2 B_2 + 3\rho^3 B_3 + 4\rho^4 B_4 + 5\rho^5 B_5\right) \tag{3.78}$$

where $B_n' = \partial B_n/\partial T$. This gives the Joule-Thomson inversion curve condition in terms of virial coefficients expressed as a polynomial in ρ.

$$(TB_2' - B_2) + \rho(TB_3' - 2B_3) + \rho^2(TB_4' - 3B_4) + \rho^3(TB_5' - 4B_5) = 0 \tag{3.79}$$

Conventionally an inversion curve will be expressed as a (T,P) curve, the above yields a (T,ρ) curve. This is simple to change by using the virial equation of state, to obtain pressures corresponding to the calculated densities.

3.5.3 Comparison of liquid-vapour domes and inversion curves

In this section, results for the liquid-vapour coexistence and JT inverson curves are presented for the different potentials and dimensions.

For the 3D *mn*-family of potentials, the liquid-vapour coexistence dome and JT inversion curve are presented in figure 3.21. The binodals show a clear trend of decreasing the estimated critical temperature T_c, as the potential well in the members of the family narrows. The widest well, $m = 4$ and $n = 8$, shows the largest estimated $T_c \approx 0.67$. Decreasing the well width for the potential with $m = 5$ and $n = 10$, the critical density decreases to an estimation of $T_c \approx 0.58$. The narrowest well, when $m = 6$ and $n = 12$, shows the lowest estimated critical temperature at $T_c \approx 0.54$. Despite the significant decrease in critical temperature, the estimated critical density remains approximately the same, varying across the range of only $\rho = [0.4; 0.48]$

Unlike the binodals, the inversion curves do not show a clear trend with varying width of the potential well. There is a little indication that the width of the inversion curves becomes narrower as the width of the well decreases. The width being the range the range of temperature an inversion curve covers. This is obvious for $m = 4$ and $n = 8$, but the two other potentials seem very similar. It is difficult to quantify this as they exist for such different values of pressure. The estimated maxima in temperature T_{max} does not vary much in temperature between the potentials. It only varies within a range of $T_{max} = [0.95; 1.25]$. The two narrower potentials are more alike than the widest, $m = 4$ and $n = 8$. The maxima vary in their associated value for the pressure, $P_{max} = [2.1; 3.4]$. Again the narrowest potentials are more alike.
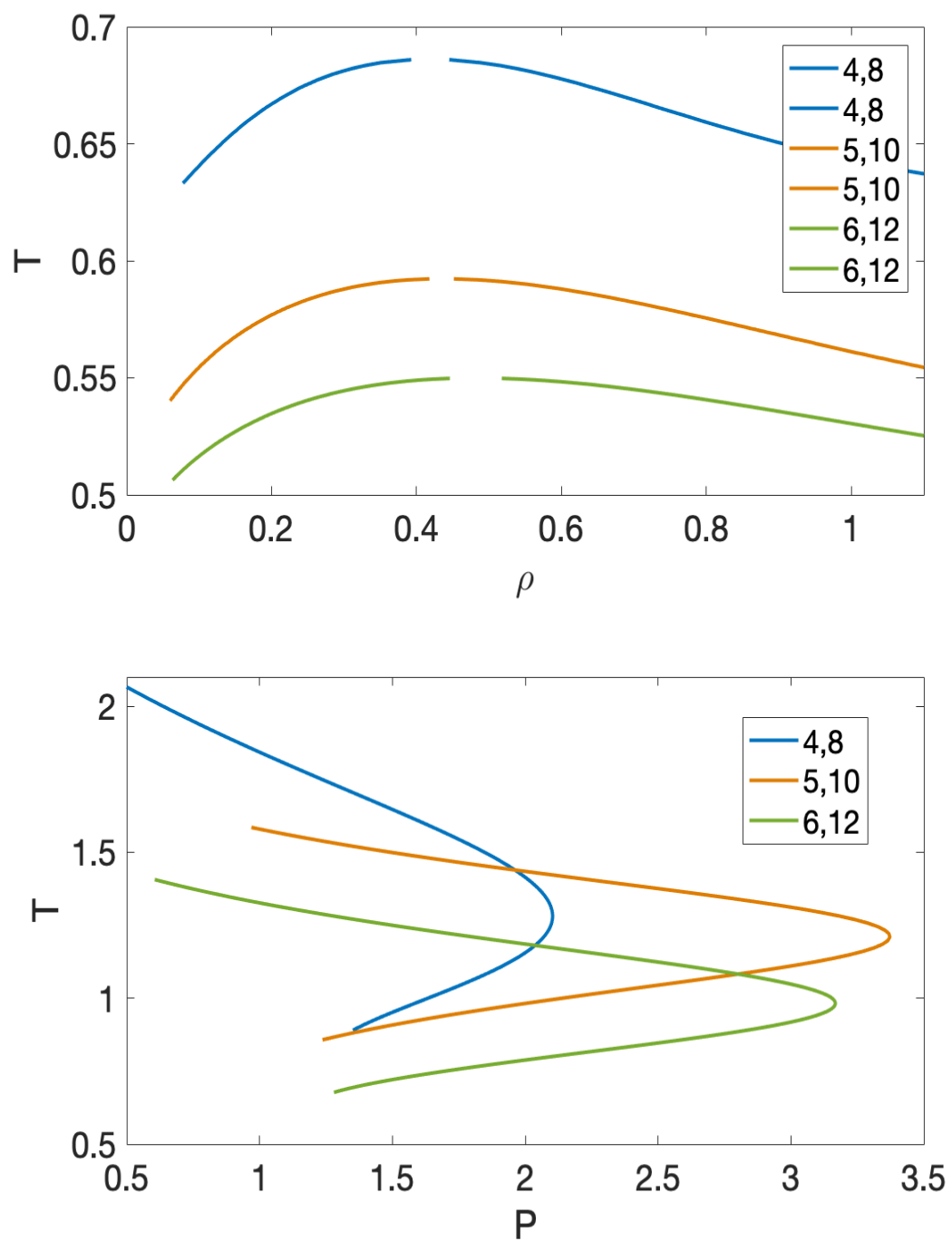
Figure 3.21: Binodals (top) and inversion curves (bottom) for the 3D m,n selected members. Pressure and Temperature are given in LJ reduced units.

For the 3D LJ/s family of potentials, the liquid-vapour coexistence dome and JT inversion curve are presented in figure 3.22. The binodal shows the same trend of decreasing the predicted critical temperature, when decreasing the range of the potential. For the longest range potential $r_c = 2.2$, the critical temperature is estimated to be $T_c \approx 1.1$, for $r_c = 1.7$ predicts $T_c \approx 0.98$ and for $r_c \approx 1.4$ the prediction is $T_c \approx 0.8$. As was seen for the 3D mn-family, the critical density remains the same at an estimated value of $\rho_c = 0.3$.

The inversion curves for the 3D LJ/s members show a similar trend to those of the 3D mn-family members. There is an indication that they narrow as the range of the potential shortens, however it is likewise difficult to quantify. The two narrowest potentials have an estimated maxima more alike, both with a $T_{max} \approx 1.9$, while the $r_c = 2.2$ has an estimated maximum temperature at $T_{max} = 3.5$.
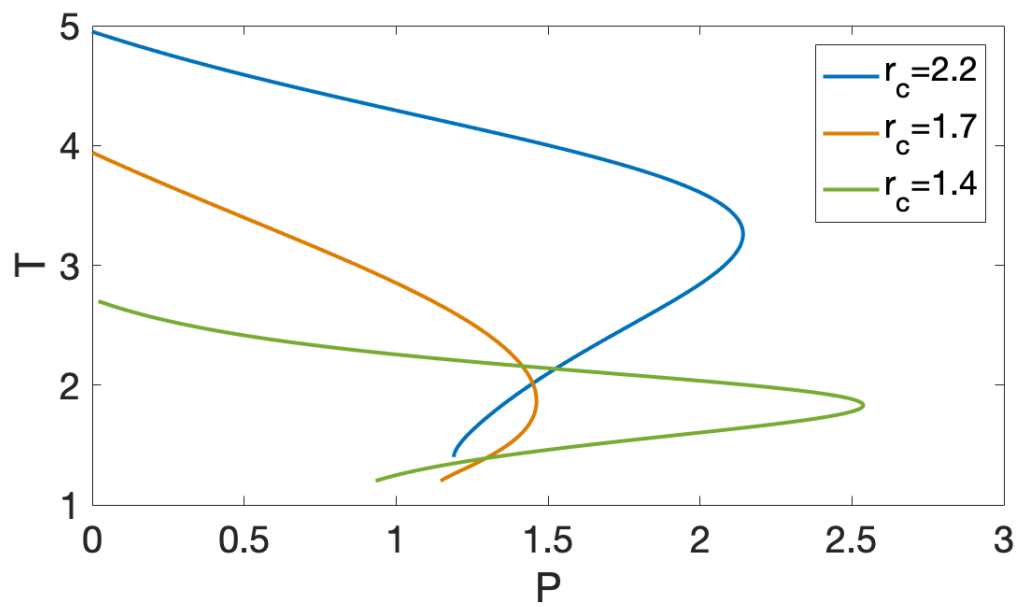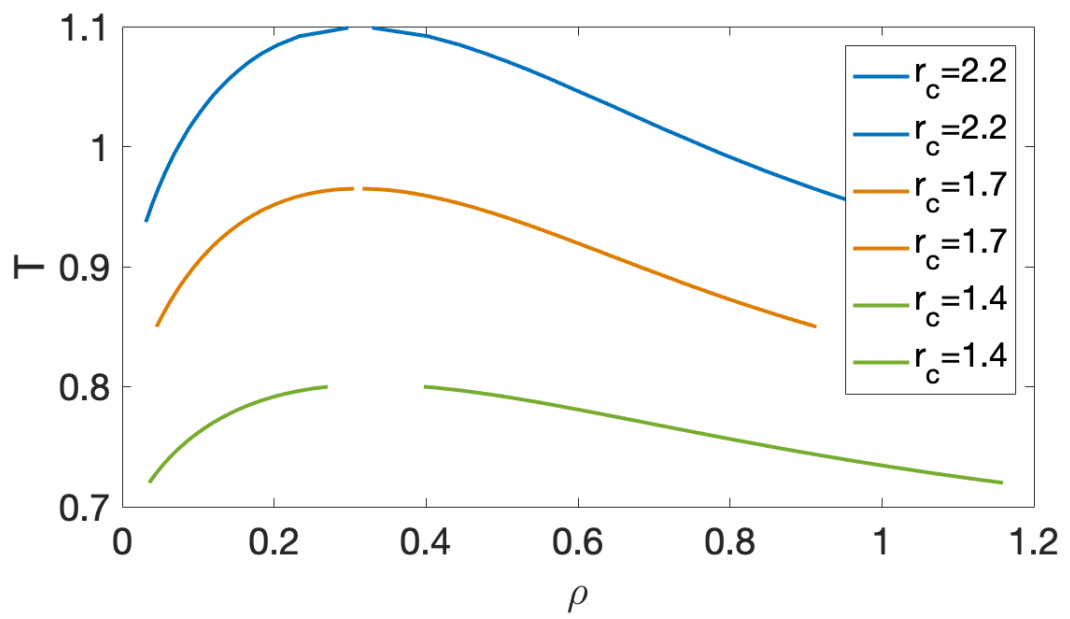
Figure 3.22: 3D LJ/s binodal and inversion curves. Pressure and Temperature are given in LJ reduced units.

For the 2D *mn*-family of potentials, the liquid-vapour coexistence dome and JT inversion curve are presented in figure 3.23. The same trend in decreasing T_c is observed, going from the highest at $T_c \approx 0.42$, decreasing to $T_c \approx 0.38$ and the lowest value $T_c \approx 0.335$. The critical density only varies in a small region $\rho_c = [0.25; 0.3]$. For the inversion curves the estimated maxima are in the range of $T_{max} = [0.75; 1.0]$ and there is less variation in pressure than was observed for the other potentials $P_{max} = [1; 1.2]$.
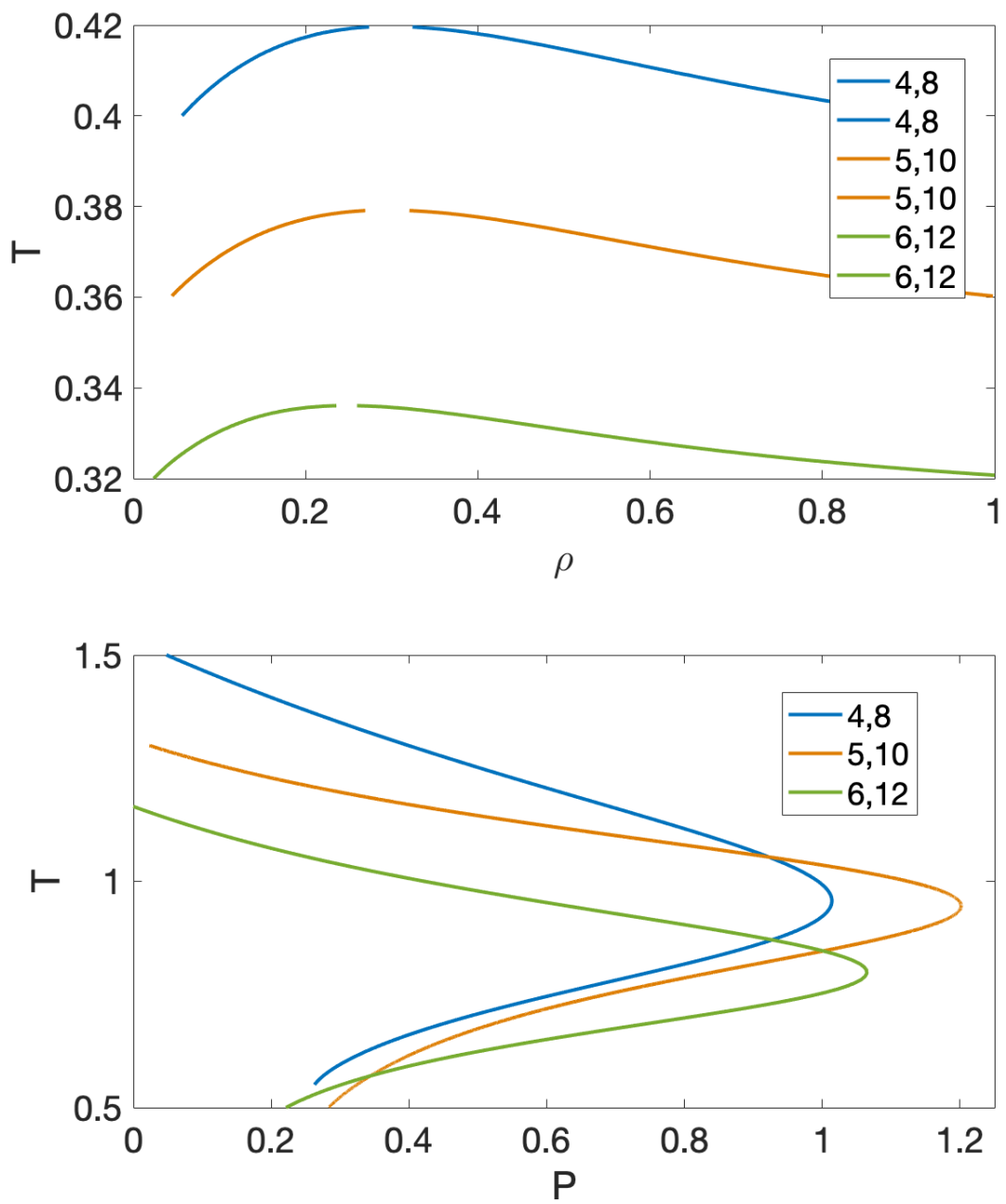
Figure 3.23: 2D mn binodal and inversion curves. Pressure and Temperature are given in LJ reduced units.

It was not possible to obtain physically meaningful results for the 2D LJ/s system. A discussion of this is given in section 3.6

3.6 Conclusions

The calculation of individual virials had great success for B_2 for all of the potentials in both dimensions, as would be expected. The same can be said for B_3, despite the presence of the Boyle temperature. Varying success was found in calculating B_4. For some, like the 3D mn-family a well defined peak was present and a good fit possible. In contrast, in the 2D mn-family, B_4 had a very steep peak, making the fit more difficult. B_4 for all of the LJ/s had a good fit, although in 2D the peak was not present. It is unlikely that there is a mistake in the MC hit and miss algorithm itself, considering the other results and the test that was performed in section 3.3. However there is currently no explanation of why it should deviate from the behaviour of other B_4. As these are the first results for these potentials' associated virials, it is clear that further investigation into the behaviour of these potentials, showing deviating behaviour, is needed.

No appropriate results were obtained for B_5, despite the use of Ree-Hoover diagrams, simulation time steps in the order of 10^{10} and closely spaced temperature values. Improvements to B_5 will require the use of better method than MC hit and miss, as it is too affected by noise and the Boyle temperature. In general, the understanding of the mathematical behaviour of virial coefficients is poor, especially for potentials differing from the more simple ones, like the HS and SW.

Despite the difficulties of calculating virial coefficients, a wide range of binodals and JT inversion curves was obtained. Generally the liquid-vapour domes showed an interesting trend in decreasing the predicted critical temperature, when shortening the range of the potential. The predicted 2D binodals were significantly smaller than 3D binodals, whilst keeping approximately the same predicted critical density. The maxima predicted for the inversion curves also showed a significant decrease from 3D to 2D.

The phase diagram for the 3D LJ/s with $r_c = 1.7$, shown in figure 3.24 (unpub-

lished, in private communication with Halfsjöld), which has been calculated by MD, shows that the virial results overestimate the critical temperature, but there is a good agreement for the critical density.
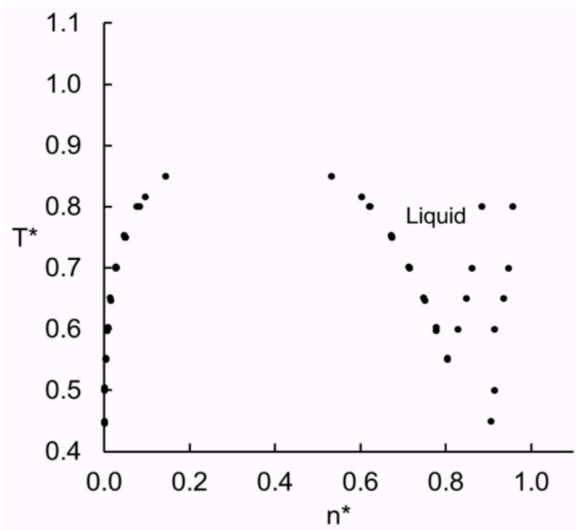
Figure 3.24: (unpublished in private communication with Halfsjöld) 3D LJ/s with $r_c = 1.71$. The axis are in LJ reduced units, where T^* is reduced temperature and n^* is reduced density.

It must also be said that, in general, the curvature of the virial predicted liquid branch in any family for any dimension, seems too shallow for what is expected and this does not change by adding on an extra virial term as was seen in figure 3.19. The liquid branch is generally observed to have the dome shape shown in figure 3.24.

In figure 3.25, the results of extensive constant enthalpy MD simulations, done in this study and described in detail in section 5, are shown, which compare the predicted inversion curve for the 2D $m = 4$ and $n = 8$ potential, using up to the third virial coefficient B_3. It is expected that the predicted inversion curve goes through the maxima of the isenthalps and there is good agreement at higher temperatures, but it starts to deviate after having reached its maxima. A puzzling feature is that it seems to agree well on the maxima pressure.

It is possible that different fits from the inverse temperature fit could be used to improve the obtained results. There has also been considerable success in using Padé approximations to better predict higher order virials [106]. Having said that, only the use of B_3 has yielded an estimated critical density which agrees well
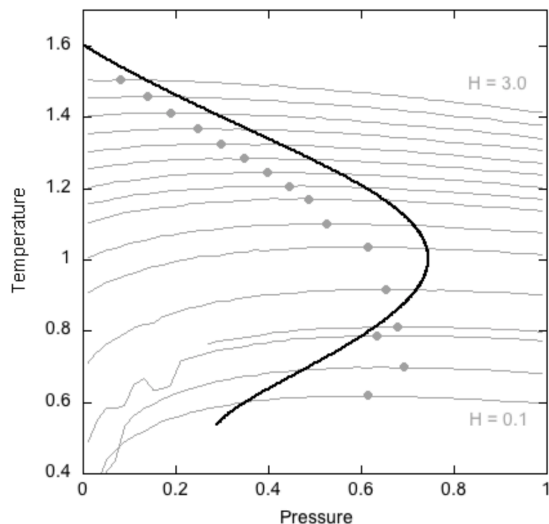
Figure 3.25: Constant enthalpy MD simulations done in this study (solid grey lines), comparing their maxima (grey circles) with the estimated JT inversion curve (solid black line) for the 2D $n = 8$ $m = 4$ potential, using up to the third virial coefficient, B_3.

with simulations. The usefulness of the lower order virials has been noted before, Lekkerkerker and Vliegenthart used only B_2 to estimate the critical point [107].

Virial coefficient theory has yielded some useful results, but the individual calculation of virials is laborious and the virial series in itself does not seem to converge well for the investigated systems. This study will now turn to perturbation theory, for which pre calculations of unpredictable virials are not necessary.

4 Calculation of thermodynamic properties using Perturbation Theory

Johannes van der Waals introduced the idea that the repulsive and attractive intermolecular forces make essentially independent contributions to the thermodynamics and can thus be treated separately. The strong, short ranged repulsive force is responsible for the structural arrangement of the molecules whereas the energy associated with long range attraction can be treated as a perturbation. This leads to the Barker-Henderson (BH) perturbation theory, followed by other versions of soft core perturbations, which have been outlined in section 1.2. Barker and Henderson studied the LJ system, splitting the potential at the distance r where it becomes zero $\phi_{LJ}(r) = 0$. The strong but short ranged potential was represented by the HS system while the longer attractive part was represented by the Zwanzig high-temperature perturbation [108, 109].

The BH perturbation theory has been shown to agree well with experimental results. However, because the long range perturbation also includes some of the repulsive part, it makes the second order perturbation term tricky to deal with. One solution is to split the potential at the minima, as was done by Weeks-Chandler-Andersen (WCA), so that no repulsive contribution appears in the long range energy perturbation. It includes a shift in the potential which means less variation of the radial distribution function, resulting in a faster converging series. Although they use an optimised cluster expansion instead of the Zwanzig high-temperature perturbation, the first correction is identical to that of BH. The WCA theory is however limited at critical temperatures, because the HS system is likely to be lying in the liquid-solid metastable region at high densities [32]. It therefore does not perform well in the critical region.

In this section a Barker-Henderson second order perturbation theory, using the reference system of the HS, is applied to each of the selected potentials, to obtain liquid-vapour coexistence and JT inversion curves.

Few authors have employed BH perturbation theory in 2D, mainly due to a lack

of interest in 2D systems, but also due to a lack of an analytical EoS for hard disks and lack of an analytical radial distribution function for disks. In this section we use a recently proposed analytical expression for the 2D structure factor, inverting it to obtain the radial distribution function and hence obtain a workable 2D perturbation theory which we can apply to our potentials of interest obtaining JT inversion curves and liquid-vapour binodals.

4.1 3D Perturbation Theory

This section will follow the version of BH perturbation theory, outlined by Levesque and Verlet [110]. Levesque and Verlet introduced a strength parameter λ, which multiplies the attractive part of the potential. The Helmholtz free energy is then written as

$$F/Nk_BT = F_0/Nk_BT + \int_0^1 \langle W \rangle_\lambda /Nk_BT \mathrm{d}\lambda \qquad (4.1)$$

F_0 is the free energy of the reference system and $\langle W \rangle_\lambda$ the average of the long range interaction at a specific value of λ. When the long range interaction $w(r)$, is given by

$$\sum_{i<j} w(|\mathbf{r}_i - \mathbf{r}_j|) \qquad (4.2)$$

the average of the long range interaction can be expressed in terms of the radial distribution function $g_0(r, \lambda)$

$$\langle W \rangle_\lambda /Nk_BT = \frac{1}{2}\rho\beta \int g_0(r, \lambda)w(r)\mathrm{d}\mathbf{r} \qquad (4.3)$$

where $\beta = 1/k_BT$

4.1.1 Reference system

A reference system must be chosen in such a way that the Helmholtz free energy is known exactly. Barker and Henderson chose the HS system, as they found this was a reasonable approximation to the reference state $u(r)$, shown in figure 4.1, when perturbing the LJ system. In general the free energy calculation of the reference
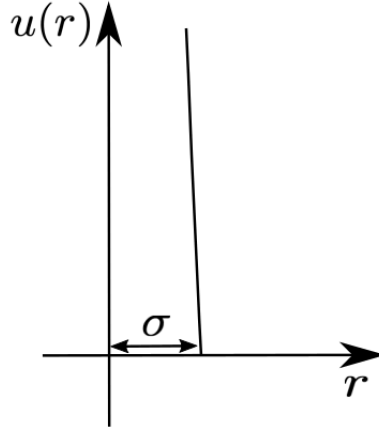
Figure 4.1: The short range strong repulsive contribution to the potential, u(r). According to the Barker-Henderson split.

system is given by

$$F_0/Nk_BT = \int_0^\rho (\text{P}/\rho k_BT - 1)\mathrm{d}\rho/\rho \tag{4.4}$$

where P is the compressibility factor of the HS system (Levesque and Verlet used a virial equation of state to calculate this). For HS, the Carnahan-Starling EoS is widely accepted as being the most accurate [111]. Using the hard sphere packing fraction $\eta = 1/2 \times \pi\rho d$, it is given as

$$Z = \frac{1 + \eta + \eta^2 - \eta^3}{(-\eta)^3} \tag{4.5}$$

where Z is the compressibility $(= PV/k_BT)$ and d is an effective or temperature dependent hard sphere diameter

$$d = \int_0^\sigma \mathrm{d}z \left(1 - e^{-\beta u(z)}\right) \tag{4.6}$$

Using the Carnahan-Starling EoS the excess free energy per particle becomes [112]

$$\frac{\beta F^{ex}}{N} = \frac{\eta(4 - 3\eta)}{(1 - \eta)^3}. \tag{4.7}$$

4.1.2 First order correction

The first order correction uses the perturbed potential $w(r)$, which is shown for a LJ system in figure 4.2. In general the first order correction to the free energy is
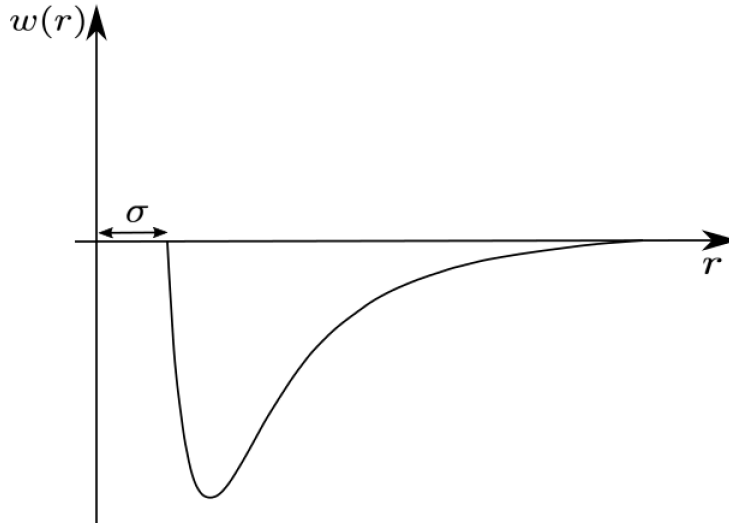
Figure 4.2: Long range interaction of the Barker-Henderson split.

given by the integral of the product $g_0(r)w(r)$.

$$\langle W \rangle_0 / N k_B T = \frac{1}{2} \rho \beta \int g_0(r) w(r) \mathrm{d}\mathbf{r} \tag{4.8}$$

Originally Barker-Henderson used the Percus-Yevick solution to the HS radial distribution function $g_0(r)$, but it was shown by Levesque and Verlet that this led to a small error in the first order correction and an even larger error in the second order correction [110]. Instead, this study makes use of the radial distribution function published by Trokhymchuk and Henderson [113]. The radial distribution function is divided into a short and long range interaction

$$g_0(r)^{short} = \begin{cases} 0 & r < \sigma \\ \frac{A}{r} e^{\mu[r-\sigma]} + \frac{B}{r}\cos(\beta[r-\sigma]+\gamma)e^{\alpha[r-\sigma]} & \sigma \leq r \leq r^* \end{cases} \tag{4.9}$$

and

$$g_0(r)^{long} = 1 + \frac{C}{r}\cos(wr + \delta)e^{-\kappa r}. \tag{4.10}$$

The coefficients $\omega\sigma$ and $\kappa\sigma$ were calculated by Roth *et al.* [113] to be

$$\omega\sigma = -0.682\exp(-24.697\eta) + 4.720 + 4.450\eta \tag{4.11a}$$

$$\kappa\sigma = 4.674\exp(-3.935\eta) + 3.536\exp(-56.270\eta) \tag{4.11b}$$

The coefficients $\alpha\sigma$, $\beta\sigma$, $r*/\sigma$ and g_m were obtained by Trokhymchuk & Henderson.

$$\alpha\sigma = 44.554 + 79.868\eta + 116.432\eta^2 - 44.652\exp(2\eta) \tag{4.12a}$$

$$\beta\sigma = -5.022 + 5.857\eta + 5.089\exp(-4\eta) \tag{4.12b}$$

$$r^*/\sigma = 2.0116 - 1.0647\eta + 0.0538\eta^2 \tag{4.12c}$$

$$g_m = 1.0286 - 0.6095\eta + 3.5781\eta^2 - 21.3651\eta^3 + 42.6344\eta^4 - 33.8485\eta^5 \tag{4.12d}$$

The parameters B, A, δ, C and g_σ^{expt} are defined as

$$B = \frac{g_m - (\sigma g_\sigma^{expt}/r^*)\exp(\mu[r^* - \sigma])}{\cos(\beta[r^* - \sigma] + \gamma)\exp\alpha[r^* - \sigma] - \cos\gamma\exp\mu[r^* - \sigma]} \tag{4.13a}$$

$$A = \sigma g_\sigma^{expt} - B\cos(\gamma) \tag{4.13b}$$

$$\delta = -\omega r^* - \arctan\left(\frac{\kappa r^* + 1}{\omega r^*}\right) \tag{4.13c}$$

$$C = \frac{r^*[g_m - 1]\exp(\kappa r^*)}{\cos(\omega r^* + \delta)} \tag{4.13d}$$

$$g_\sigma^{expt} = \frac{1}{4\eta}\left(\frac{1 + \eta + \eta^2 - (2/3)\eta^3 - (2/3)\eta^4}{(1 - \eta)^3}\right) \tag{4.13e}$$

The analytical expression by Trokhymchuk and Henderson, at three different densities, is compared to MC calculations in figure 4.3. They show a good agreement, despite a slight deviation at the first peak for $\rho = 0.9$. However, the same deviation is found in the work by Trokhymchuk and Henderson themselves.

4.1.3 Second order correction

The second order correction can be obtained by following either the macroscopic or the microscopic compressibility approximation. Following the work of Levesque and Verlet, this study uses the macroscopic compressibility approximation, which is
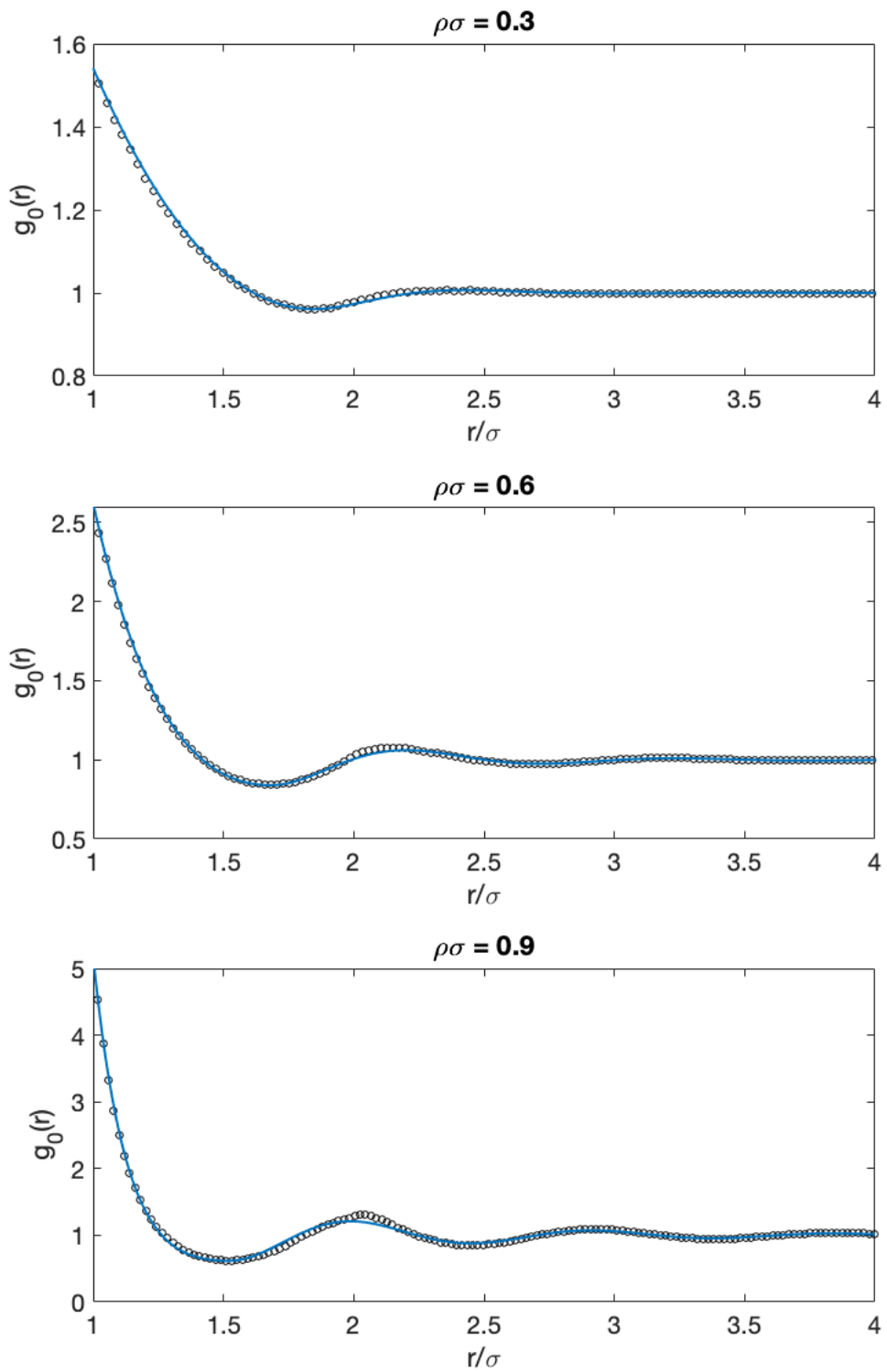
Figure 4.3: HS radial distribution functions at various densities $\rho = [0.3, 0.6, 0.9]$, calculated using the analytical $g_0(r)$ by Trokhymchuk and Henderson (solid line) compared to MC calculations (circles) which were performed in this study.

given by

$$\rho \int d\mathbf{r} \omega^2(r) g_0(r) / (\partial P / \partial \rho)_0 \qquad (4.14)$$

where $(\partial P / \partial \rho)_0$ is the isothermal HS compressibility. From the Carnahan-Starling EoS, this is given by

$$\left(\frac{\partial P}{\partial \rho} \right)_0 = \frac{1 + 4\eta^2 - 4\eta^3 + \eta^4}{1 - \eta^4}. \qquad (4.15)$$

Apart from the additional factor of the isothermal HS compressibility and an extra factor of the perturbed potential contribution, the second order correction is solved exactly like the first order correction.

4.1.4 Verification

A comparison was made with the values for the free energy of the LJ 12-6 potential, obtained by Levesque and Verlet. These are shown in table 12, along with values calculated in this study. A small difference is expected, as the Carnahan-Starling EoS offers greater accuracy in describing the behaviour of HS [114] than the virial EoS used by Levesque and Verlet.

ρ	$P/\rho kT$	L&V	difference(%)	F_0/NkT	L&V	difference(%)
0.2	1.49	1.48	0.7	0.429	0.430	0.2
0.5	2.88	2.89	0.3	1.335	1.343	0.6
0.8	6.12	6.07	0.8	2.806	2.814	0.3

Table 12: Comparison of free energy calculations of the HS system to those obtained by Levesque & Verlet (L&V) (1969) [110].

The full Helmholtz free energy to the first and second order correction is compared to results obtained by Cuadros et al. (1996) [115] who performed an extensive MD study on the LJ system. These are displayed in figure 4.4. It shows a significant improvement to the free energy when adding the second order correction and a reasonable agreement between the second order correction and MD results, until an increasing deviation after the minima.

Having verified the free energy calculations, it is useful to further check how well it predicts isotherms. An isotherm for the LJ system was chosen at a temperature
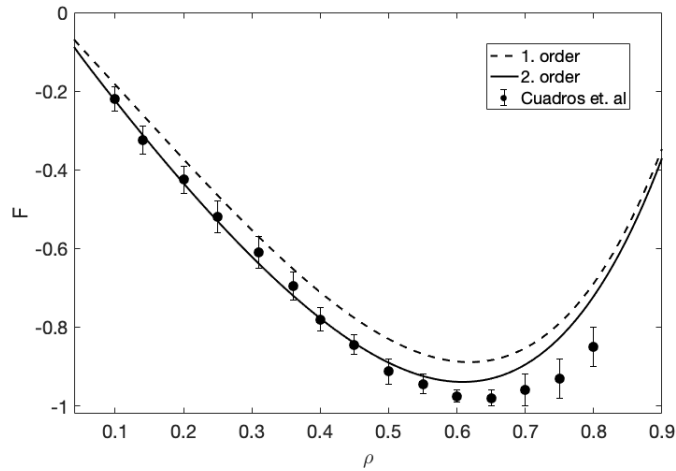
Figure 4.4: 1st order perturbation of the Helmholtz free energy is compared to the 2nd order pertubation and the extensive MD results obtained by Cuadros et al. (1996) [115], for the LJ system at temperature $T = 1.5$.

$T = 1.5$ above the critical temperature to avoid the liquid vapour phase transition. The results are shown in figure 4.5, where good agreement is observed, up until a small deviation at higher densities. A discussion of how pressure was obtained can be found in the next section.
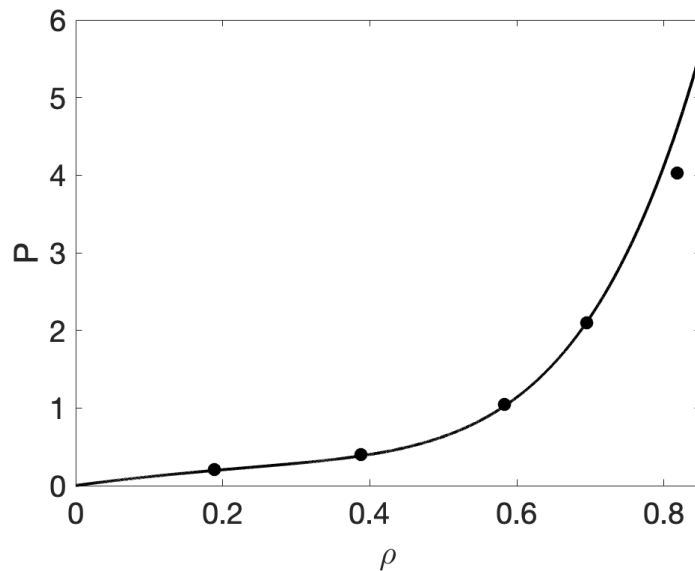
Figure 4.5: Isotherm at T = 1.5 for the LJ system (line), compared to individual NVT MD simulations, performed in this study.

4.1.5 Obtaining liquid-vapour coexistence and Joule-Thomson inversion curves.

BH perturbation theory gives a prescription for calculating the free energy of a system described by a pair potential. In this section we show how to make use of the free energy to obtain a binodal and JT inversion curve. The compression factor Z for the system follows directly from the derivative of the free energy

$$Z = Z_0 + \rho \frac{\partial}{\partial \rho} \left[\beta F - \beta F_0 \right] \tag{4.16}$$

where Z_0 is the HS compression factor. The pressure can be obtained using

$$\beta P = \rho Z. \tag{4.17}$$

Barker-Henderson perturbation theory does not yield good results in the low density region. To extend the density region, a virial equation of state truncated at the third virial coefficient was used. At the point at which the two regions meet, there is a slight discontinuity in the pressure. This was accommodated by smoothing the entire density-pressure region using an empirical virial series up to the fifth order in density, computing 10^3 densities.

$$P^{smooth} = a_1 \rho + a_2 \rho^2 + a_3 \rho^3 + a_4 \rho^4 + a_5 \rho^5 \tag{4.18}$$

The fitted equation was then used to generate a smooth chemical potential.

$$\beta \mu^{smooth} = \ln(\rho) + b_1 \rho + b_2 \rho^2 + b_3 \rho^3 + b_4 \rho^4 + b_5 \rho^5 \tag{4.19}$$

The differentiation in equation (4.16) was performed using MatLab's numerical differentiator, the *diff*-function. Along an isotherm, the corresponding points on the liquid-vapour binodal are obtained by solving the following simultaneous equations

$$P_{gas} = P_{liquid}$$

$$\mu_{gas} = \mu_{liquid}$$

(4.20)

These conditions were met using the Maxwell equal area construction.

Obtaining the JT inversion curve follows the same method used in virial coefficient theory in section 3.5.2, identifying the point at which the JT coefficient vanishes, given in equation (3.76). Isotherms were then generated and fitted using least squares to a virial type equation truncated at the mth order in density (m = 6 is appropriate for this work). Taking derivatives along an isotherm and an isochore, then substituting the resulting expression into equation (4.21)

$$\beta P = \rho + \sum_{k=2}^{m} na_{k-1}\rho^k = 0$$

(4.21)

yields a polynomial

$$\sum_{k=1}^{m} \rho^{k-1}[Ta'_k - ka_k] = 0.$$

(4.22)

The roots correspond to points on the ρ, T inversion curve. The derivatives a'_k were obtained by first fitting the empirical coefficients in equation (4.22) against inverse temperature using least squares.

$$a_k = \sum_{n=1}^{p} b_n \beta^{n-1} = 0$$

(4.23)

where $\beta = 1/k_B T$. For this work, $p = 5$ was shown to be sufficient. The derivatives follow from differentiation of equation (4.21) with respect to temperature, and have $m - 1$ roots. Discarding unsuitable roots (those being imaginary, unphysical roots showing negative densities and roots that clearly lie outside the fluid range) leaves only a single root for density at any given temperature in the coexistence region. As for the inversion curves obtained for virial coefficient theory, the density is converted to pressure by using the empirical equation of state, given in equation (4.17).

4.1.6 3D perturbation results.

In this section, binodals and inversion curves obtained by a 3D BH perturbation theory are presented for the selected members of the mn-family and LJ/s.

The binodals for both families are shown in figure 4.6. The predicted critical temperatures decreases as the range of the potential decrease. A summation of the estimates for the critical temperature T_c is given in table 13.

mn-family		LJ/s-family	
m,n	$T_c(\approx)$	r_c	$T_c(\approx)$
4,8	0.68	2.2	1.10
5,10	0.58	1.7	0.82
6,12	0.53	1.4	0.80

Table 13: Summary of the estimated ($\approx$) critical temperatures T_c for the mn-family (m,n) and the LJ/s (r_c).

The prediction of the critical density stays the same when varying the potential range. For the mn-family $\rho_c \approx 0.6$ and for the LJ/s $\rho_c \approx 0.3$.

For the inversion curves predicted by perturbation theory, displayed in figure 4.7, the maximum temperature decreases when the range of the potentials decreases. For the longest range of the mn-family $m = 4$ and $n = 8$, the predicted maximum temperature is $T_{max} = 1.4$, for $m = 5$ and $n = 10$ $T_{max} = 1.1$ and for the shortest $m = 6$ and $n = 12$ the maximum temperature is estimated to be $T_{max} = 0.75$. The range of pressure for each of the inversion curves is very similar, as well as their shape. Therefore it is possible to see clear indications that the inversion curves for both families becomes narrower as the range decreases. There is observed an odd 'bump' for the inversion curve for $r_c = 2.2$. It is not clear whether this is a physical feature, or an effect of perturbing at a long range.
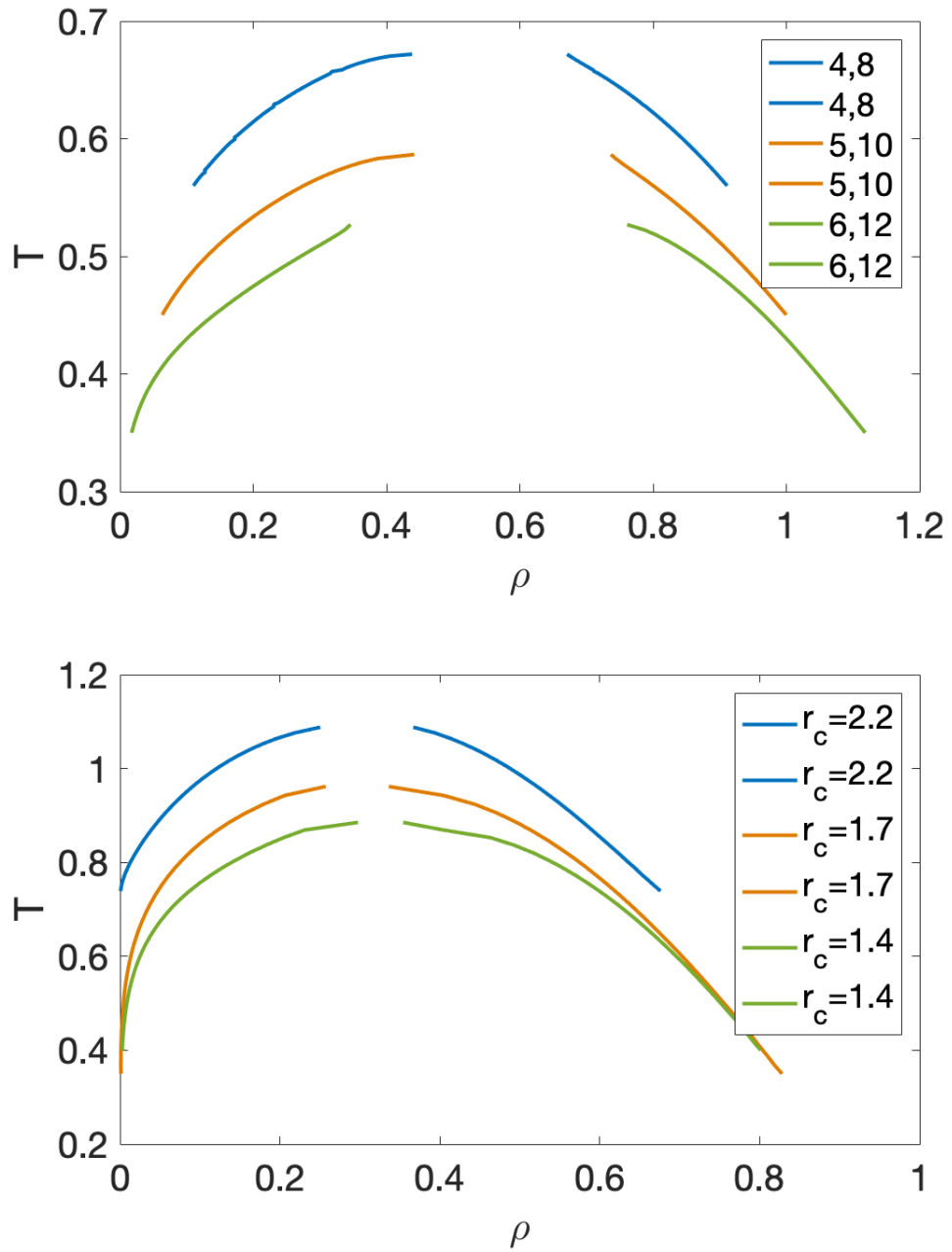
Figure 4.6: Binodals predicted by the 3D BH second order perturbation theory. Showing results for the *mn-* and LJ/s family-members. Using LJ reduced units.
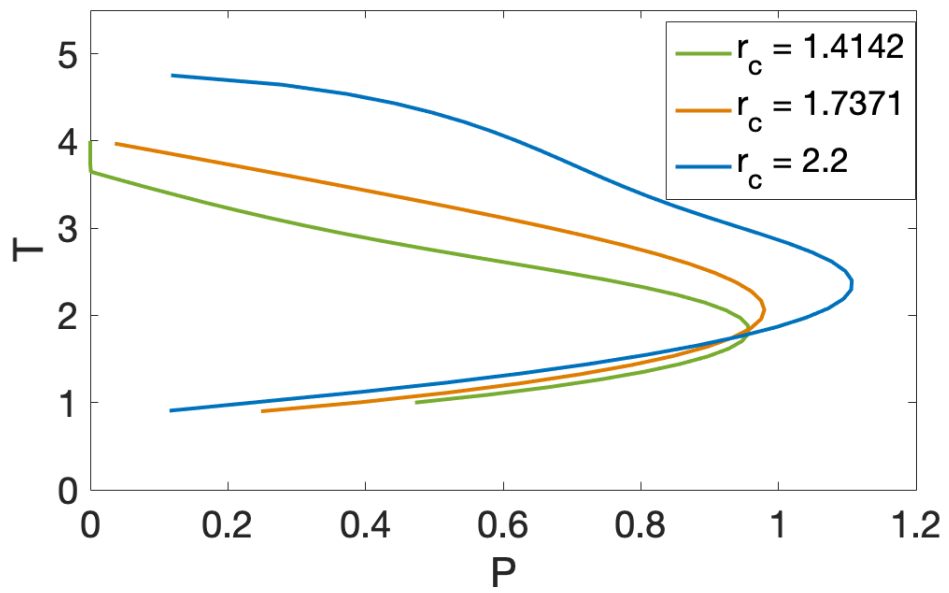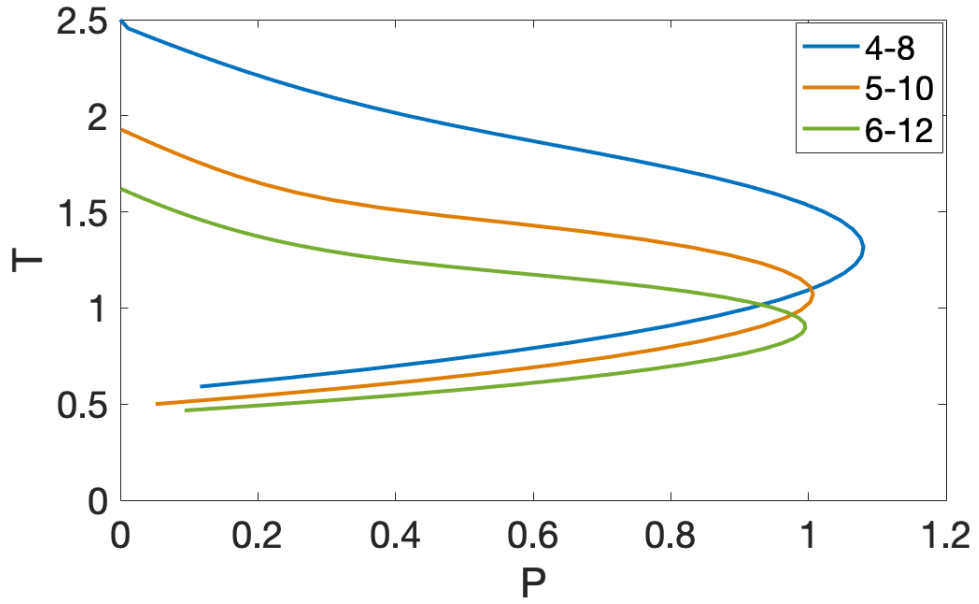
Figure 4.7: Inversion curve predicted by the 3D Barker-Henderson second order perturbation theory. Showing results for the *mn*- and LJ/s-family. Using LJ reduced units.

4.2   2D Perturbation Theory

Henderson extended the BH perturbation theory to two dimensions, in a study of the two dimensional LJ fluid [116]. He used HD distribution functions produced by MC simulation as currently there exists no analytical expression for the radial distribution function for the HD system. However, there exists an analytical expression for the HD correlation function $c(k)$, which is related to the static structure factor, which is further related to the radial distribution function. From this, a 2D BH perturbation of the Helmholtz free energy follows that of three dimensions.

4.2.1   Hard disk radial distribution function.

The relation between the correlation function $c(\kappa)$ and the structure factor $S(k)$ is given by Bosch and Collots [117]

$$S(k) = \frac{1}{1 - c(k)} \tag{4.24}$$

For a wavevector of magnitude k and the packing fraction η, the direct correlation function is

$$c(k; \eta) = \eta c_0 \left[4(1 - a^2\eta)f(k) + a^2\eta \left(\left\{ af\left(\frac{ak}{2} \right) \right\}^2 + H(k; a) \right) \right] \tag{4.25}$$

where f is an auxiliary function.

$$f(k) = \frac{2J_1(k)}{k} \tag{4.26}$$

with $J_1(x)$ being a Bessel function of the first kind, of order 1, and $H(k; a)$ is given by

$$H(k; a) = \frac{16}{\pi} \int_{1/a}^{1} dx \sqrt{(1 - x^2)}(f(k) - a^2 x^2 f(akx)) \tag{4.27}$$

where a is a scaling parameter parameter defined by

$$a(\eta) = \frac{(2 + \eta\alpha(\eta))}{1 + \eta\alpha(\eta)} \tag{4.28}$$

and $\alpha(\eta)$ is given as

$$\alpha(\eta) = -0.2836 + 0.2733\eta \tag{4.29}$$

In equation 4.25, c_0 is a scaling function, related to the prescribed equation of state

$$z(\eta) = \frac{1 + c_2\eta^2}{(1 - \eta)^2} \tag{4.30}$$

by the inverse compressibility

$$c_0 = -\frac{\partial \eta z(\eta)}{\partial \eta} \tag{4.31}$$

This results in

$$c_0 = \frac{-(1 + \eta + 3c_2\eta^2 - c_2\eta^3)}{(1 - \eta)^3} \tag{4.32}$$

where $c_2 = 7/3 - 4\sqrt{3}/\pi$.

Since the structure factor is the Fourier transform of the pair correlation function, $h(\mathbf{r}) = g(\mathbf{r}) - 1$, the structure factor $S(\mathbf{k})$ can be written as [118]

$$S(\mathbf{k}) = 1 + \rho \int d\mathbf{r}(g(\mathbf{r}) - 1)e^{i\mathbf{k}\cdot\mathbf{r}} \tag{4.33}$$

Equation (4.33) can be inverted to yield an expression for the radial distribution function $g(r)$.

$$g(r) = 1 + \frac{1}{\rho 2\pi} \int_0^\infty dk(S(k) - 1)kJ_0(kr) \tag{4.34}$$

Lado provides a discrete version of this particular Hankel transform [119]

$$g(r_i) = 1 + \frac{1}{\rho \pi R^2} \sum_{j=1}^{N-1} (S(k) - 1)\frac{J_0(k_j r_j)}{[J_0'(k_j R)]^2} \tag{4.35}$$

where r_i and k_j are defined as

$$r_i = \mu_i R/\mu_N \tag{4.36a}$$

$$k_j = \mu_j/R \tag{4.36b}$$

R is the range of the original function being transformed, which in this case is $g(r) - 1$. Outside the range of R, the function is assumed to vanish. μ_i is the ith

positive root of $J_0(x)$.

4.2.2 2D vapour-liquid coexistence and Joule-Thomson inversion curve

The calculation of the predicted liquid-vapour dome and JT inversion curves is performed in the same way as for the 3D case. The use of the analytical radial distribution function derived in the previous section does yield satisfying results, despite the calculations being very slow. In figure 4.8 the liquid-vapour dome and inversion curve for the 2D LJ/s potential with $r_c = 1.7$ is shown (orange line).

The liquid vapour dome is not closed sufficiently at higher temperatures to make any sensible statement about the predicted critical temperature, but it does predict a critical density at $\rho_c \approx 0.4$. The inversion curve predicts a maximum point at $T_{max} \approx 1.25$ and $P_{max} \approx 0.65$.
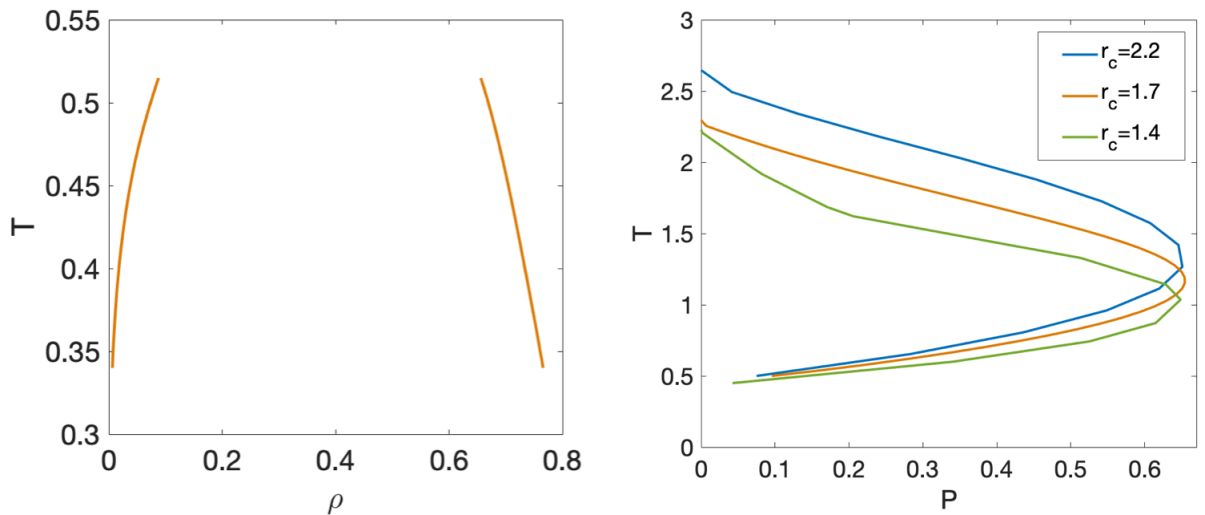
Figure 4.8: 2D perturbation results for the LJ/s potential with $r_c = 1.7$: binodal (left) and JT inversion curve (right). Using LJ reduced units.

Figure 4.8 also displays the JT inversion curves (left) of the longer spline $r_c = 2.2$ and the shorter spline $r_c = 1.4$. $r_c = 2.2$ has an estimated maximum temperature at $T_{max} \approx 1.4$ and $r_c = 1.4$ an estimated maximum temperature at $T_{max} \approx 1.1$. They both have the same associated pressure at the maximum $P_{max} \approx 0.65$.

It is worth noting that the long spline $r_c = 2.2$ does not display a bump in the inversion curve in 2D.

4.3   Concluding on perturbation theory.

In 3D, the same drop in critical temperature when the range of the potential is decreasing is consistent with what was seen for virial coefficient theory. 3D perturbation theory also predicted approximately the same critical density, which also did not change when changing the range of the potentials. The inversion curves predicted by perturbation theory seemed much more consistent. There was a clear pattern for the maximum temperature, which decreased with the range of the potentials. It could also be seen that the width of the inversion curves decreased with decrease in range, which was not clear from the virial coefficient results.

Compared to the MD results, obtained by Halfskjöld *et al.*, shown in figure 3.24, the perturbation result overestimates the critical temperature, but this is to be expected for a second order approximation. It is also deviating on the liquid branch, which should also be expected, as it is the density region where a deviation in the free energy is observed in figure 4.4.

Compared to the virials, the perturbation theory is able to predict liquid-vapour coexistence and inversions curves over a larger range. Also, the predicted liquid branch has a shape more representative of what is observed in the literature. As it was possible to obtain physically sensible results for the 2D LJ/s system, it can be concluded that the virial theory failed. It is not the case that liquid-vapour coxeistence does not exist. In figure 4.9, the 2D perturbation inversion curve is compared to constant enthalpy MD results. Overall the 2D perturbation results for the inversion curve showed a trend of the maximum temperature decreasing with the decreasing range of the potential, without changing the associated pressure. The maximum temperatures predicted for 2D were generally lower than in 3D.

It is worth noting that using the HS as a reference system for the *mn*-family of potentials seems valid, although it does not tend to infinity at the origin. This is contrary to the statement by Barker and Henderson that HS was only valid because the LJ potential goes to infinity at the origin. This could be because, locally, it appears very steep. It is possible to test this by using other reference systems that are more like the perturbed system, such as the Gaussian. People interested
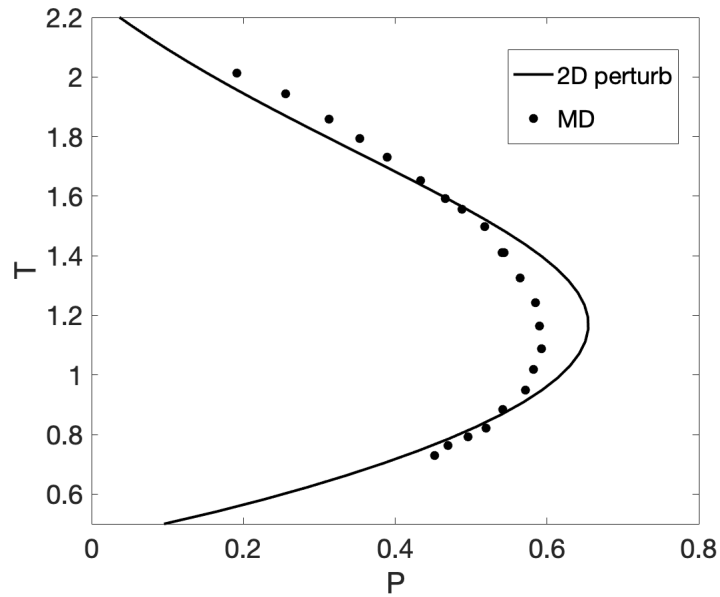
Figure 4.9: 2D inversion curve second order BH style perturbation theory (solid line) and constant enthalpy MD results (dots). Details on constant enthalpy MD simulation are given in chapter 5.

in SAFT, being a perturbation theory as well, have made extensive use of softer reference systems

When the second order BH perturbation theory was compared to MD results, a disagreement was found on the liquid-branch. To address this, it might be worth considering a different split of the pair potential, like the WCA split.

5 Direct constant enthalpy Molecular Dynamics simulations

Direct simulation in the NPT and NVT ensemble using MD is well used for the purpose of obtaining thermodynamic properties [30], to produce isochores and isotherms. However, in the case of determining the Joule-Thomson inversion curve using MD, the production of isenthalps is required. For this study, accurate isenthalps will confirm the accuracy of the theoretically predicted Joule-Thomson inversion curves in section 3 and 4.

Good results for Joule-Thomson inversion curve using MC have been obtained [25, 120], but attempts to use MD failed [121]. MC has many advantages over MD when producing thermodynamic properties (e.g easier to reached a desired state point in the simulation and/or move between different state points). However, it is easier to simulate complex molecules using MD, so there is a motivation for enabling MD to perform similar simulations to those done in MC.

The failure of the MD attempt to produce Joule-Thomson inversion curves, was due to the difficulties arising when attempting to control pressure and enthalpy using established equations of motion. Kioupis and Maginn [122, 123] proposed a solution to this, by introducing couplings between the pressure and enthalpy to an extended system. This resulted in modified equations of motion that allows isobaric-isothermal MD simulations.

This chapter presents an NPH-MD algorithm, which uses the equations of motion proposed by Kioupis and Maginn. The system used is a simple orthogonal cell, using coordinate restricted periodic boundary conditions. A system size of $N = 529$, 2D 4,8 potential particles was used and a total of 16 isenthalps in the pressure range $P = [0.01; 0.99]$ were produced.

5.1 Equations of motion

This section summarises the development of new equations of motion, by Kioupis and Maginn [122, 123], that will allow for direct simulation of isenthalp-isobaric

MD simulations. The equations of motion are given by the isobaric-isenthalpic equilibrium MD method [124–127]

$$\dot{\mathbf{r}}_i = \mathbf{v}_i + \chi \mathbf{r}_i \tag{5.1}$$

$$\dot{\mathbf{v}}_i = \frac{\mathbf{F_i}(\mathbf{r_i})}{m_i} - \chi \mathbf{v}_i \tag{5.2}$$

$$\dot{V} = 3V\chi \tag{5.3}$$

where r_i is the position of particle i, $\mathbf{v}_i$ the velocity of particle i, F_i is the force acting on particle i, m_i is the mass of the particle, χ is the strain rate of the system and V is the volume of the system. In order to keep the pressure constant, the volume is permitted to change.

The total energy of the system, E, is the sum of the kinetic and potential energy,

$$E = \frac{1}{2} \sum_i m_i v_i^2 + \sum_i \sum_{i>j} \phi_{ij} \tag{5.4}$$

Over time, the change in energy can be expressed as

$$\dot{E} = \sum_i m_i \mathbf{v}_i \cdot \dot{\mathbf{v}}_i - \sum_i \mathbf{F}_i \cdot \dot{\mathbf{r}}_i \tag{5.5}$$

substituting the equations of motion given in equations (5.1), (5.2) and (5.3) into the time derivative of the total energy in equation (5.5) as well as using the virial EoS yields a relationship between pressure and the time evolution of the total energy of the system.

$$3PV = \sum_i m_i \mathbf{v}_i^2 + \sum_i \mathbf{r}_i \cdot \mathbf{F}_i \tag{5.6a}$$

$$\dot{E} = -P\dot{V} \tag{5.6b}$$

From equation (5.6b) the time derivative of the enthalpy of the system can be written as

$$\dot{H} = \dot{P}V \tag{5.7}$$

Equations (5.6b) and (5.7) are both expressions for the first law of thermodynamics (conservation of energy), for an adiabatic (no transfer of heat nor mass) compression. It is obvious from equation (5.7) that for constant pressure ($\dot{P} = 0$) enthalpy must also be constant ($\dot{H} = 0$). The strain rate χ is allowed to vary, to maintain the pressure at a constant value.

The purpose is not just to keep some variables at a constant value, but also to drive variables to a pre-determined value, while keeping other variables constant. To do this in MD, temperature, T, must be kept constant as pressure, P, changes under the conditions for constant enthalpy, namely $\dot{P} \neq 0$ but $\dot{H} = 0$. This has, before the work of Kioupis and Maginn, [122] been difficult to obtain in MD simulations. They introduced a pressure coupling to an extended system, where the pressure in the extended system, P_{ext}, is coupled to the pressure of the considered system via a piston controller. By changing P_{ext}, a system consisting of N particles under pressure P will move towards the value of P_{ext}. Wang and Fichthorn [128] also allow for the change of pressure in an isobaric process by relating the time evolution of the pressure $\dot{P}$ to the desired pressure P_{set} and the instantaneous pressure of the system P.

$$\dot{P} = k_p(P_{set} - P) \tag{5.8}$$

where k_p is the proportionality constant. By integrating (5.8) using the initial pressure P_0 as the initial condition, the time dependent pressure becomes

$$P(t) = P_{set} + (P_0 - P_{set})\exp(-k_p T) \tag{5.9}$$

Having introduced a way of changing pressure during an isenthalpic process, Kioupis and Maginn proceed to present modified equations of motion to allow for direct enthalpy changes during an isobaric process. They introduce a force constraint $\alpha \mathbf{v}_i$, where α is a friction coefficient keeping enthalpy constant during pressure changes which, they show, has the form

$$\alpha = \frac{\dot{P}V - \dot{H}}{\sum_i m_i \mathbf{v}_i^2} \tag{5.10}$$

This leads to the following form for the equations of motion

$$\dot{\mathbf{r}}_i = \mathbf{v}_i + \chi \mathbf{r}_i \tag{5.11a}$$

$$\dot{\mathbf{v}}_i = \frac{\mathbf{F}_i(\mathbf{r}_i)}{m_i} - \chi \mathbf{v}_i - \alpha \mathbf{v}_i \tag{5.11b}$$

$$\dot{V} = 3V\chi \tag{5.11c}$$

The strain rate χ must also be changed to account for the introduction of the friction coefficient. Just as for pressure, the time derivative of the enthalpy is described in terms of desired value, H_{set}, and the instantaneous value H, which fixes the enthalpy of the system while allowing it to drift over time.

$$\dot{H} = k_H(H_{set} - H) \tag{5.12}$$

5.2 The NPH MD algorithm

The MD algorithm for directly producing isenthalps uses the modified equations of motion described in the previous section. This section provides information on the initial configurations used to start the simulation, which boundary conditions are being used and how thermodynamic properties are measured, in particular in relation to the production of isenthalps.

5.2.1 Initial configuration and boundary conditions

The two dimensional system is set up as a square, initially placing particles on an even grid as shown in figure 5.1.

The boundary conditions used are periodic, given for an orthogonal cell centred at the origin as shown in figure 5.2. X is defined as the length of the box in the x direction while Y is defined as the length of the box in the y direction. A particle that goes beyond the length of the cell at position x will re-enter on the opposite side, maintaining the same velocity. The boundary conditions use restricted coordinates
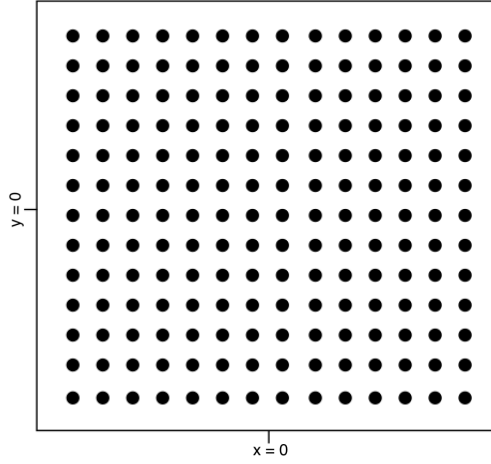
Figure 5.1: Initial configuration for 2D NPH MD simulation. Particles are placed on a regular square grid, in an orthogonal cell, which is centered on the origin.

as follows

$$\text{If} \quad x > \frac{1}{2}X \quad \text{then} \quad x = x - X \tag{5.13a}$$

$$\text{If} \quad x < -\frac{1}{2}X \quad \text{then} \quad x = x + X \tag{5.13b}$$

$$\text{If} \quad y > \frac{1}{2}Y \quad \text{then} \quad y = y - Y \tag{5.13c}$$

$$\text{If} \quad y < -\frac{1}{2}Y \quad \text{then} \quad y = y + Y \tag{5.13d}$$

How an exiting particle reappears at the opposite boundary is illustrated in figure 5.2.

5.2.2 Calculation of thermodynamic properties

Thermodynamic properties relevant for the production of isenthalps are pressure P, temperature T and enthalpy H. For each variable, the intermediate value is stored in an array and averaged over the number of time steps to yield an average value.

The local measurement of pressure corresponds to

$$P_{xy} = \frac{v_x^2 + v_y^2 + \sum_{j,j\neq i}^{N} x_{ij}^2 F_{ij}}{2XY} \tag{5.14}$$

where v_x is the velocity in the x-direction, v_y the velocity in the y-direction, x_{ij} the distance between particle i and j, F_{ij} the force exerted on particle i from particle j
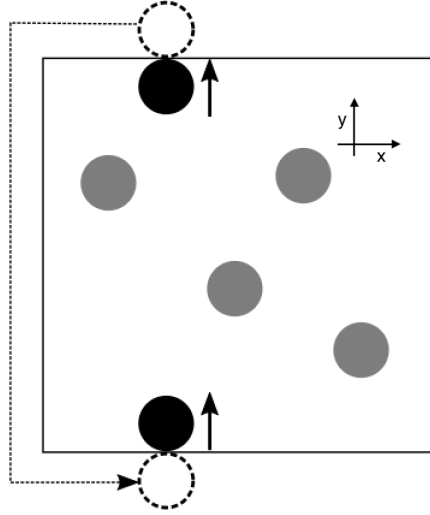
Figure 5.2: Diagram showing restricted coordinates periodic boundary conditions. A particle (black) exits the top of the box in the y direction, then reappears at the bottom maintaining the same position in x.

and XY is the area of the simulation system. The direct measurement of the local kinetic temperature corresponds to

$$T_{kin} = \frac{v_x^2 + v_y^2}{2(N-1)} \tag{5.15}$$

where $2(N-1)$ are the degrees of freedom. The local measurement of enthalpy H_{xy} is given by

$$H_{xy} = v_x^2 + v_y^2 + \phi_{ij} + \frac{x_{ij}^2 F_{ij} + y_{ij}^2 F_{ij}}{2N} \tag{5.16}$$

In practice, it is important to appreciate that the system is driven towards the desired enthalpy, and will not always correspond to the directly measured enthalpy. Long production runs should be performed, to ensure that the measured enthalpy corresponds with the desired enthalpy.

For a given enthalpy, several simulations are performed with varying pressure. This is all repeated for several values of enthalpy. In the next section, results from repeated constant enthalpy simulations are shown for the 2D 4,8 potential.

5.3 Constant enthalpy MD results

In order to obtain results for the Joule-Thomson inversion curve, several constant enthalpy simulations must be performed and their maxima determined as this corresponds to the point at which the Joule-Thomson coefficient μ_{JT} vanishes. An example of extracting maxima from isenthalps to yield an inversion curve is given in appendix D for the case of the analytical VDW system.

In practice several constant enthalpy simulation were performed using $N = 529$ particles with an equilibration run using 50000 time steps to melt the crystal, followed by a production run using 10^6 timesteps. 16 different values of enthalpy were used $H = [0.1; 0.5; 0.9; 1.0; 1.4; 1.8; 2.0; 2.2; 2.3; 2.4; 2.5; 2.6; 2.7; 2.8; 2.9; 3.0]$, in the pressure range $P = [0.01; 0.99]$. using 50 values. These simulations make up isenthalps which are displayed in figure 5.3.
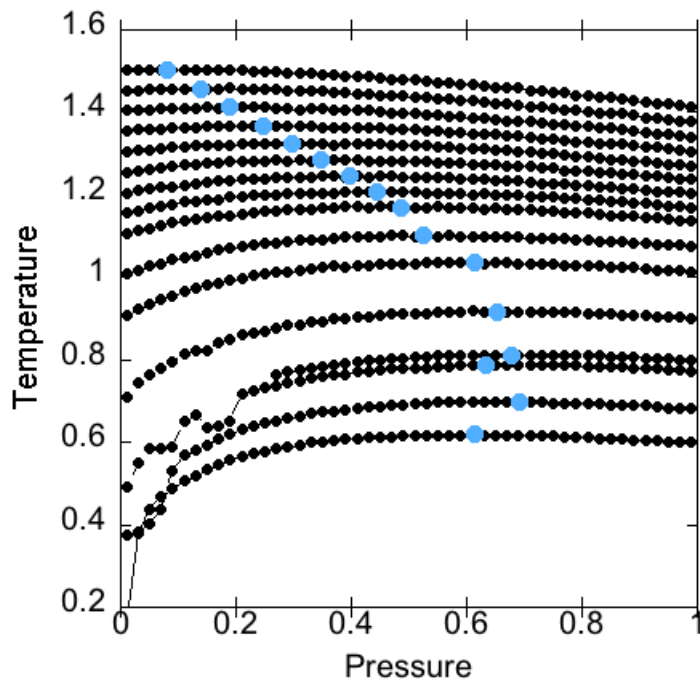
Figure 5.3: Isenthalps produced by repeated NPH MD simulations. Constant pressure and enthalpy MD simulations (black circle) and their maximum (blue circle). Using LJ reduced units.

Overall the isenthalps are smooth due to the long production runs and it is clear

that a sufficient number of pressures have been used to determine the maxima. At the low pressure and density region, due to low particle interaction under these conditions, the data is noisy. This is sufficiently far away from the point at which $\mu_{JT} = 0$ to have no effect on the determination of the Joule- Thomson inversion curve.

5.4 Conclusion

Extensive NPH MD simulations were performed at 16 different enthalpies using 50 different values of pressure in the region of $P = [0.01; 0.99]$, to yield smooth isenthalps. The method described in appendix D can be used to extract the value for each of the isenthalps at the point where the Joule-Thomson coefficient μ_{JT} vanished.

Although this method successfully yields a Joule-Thomson inversion curve, it is worth noting, that for the sole purpose of obtaining an inversion curve, only the simulations performed around the maxima, are required. The methods described in section 3 and 4 can give a reasonably fast theoretical estimate of where MD simulations should be performed to obtain accurate values for when $\mu_{JT} = 0$, without wasting computational resources and time.

6   Joule-Thomson Throttling of Gases

Early work on the freely expanding ideal gas in a vacuum, showed that the change in internal energy is independent of the change in volume [129, 130]. By 1845 Joule continued this work in his attempts to find the mechanical equivalence of heat. In 1852, together with Lord Kelvin, this resulted in what is today known as *Joule-Thomson throttling* [23]. The *Joule-Thomson Throttling* experiment was originally a thermally insulated lead pipe, where gas was pumped through at a steady rate, passing a porous plug situated in the centre of the construction. The temperature was carefully monitored and a drop in the temperature of the gas was observed. This phenomenon is the basis of various modern technologies such as refrigeration, air conditioning, heat pumps and liquefiers [131, 132].

The non-equilibrium molecular dynamics realisation of Joule-Thomson throttling developed by Hoover *et. al.*, provides an interesting new way to study non-equilibrium steady states with simple boundary conditions. The work of these authors showed a small temperature drop when the gas was based on a purely repulsive pair potential. This presents a puzzle since the Joule-Thomson effect was used to prove the existence of attractive forces.

In this section the Joule-Thomson simulation is revisited but using a potential with an attractive component to investigate whether a temperature drop may occur and understand why it did in the original work.

6.1   Joule-Thomson throttling of a purely repulsive potential.

In 2014 Hoover, Hoover and Travis [20] successfully demonstrated that molecular dynamics can be used to model shock waves. A two dimensional shock wave is travelling in one dimension, using a purely repulsive pair potential. Cold fluid enters the left side of a simulation box, meeting a hot fluid which exits to the right.

Shock waves and Joule-Thomson throttling differ in 2 key ways. (1) for Joule-Thomson throttling, kinetic energy is negligible, which is not the case for shock waves. (2) In shock waves the conductive heat flux is at its maximum at the wave

front, whereas it is invisible in Joule-Thomson throttling due to the porous plug. However, they also have similarities. (1) The flow of particles happens in one direction. (2) They have the same thermodynamics. (3) Both have constant fluxes. Therefore it should be possible to construct a successful MD simulation of a Joule-Thomson throttling.

6.1.1 Boundary conditions and plug.

The boundary conditions are easily revised to suit the Joule-Thomson simulation. Instead of simulating a porous plug, a potential barrier is placed in the middle of the system perpendicular to the flow. The sole purpose of the obstruction is to strip momentum from the incoming gas, so a potential barrier will suffice. A gaussian-like potential was chosen as it is short ranged and sufficiently smooth. The barrier potential and its force are given in equations (6.1) and (6.2) and illustrated in figure 6.1.

$$\phi_{barrier}(x) = \frac{1}{4}\left(1 - x^2\right)^4 \tag{6.1}$$

$$F_{barrier}(x) = 2x(1 - x^2)^3 \tag{6.2}$$

A purely repulsive potential was chosen for the pair interaction of the particles

$$\phi(r < 1) = [1 - r^2]^4 \tag{6.3}$$

and the force

$$F(r < 1) = 8r(1 - r^2)^3 \tag{6.4}$$

which are illustrated in figure 6.2. The potential was slightly modified to alleviate the possible problem of compressibility at high densities. The force is capped at the point of inflexion.

The one dimensional steady flow of gas is created via the boundary conditions. At a steady state, columns of particles are fed into the simulation from the left side
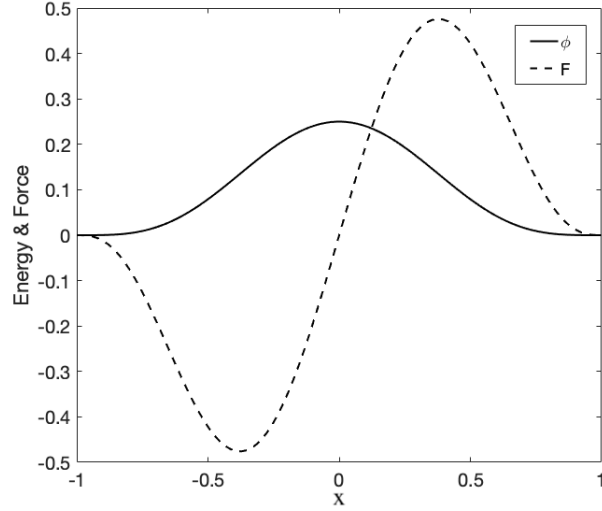
Figure 6.1: Barrier potential and barrier force from equation (6.1) (solid line) and (6.2) (broken line).

of the system. Particles are ejected from the system when they reach the boundary at the right side of the system. The particles are allowed to exist in a small region, beyond the border, before they are discarded.

6.1.2 Equations of motion and calculation of fluxes

The trajectories in the 2D JT throttling use Newton's second law of motion derived from the Hamiltonian $H = \sum_k \dot{\mathbf{q}}_k \mathbf{p}_k - L$ [55]

$$\ddot{r} = \dot{v} = \frac{F}{m} \tag{6.5}$$

The advantage of using the Hamiltonian derived equation of motion, rather than the Lagrangian, is simpler equations of motion. Newtonian equations of motion are integrated using a fourth order *Runge-Kutta* algorithm [55]. It is self starting and has an associated error of order $\Delta t^4/5!$. It calculates the trajectories doing four intermediate calculations within the time step.

$$\mathbf{r}_i(1) = \mathbf{r}_i(t) + \dot{\mathbf{r}}(t)\Delta t \tag{6.6a}$$

$$\mathbf{v}_i(1) = \mathbf{v}_i(t) + \dot{\mathbf{r}}_i(t)\Delta t \tag{6.6b}$$

114
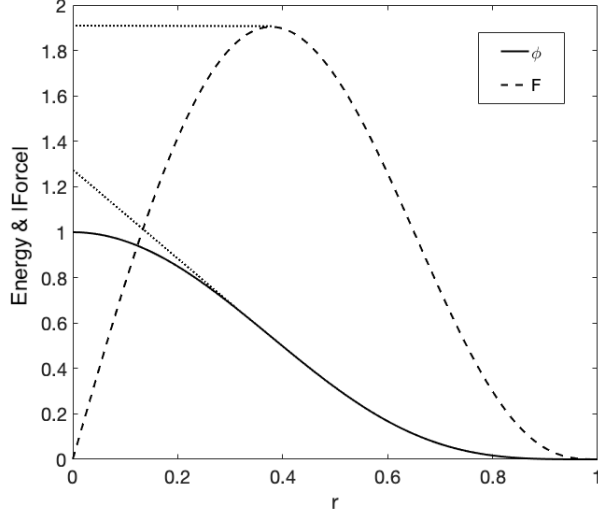
Figure 6.2: Pair potential and force of the gas particles in the Joule-Thomson throttling.

$$\mathbf{r}_i(2) = \mathbf{r}_i(t) + \dot{\mathbf{r}}_i(1)\frac{\Delta t}{2} \tag{6.7a}$$

$$\mathbf{v}_i(2) = \mathbf{v}_i(t) + \dot{\mathbf{v}}_i(1)\frac{\Delta t}{2} \tag{6.7b}$$

$$\mathbf{r}_i(3) = \mathbf{r}_i(t) + \dot{\mathbf{r}}_i(2)\frac{\Delta t}{2} \tag{6.8a}$$

$$\mathbf{v}_i(3) = \mathbf{v}_i(t) + \dot{\mathbf{v}}_i(2)\frac{\Delta t}{2} \tag{6.8b}$$

$$\mathbf{r}_i(4) = \mathbf{r}_i(t) + \dot{\mathbf{r}}_i(3)\Delta t \tag{6.9a}$$

$$\mathbf{v}_i(4) = \mathbf{v}_i(t) + \dot{\mathbf{v}}_i(3)\Delta t \tag{6.9b}$$

Then each intermediate time step is averaged, yielding the final trajectories at time $t + \Delta t$.

$$\mathbf{r}_i(t + \Delta t) = \mathbf{r}_i(t) + \left[\frac{\dot{\mathbf{r}}_i(1)}{6} + \frac{\dot{\mathbf{r}}_i(2)}{3} + \frac{\dot{\mathbf{r}}_i(3)}{3} + \frac{\dot{\mathbf{r}}_i(4)}{6}\right]\Delta t \tag{6.10a}$$

$$\mathbf{v}_i(t + \Delta t) = \mathbf{v}_i(t) + \left[\frac{\dot{\mathbf{v}}_i(1)}{6} + \frac{\dot{\mathbf{v}}_i(2)}{3} + \frac{\dot{\mathbf{v}}_i(3)}{3} + \frac{\dot{\mathbf{v}}_i(4)}{6}\right]\Delta t \tag{6.10b}$$

$$\text{mass flow} = \rho u$$

$$\text{momentum flow} = P_{xx} + \rho u^2 \tag{6.11}$$

$$\text{energy flow} = (\rho u)[e + (P_{xx}/\rho) + (u^2/2)]$$

where u is the flow velocity, determining the feed time of new particles into the system $(= \frac{1}{2}(u_L \Delta t)^{-1})$. P_{xx} the xx component of the pressure tensor, and e the specific internal energy. The fluxes are calculated using SPAM averaging [55]. SPAM averaging defines local averages where contributions from many nearby particles are considered. At position r for the variable f, the added nearby particle contributions $f(r_i)$ leads to an interpolated average value $f(r)$

$$f(r) = \sum_i m_i f_i w(r - r_i) / \sum_i m_i w(r - r_i) = \sum m_i f_i w_{ri} / \rho(r) \tag{6.12}$$

which leads to

$$f(r)\rho(r) \equiv f_r \rho_r \equiv (f\rho_r) \equiv \sum_i f_i m_i w(r - r_i) \equiv \sum_i f_i m_i w_{ri} \tag{6.13}$$

where $\rho(r)$ is the smooth particle density $= \rho_r = \sum_j m_j w(r - r_j)$ and w a Lucy weight function. The Lucy weight function is given in terms of the maximum distance to the included neighbouring particles [55]

$$w(r) = \left(\frac{5}{\pi h^2}\right)\left[1 + 3\frac{r}{h}\right]\left[1 - \frac{r}{h}\right]^3 \tag{6.14}$$

using the appropriate two dimensional normalisation factor $\int_0^h 2\pi r w(r) dr = 1$. The simulation makes no use of a thermostat.

The momentum flow described in equation (6.11) was calculated by

$$\text{momentum flux} = w(r) \times \left(\frac{1}{2R}x_{ij}^2 \times F_{ij} + u_x\right) \tag{6.15}$$

where u_x is the intermediate velocity at position x, R is the separation between the two particles, x_{ij} is the position of particles i and j, F_{ij} the force between the two

particles which is dependent on the pair potential and u_L is the velocity to the left of the potential barrier. The momentum flux is then divided by the length of the simulation box and averaged over all the produced time steps to give a final profile. The pressure tensor P_{xx} was calculated by

$$P_{xx} = w(r) \times \left(\frac{1}{2R} x_{ij}^2 F_{ij} + (u_x - u_L) \right)^2 \tag{6.16}$$

which is also averaged over all time steps to give a final profile.

6.1.3 Simulation details

The simulation was performed with dimensions: 200 columns in the x direction and in the y-direction 40 rows of particles are added with unit spacing, placing the potential barrier at $x/2$, starting the particles on a square lattice. Although the simulation aims to throttle a gas, it is favourable to use a square lattice (or a triangular), to ensure that the particles experience an even strength of the force from pair potential. The initial particle configuration is shown in figure 6.3.
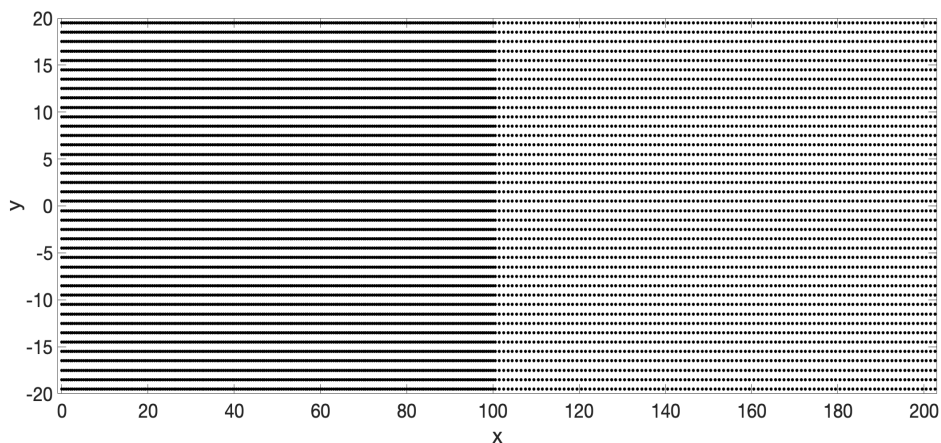
Figure 6.3: The initial position of particles, used for the JT MD throttling. Particles are placed on a square lattice with a two fold compression on the left hand side of the plug.

The particles require initial conditions. The conditions were set to reproduce the results by Hoover, Hoover and Travis [20] which were: initial velocity to the left of the plug $u_L = 0.5$, initial velocity to the right of the plug $u_R = 1.0$, where

a velocity at 1.0 is equal to the speed of sound. The left and right velocities are related to the rate at which particles are inserted to the left, and removed from the right. These need to be chosen appropriately to ensure a suitable flow. Thermal momenta are specified consistent with an initial temperature $T_0 = 0.05$ and the Gaussian potential barrier height is set at 0.25. This needs to be high enough to act as a porous plug, but not so high as to stop any particles coming through.

6.1.4 Results for purely repulsive potential

Using the initial conditions above, the results by Hoover, Hoover and Travis were reproduced. The simulation was run for 1500000 timesteps. The particles have lost their initial lattice structure as is shown in figure 6.4.
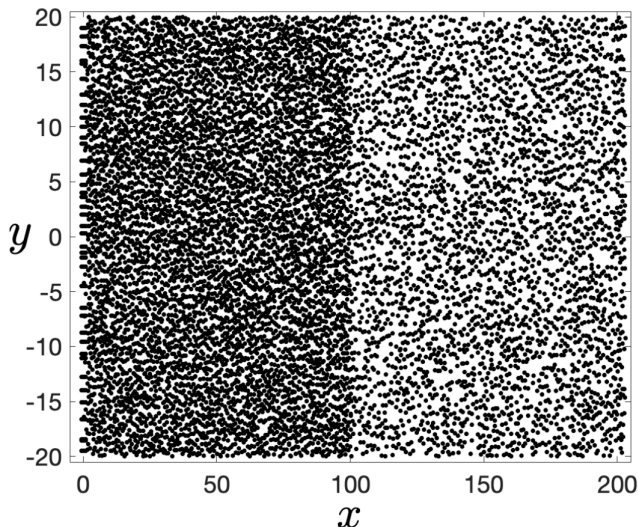
Figure 6.4: Final configuration for purely repulsive potential.

The resultant density profile is shown in figure 6.5, which shows a density to the left hand side of the plug of $\rho = 1.6$ which decreases to a density of $\rho = 0.8$ on the right hand side of the plug. The flux of mass, momentum and energy is shown in figure 6.6. A drop in momentum is observed from 1.7 on the left hand side to 1.5 on the right hand side. Energy and mass are kept constant at 1 and 1.3 respectively. A small drop in energy is seen at the plug. The profiles of velocity u_x and of tensor pressure components p_{xx} and p_{yy} are shown in figure 6.7. The velocity to the left hand side is 0.6 increasing to 1.25 on the right hand side. The pressure tensor components, p_{xx} and p_{yy}, are equal to each other, being one on the left hand
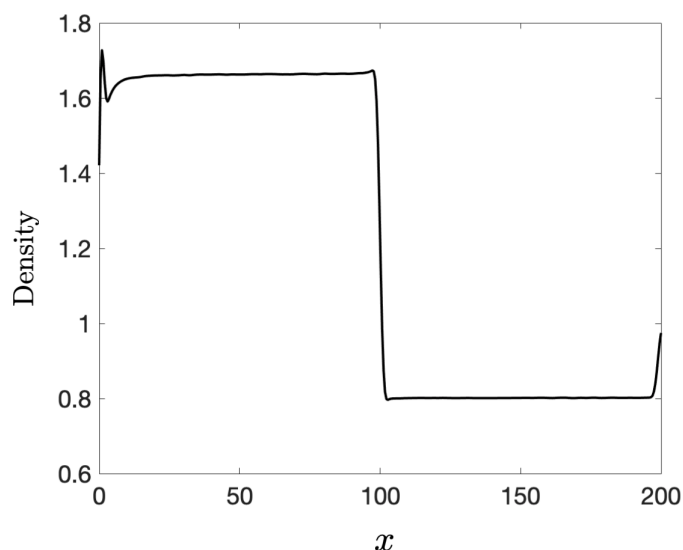
Figure 6.5: Density profile for JT throttling using a purely repulsive potential.
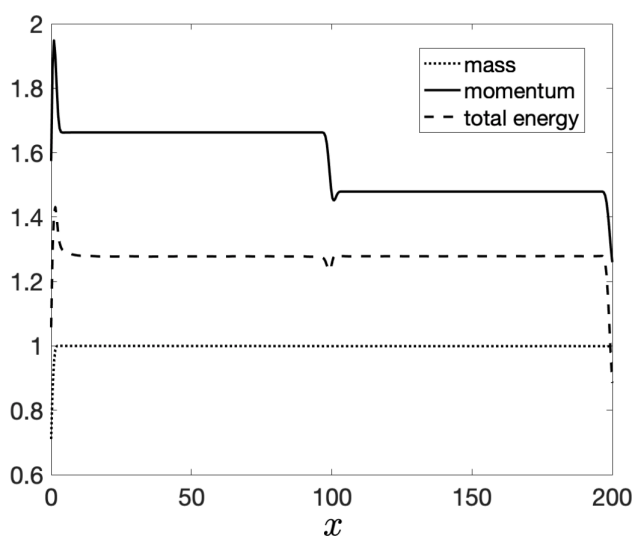
Figure 6.6: Momentum, mass and energy fluxes from 2D Joule-Thomson throttling, using a purely repulsive potential.

side decreasing on the right hand side to 0.2. The profiles of the components of the temperature tensor, T_{xx} and T_{yy}, are shown in figure 6.8. This shows a decrease in temperature for both from 0.25 to 0.16.

All of these profiles are consistent with those obtained obtained by Hoover, Hoover and Travis. It is puzzling that a drop in temperature is observed when using a purely repulsive potential, because the original experiment by Joule and Lord Kelvin was constructed to prove the existence of attractive forces. As discussed in chapter 1, for an ideal gas being throttled at constant enthalpy, the temperature
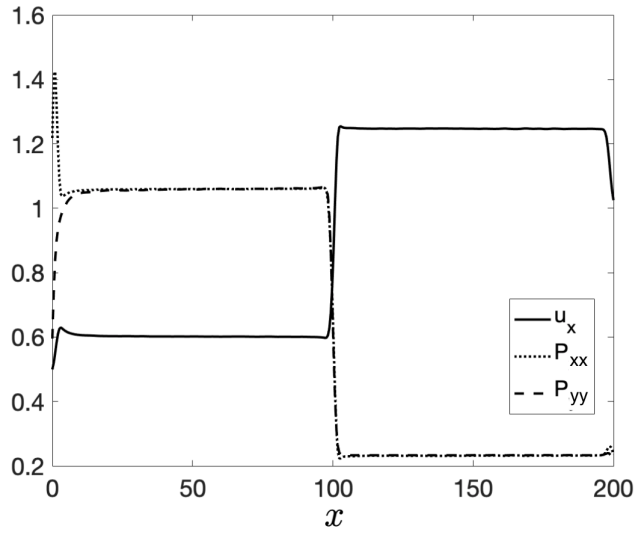
Figure 6.7: Velocity and pressure profiles of 2D Joule-Thomson throttling.
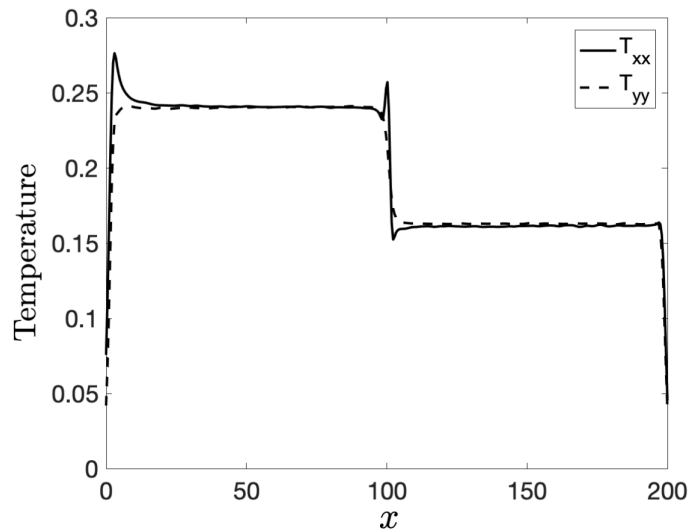
Figure 6.8: Temperature profiles of 2D Joule-Thomson throttling.

will likewise be constant. At low temperatures, the attractive part of the potential dominates the repulsive part. Further investigation showed that the observed drop in temperature was due to the simulation not being isenthalpic. The enthalpy profile in the throttling direction is measured as

$$H(x) = w(r) \times \left(0.5 \times \left(\frac{1}{2R} x_{ij}^2 F_{ij} + \frac{1}{2R} y_{ij}^2 F_{ij} \rho^{-1} + 0.5 E_{ij} + 0.5 \times (u_x - u_L)^2 + u_y^2 \right) \right)$$

(6.17)

where u_y is the intermediate velocity in the y-direction and shown in figure 6.9, which is not constant. There is a clear drop in enthalpy from 1.65 to 0.8 after the throttling. In an attempt to move the system towards constant enthalpy, the initial velocities
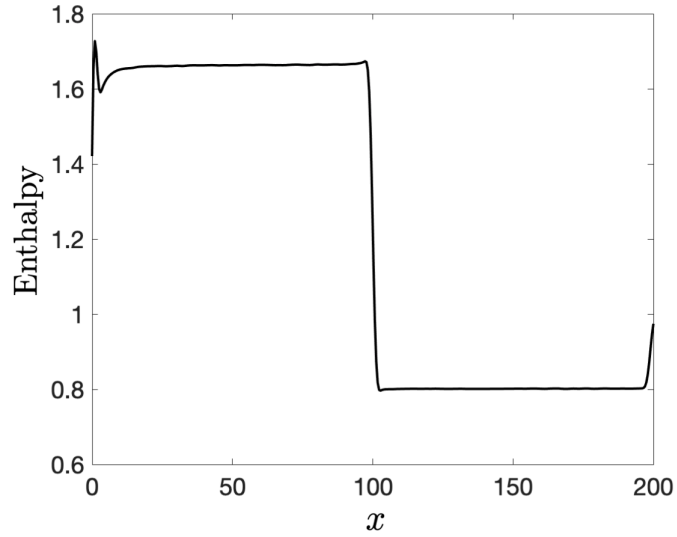
Figure 6.9: Enthalpy profile of 2D Joule-Thomson throttling, for the repulsive disk system.

were decreased to very low values of $u_L = 0.001$ and $u_R = 0.005$, still keeping a velocity difference to enable flow through the system. The initial temperature was also decreased from the original simulation to $T_0 = 0.001$. The result for the enthalpy after 150000 time steps are shown in figure 6.10. It is observed that the drop in enthalpy has decreased significantly. However, the system is losing its temperature profile, it now appears more like a gradient than a defined temperature drop, as is seen in figure 6.10. It does not seem to be possible, for this system, to achieve constant enthalpy and a temperature drop as expected for a JT throttling. It could

be discussed whether or not the choice of boundary conditions were appropriate and if they are the cause of the enthalpy problem. However, this would imply that Hoover, Hoover and Travis' work on the 1D shock wave is wrong, for which there was no indication.
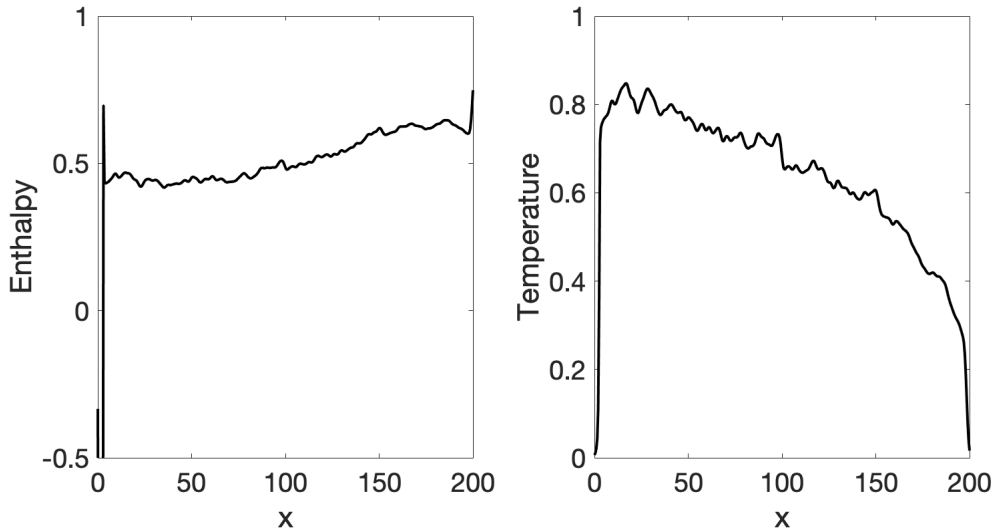
Figure 6.10: JT throttling results for the purely repulsive potential for (left) Enthalpy and (right) Temperature.

Since the original experiment was designed to prove the existence of attractive forces, using a potential with an attractive component could results in a constant enthalpy profile while keeping the drop in temperature.

6.1.5 Results for potential with an attractive component

In this section the JT throttling simulation is repeated using a potential with an attractive component. The 2D $m = 4$ and $n = 8$ was chosen, as a longer range potential seemed to have a wider inversion curve, and for convenience, as constant enthalpy MD simulations are available. A few changes to the original simulation had to be undertaken to accommodate the presence of attractive forces. Firstly the initial condition has to be altered, as using the square lattice with unit spacing, caused the system to condense fairly quickly, if the initial density does not corresponds to an appropriate phase point in the gas region. The initial grid was changed to a triangular lattice, keeping the two fold compressions, but increasing the distance

between particles to be greater than the potential cut off distance. The initial configuration is displayed in figure 6.11.
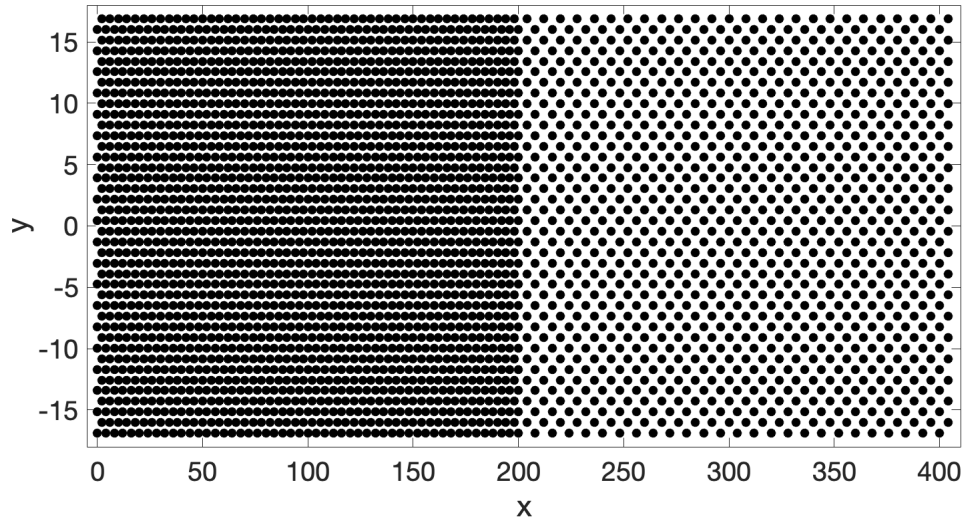
Figure 6.11: Initial particles configuration for the 2D $4, 8$-potential.

Initial values for the simulation must be chosen in such a way that the throttling exists within the JT inversion curve. In figure 6.12 the inversion curve predicted by virial coefficient theory and constant enthalpy MD simulations is shown. From this it is possible to see at what values of pressure and temperature a cooling from a throttling will occur.

The simulation was started with an initial reduced temperature of $T_0 = 1.0$, since aiming to throttle in the middle of the temperature range of the inversion curve gives the widest range of suitable pressures. The inlet and outlet velocities had to be set rather high, at LJ reduced velocities $u_L = 2.5$ and $u_R = 5.0$ (in comparison speed of sound $= 1$), otherwise the flow of the simulation reversed. The barrier height was also increased to a value of 3.5, to raise the pressure into the area of the inversion curve. It is worth noting that no values in the input file allow for the direct control of temperature and pressure, remembering that there is neither a thermostat or barostat present. Therefore setting initial conditions to achieve appropriate pressure and temperature still involves a trial and error approach.

The final configuration after 50000 time steps is given in figure 6.13. It is noticeable that particles seem to cluster at the potential barrier. This should not have
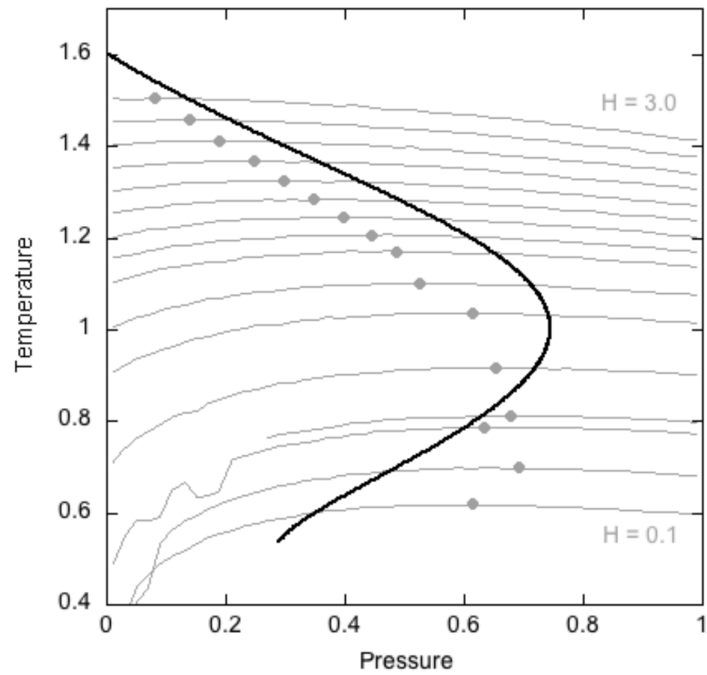
Figure 6.12: JT inversion curve for the 2D $4, 8$ potential. Showing predicted inversion curve by virial coefficient theory (solid black), isenthalps (solid grey) and maxima for the isenthalps (grey dots).

an effect on the profiles as such, but would indicate that the barrier is too high compared to the flow. Lowering the barrier height will make the configuration more uniform. The density profile for the simulation is given in figure 6.14, showing the
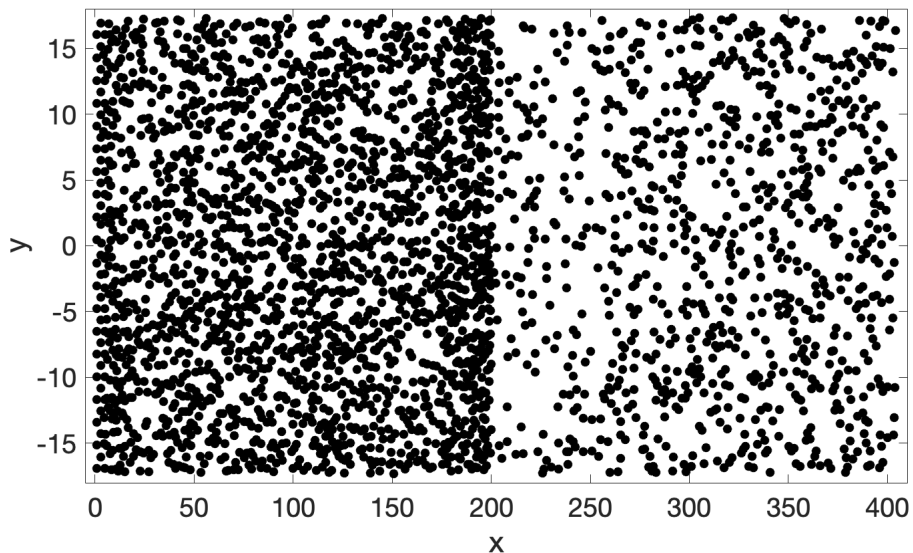
Figure 6.13: Final configuration for the throttling using the 2D $4, 8$-potential.

expected density decrease as well as the condensation close to the left hand side of the barrier, echoing the configuration seen in figure 6.13.
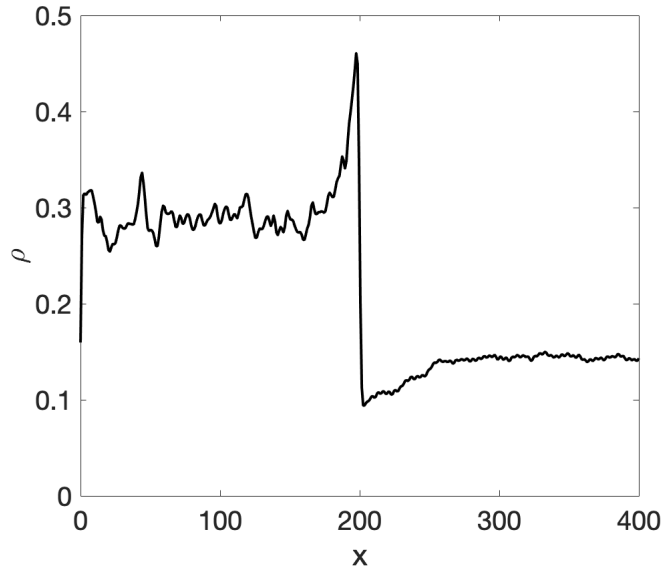
Figure 6.14: Density profile of the JT throttling using the 2D 4,8 potential.

In figure 6.15, the profiles for pressure and temperature are given. Approximate values can be made out, despite the data still being noisy. The pressures $P_L \approx 0.5$ and $P_R \approx 0.15$. The temperatures are $T_L \approx 1.2$ and $T_R \approx 1.1$. Note that these temperatures are not identical to the initial temperature, as there is no temperature control. The initial temperature is merely there to provide starting energies to the MD particles. The initial pressure is within the predicted inversion curve, but it falls just outside the inversion curve calculated via MD. The final pressure is however well within the inversion curve. Looking at the temperature profile, the drop in temperature is small, but considering the shape of the isenthalps in figure 6.12, only a small drop in temperature is to be expected. The effect from the clustering at the potential barrier observed in the configuration in figure 6.13 is seen as a sharp increase in pressure and temperatures in figure 6.15, but as expected it does not have much effect on the overall profiles.

The enthalpy profile is given in figure 6.16, which although noisy, does not display the significant drop in enthalpy that were observed in figure 6.9, in the reproduction of the original simulation for a purely repulsive potential. Note that the large spikes in figure 6.15 and figure 6.16, occurs due to the potential barrier that causes particle to condense just before it.
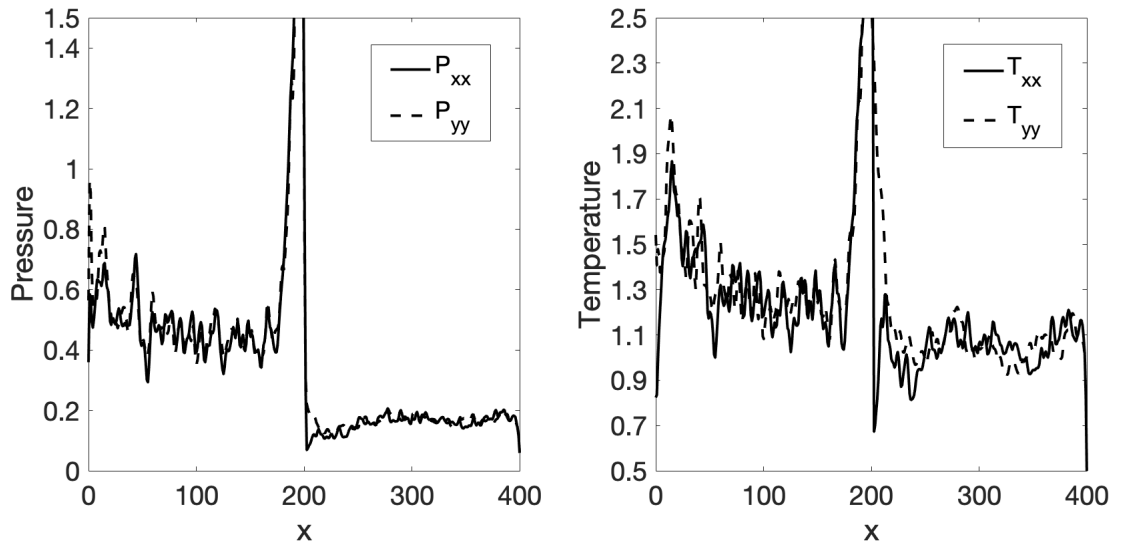
Figure 6.15: Pressure profile (left) and temperature profile (right) for the 2D throttling of the $4, 8$ potential.
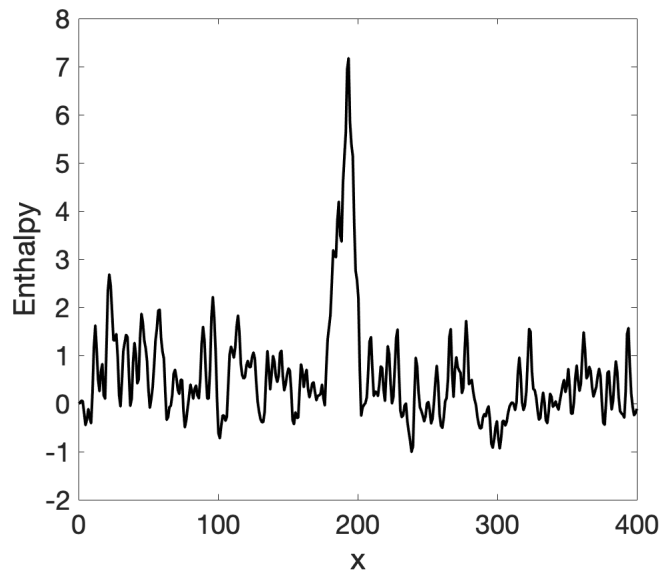
Figure 6.16: Enthalpy profile for the 2D $4, 8$ potential JT throttling.

6.2 Conclusion

The original simulation done by Hoover, Hoover and Travis, using a purely repulsive potential was reproduced successfully. A further investigation into the original results, showed that although a temperature drop was observed, the process was not isenthalpic. In an attempt to rectify this, the flow rate and initial temperature of the system was lowered significantly. It was found that the significant drop in enthalpy did diminish but, in the process the temperature profile was lost.

Another solution to address the enthalpy problem was to use a potential with an attractive component. This is because, as van der Waals realised at the time, the original experiment proved the existence of attractive intermolecular forces. Adjustments need to be made to the initial conditions to account for the presence of attractive forces. The $m = 4$ and $n = 8$ potential from the mn family was selected and the predicted inversion curve was used to determine the initial values for the throttling.

It was found that there was a drop in temperature while keeping the enthalpy constant. The values observed matched well with the MD data obtained for constant enthalpies.

7   Conclusion

This study sought to present an algorithm that represented a true JT throttling of a gas, which required a potential with an attractive component rather than the purely repulsive potential originally used. It was decided to look into two different families of pair potentials: the mn-family and the LJ/s family, due to their suitable mathematical properties for MD simulations. The phase diagram and JT inversion curves for these potentials were unknown, but are required for the purpose of JT throttling. Two theoretical methods were employed to predict the phase diagrams and inversion curves: Virial coefficient theory and a Barker Henderson style perturbation theory.

The virial coefficient theory only yielded a general usefulness of the second and third coefficient, from which binodals and inversion curves for the potentials were produced in two and three dimensions. The perturbation theory yielded results for all of the potentials in three dimensions. A 2D perturbation theory was also performed, but due to being significantly slower, a limited number of results were presented. Generally it was observed that as the range of the potential decreased, so did the critical temperature.

Using the predicted JT inversion curve for the 2D $m = 4$ and $n = 8$ potential, a JT throttling showing a drop in temperature with constant enthalpy was performed.

The choice of potential used was mainly due to convenience as MD simulations for constant enthalpy were available from section 5. Considering the trend of the liquid-vapour coexistence, there may be more viable choices. As was seen for the study in fullerenes, the liquid-vapour dome moved down as the range of the potential decreased, making a stable liquid phase disappear. Choosing such a potential could be advantageous, as condensation of the gas is undesirable in JT throttling.

There could be a question of whether or not the puzzling feature of the Hoover, Hoover and Travis publication was due to inappropriate choice of boundary conditions, however, this would imply that their results from their work on the 1D shock wave is wrong as it uses identical boundary conditions. The 1D shock wave work had no error, so it can be assumed that the boundary conditions used were indeed

appropriate.

To address the question, of whether or not the potentials studied have a stable liquid phase, it is necessary to investigate the sublimation line in order to establish the triple point. Doing this will show whether the critical temperature, as it decreases, will find itself under the triple point, as was seen for the study in carbon discussed in section 1.2.2. An approach to determine the sublimation line could be: (1) Determine the high pressure (solid phase) part of an isotherm, at a temperature lower than the best guess at the triple point temperature, then fit a polynomial to the pressure versus density. (2) Obtain the low pressure (vapour phase) region of the same isotherm. Fit a polynomial to the pressure versus density curve, aided by the first two viral coefficients calculated according to section 3.4. (3) Integrate vapour pressure to obtain the free energy of the vapour at this temperature. (4) Estimate the stress free density of the triangular lattice with this pair potential - several NVT simulations are performed at different densities but at zero temperature (only a single MD step is needed). A plot of pressure (which is just the virial since this is at zero temperature) vs density is produced and one interpolates to find the density giving rise to zero mechanical pressure. (5) Run a Frenkel-Ladd simulation at the stress free density and temperature of interest to determine the absolute free energy of the reference state. (6) Convert the free energies to chemical potentials using standard thermodynamic expressions. (7) Integrate the solid branch of the isotherm and combine with the free energy of the reference state to yield an equation for the free energy of the solid at any density. (8) Solve the pair of simultaneous equations for equality of chemical potential and pressure to obtain the coexisting solid and vapour densities at this temperature.

References

[1] W. T. Sommer. "Liquid Helium as a Barrier to Electrons". *Phys. Rev. Lett.*, **12**(11), (1964).

[2] S. V. Morozov D. Jiang I. M. Katsnelson I. V. Grigorieva S. V. Dubonos A. A. Firsov K. S. Novoselov, A. K. Geim. "Two dimensional gas of massless Dirac fermions in graphene". *Nature*, **438**(7065), (2005).

[3] H. L. Stormer P. Kim Y. Zhang, Y. W. Tan. "Experimental observations of the quantum Hall effect and Berry's phase in graphene.". *Nature*, **438**(7065), (2005).

[4] Qunqing; Xie Jing; Jin Zhong; Wang Jinyong; Li Yan; Jiang Kaili Wang, X.; Li. "Fabrication of Ultra long and Electrically Uniform Single-Walled Carbon Nanotubes on Clean Substrates". *Nano Letters*, **9**(9), (2009).

[5] G. Roberts. *"Langmuir-blodgett films"*. Springer Science & Business Media, (2013).

[6] Z.; Nemoto Y.; Sakka Y.; Hall S. R. Boston, R.; Schnepp. "In Situ TEM Observation of a Micro crucible Mechanism of Nanowire Growth". *Science*, **344**(6184), (2014).

[7] S. Mohammad and A. Khaledi-Nasab. "Size-dependent inter subband optical properties of dome-shaped InAs/GaAs quantum dots with wetting layer". *Applied Optics*, **51**(18), (2014).

[8] W. G. Hoover and C. G. Hoover. *"Simulation and Control of Chaotic Nonequilibrium Systems"*. Advanced Series in Non-linear Dynamics Vol 27, (2015).

[9] F. Galton. *"Natural Inheritance"*. Macmillan and Company, (1894).

[10] W. G. Hoover. *"Computational Statistical Mechanics"*. Elsevier, (1991).

[11] W. G. Hoover B. Moran and S. Bestiale. "Diffusion in a Periodic Lorentz Gas". *J. of Stat. Phys.*, **48**(34), (1987).

[12] C. Dellago and Wm. G. Hoover. "Finite-precision stationary states at and away from equilibrium". *Phys. Rev. E*, **62**(5), (2000).

[13] C. G. Hoover W. G. Hoover and J. C. Sprott. "Non equilibrium system: hard disks and harmonic oscillators near and far from equilibrium.". *Molecular Simulation*, **42**(1300-1316), (2016).

[14] W. G. Hoover and C. G. Hoover. "Three lectures: NEMD, SPAM and shock-waves". *AIP Conference Proceedings*, **1332**(23), (2011).

[15] K. P. Travis and K. E. Gubbins. "Poiseuille flow of Lennard-Jones fluids in narrow slit pores.". *J. Chem. Phys*, **112**(1984), (2000).

[16] K. P. Travis and K. E. Gubbins. "Transport Diffusion of Oxygen-Nitrogen Mixtures in Graphite Pores: A Non-equilibrium Molecular Dynamics (NEMD) Study.". *Langmuir*, **15**(18), (1999).

[17] B. D. Todd K. P. Travis and J. Denis. "Departure from Navier-Stokes hydro-dynamics in confined liquids". *J. Chem. Phys.*, **104**(23), (1996).

[18] K. P. Travis J. S. Hansen, P. J. Davis and B. D. Todd. "Parameterization of the nonlocal viscosity kernel for an atomic fluid". *Phys. Rev. E*, **76**(041121), (2007).

[19] J. Zhang P. J. Cadusch, B D Todd and P. J Daivis. "A non-local hydrodynamic model for the shear viscosity of confined fluids: analysis of a homogenous kernel". *J. of Phys. A*, **41**(035501), (2008).

[20] C. G. Hoover W. G. Hoover and K. P. Travis. "Shock-Wave Compression and Joule Thomson Expansion". *Phys. Rev. Lett.*, **112**(144504), (2014).

[21] W. Hoover and C. Hoover. "Tensor temperature and shock-wave stability in a strong two-dimensional shock wave". *Phys. Rev. E.*, **80**(1), (2009).

[22] Wm. G. Hoover and Carol G. Hoover. "Well-posed two-temperature constitutive equation for stable dense fluid shock waves using molecular dynamics and

generalizations of Navier-Stokes-Fourier continuum mechanics.". *Phys. Rev. E*, **81**(046302), (2010).

[23] J.P. Joule and W. Thomson. "LXXVI. On the thermal effects experienced by air in rushing through small apertures". *The London, Edinburgh and Dublin philosophical magazine and journal of science*, **4**(28), (1852).

[24] M. W. Zemansky and R. H. Dittman. *"Heat and Thermodynamics"*. The McGraw-Hill Companies INC., (1997).

[25] C. M. Colina and E. A. Müller. "Molecular Simulation of Joule-Thomson Inversion curves". *International Journal of Thermophysics*, **20**(1), (1999).

[26] H-C. Chang G. Arya and E. J. Maginn. "A critical comparison of equilibrium, non-equilibrium and boundary driven molecular dynamics techniques for studying transport in microporous materials.". *J. Chem. Phys*, **115**(8112), (2001).

[27] Y. Zhang S-I Furukawa, A. Fukui and T. Nitta. "Influence of Gas-Solid Kinetic Energy Exchange Processes on Gas Effusion from Slitpores in Non-equilibrium Molecular Dynamic Simulations". *Molecular Simulation*, **30**(6), (2004).

[28] R. Lesar. *"Introduction to Computational Material Science"*. Cambridge University Press, (2013).

[29] M. P. Allen and D. J. Tildesley. *"Computer Simulation of Liquids"*. Oxford University Press, Oxford(England), (1989).

[30] D. Frenkel and B. Smith. *Understanding molecular simulation: from algorithms to applications*. Academic Press, San Diego, Second Editions, (2002).

[31] D. W. Brenner. *"The Art and Science of An Analytical Potential"*. Phys. Stat. Sol. (b) 217, (2000) pp 23-40.

[32] J. P. Hansen and I. R. McDonald. *"Theory of Simple Liquids"*. Academic Press, London, (1990).

[33] Ángel Mulero. *"Theory and Simulation of Hard-Sphere Fluids and Related Systems"*. Springer Nature Switzerland, (2008).

[34] M. D. Rintoul and S. Torquato. "Hard-Sphere statistics along the metastable amorphous branch". *Phys. rev. E.*, **58**(1), (1998).

[35] R. Sear and D. Frenkel. "Continuous Freezing in Three Dimensions". *Phys. Rev. Lett.*, **90**(19), 2003.

[36] M. N. Rosenbluth and A. W. Rosenbluth. "Further Results on Monte Carlo equations of state". *Journal of Chemical Physics*, **22**(881), (1954).

[37] W. W. Wood and J. D. Jacobsen. "Preliminary results from a recalculation of the monte carlo equation of state of hard spheres". *The Journal of Chemical Physics*, **27**(1207), (1957).

[38] B. J. Alder and T. E. Wainwright. "Phase transition for hard sphere system". *J. Chem. Phys.*, **27**(1208), (1957).

[39] C. F. Curtiss J. O. Hirschfelder and R. B. Bird. *"Molecular Theory of Gasses and Liquids"*. John Wiley & Sons, inc., New York Chapman & Hall, Limited, London, (1954).

[40] L. F. Finney and L. Woodcock. "Renaissance of Bernal's random close packing and hypercritical line in the theory of liquids.". *J. of Phys. Condensed Matter*, **26**(463102), (2014).

[41] R. Roth and A. O Parry. "Drying in a Capped Capillary". *Mol. Phys.*, **109**(7-10), (2011).

[42] T. Kihara. *"Convex Molecules in Gaseous and Crystalline States."*. John Wiley & Sons, (1963).

[43] S. S. Chen and A. Kreglewski. "Applications of the Argumented van der Waals Theory of Fluids.: I. Pure Fluids.". *Ber. Bunsen-Ges. Phys. Chem.*, **81**(1048), (1977).

[44] T. Boublik. "Supercritical fluid extraction of solids. Statistical thermodynamics approach.". *J. Phys. Chem.*, **2**(91-95), (2000).

[45] P. C. Hemmer. "Fluid with several phase transitions.". *Phys. Rev. Lett.*, **24**(1284), (1970).

[46] I. Joung T. Steinbrecher and D. A. Case. "Soft-Core Potentials inThermodynamic Integration: Comparing One- and Two-Step Transformation". *Journal of Computational Chemistry*, **32(15)**(3253-63), (2011).

[47] H. M. Gibson and N. B. Wilding. "Metastable liquid-liquid coexistence and density anomalies in core-softened fluid.". *Phys. Rev. E*, **75**(061507), (2006).

[48] Brian Robert Martin. *"Particle Physics"*. Graham Shaw, (2008).

[49] J. S Rowlinson. *"On the Continuity of the Gaseous and Liquid States"*. Dover Phoenix Editions, (1988).

[50] J. E. Lennard-Jones. "On the Determination of Molecular Fields". *Proc. R. Soc. Long. A*, **106**(738), (1924).

[51] M.P. Tildesley Allen. *"Computer Simulations in Chemical Physics"*. Springer, (1992).

[52] D. M. Heyes and H. Okumura. "Some Physical Properties of the Weeks-Chandler-Andersen Fluid". *Francis*, **32**(01), (2006).

[53] D. Chandler J. D. Weeks and H. C. Andersen. "Role of repulsive forces in determining the equilibrium structure of simple liquids.". *J. Chem. Phys.*, **54**(5237), (1971).

[54] L. Holian and D. J. Evans. "Shear viscosities away from the melting line: A comparison of equilibrium and non equilibrium molecular dynamics.". *Chem. Phys.*, **78**(5147), (1983).

[55] W. G. Hoover. *"Smooth Particle Applied Mechanics: The State of the Art."*. World Scientific Publishing Co. Pte. Ltd., (2006).

[56] M. T. Calvet and H. A. J. Oonk. *"Equilibrium Between Phases of Matter, Phenomenology and Thermodynamics"*. Springer Netherlands, (2008).

[57] J. S. Rowlinson and B. Widom. *'Molecular Theory of Capillarity'*. Oxford:Clarendon Press, (1982).

[58] K. E. Gubbins. "The Role of Computer Simulation in Studying Fluid Phase Equilibria. *Molecular Simulation*, **2**(4-6), (1989).

[59] A. Z. Panagiotopoulos. "Direct Determination of Fluid Phase Equilibria by Simulation in the Gibbs Ensemble: A Review". *Molecular Simulation*, **9**(1), (1992).

[60] A. Z. Panagiotopoulos. "Monte Carlo methods for phase equilibria of fluids". *J. Phys.: Condens. Matter*, **12**(2000), (1998).

[61] J. Siepmann B. Chen and M. L. Klein. "Direct Gibbs Ensemble Monte Carlo Simulations for Solid-Vapour phase equilibria: Applications to the Lennard-Jonesium and Carbon Dioxide". *J. Phys. Chem. B*, **105**(40), (2001).

[62] D. A. Allan M. Dinpajooh, P. Bai and J. I. Siepmann. "Accurate and precise determination of critical properties from Gibbs ensemble Monte Carlo Simulations.". *J. Chem. Phys.*, **143**(114113), (2015).

[63] D. A. Kofke. "Direct evaluation of phase coexistence by molecular simulation via integration along the saturation line". *J. Chem. Phys.*, **98**(4149), (1993).

[64] M. Mehta and D. A. Kofke. "Coexistence diagrams of mixtures by molecular simulation". *Chem. Eng. Sci.*, **49**(16), (1994).

[65] I. R. McDonald and K. Singer. "Calculation of thermodynamic properties of liquid argon from Lennard-Jones parameters by Mote Carlo method.". *Discuss. Faraday Soc.*, **43**(40-49), (1967).

[66] W. W. Wood. "Monte Carlo Calculation for Hard Disks in the Isothermal-Isobaric Ensemble". *J. Chem. Phys.*, **48**(415), (1968).

[67] D. N. Card and J. P. Valleau. "Monte Carlo Study of the Thermodynamics of Electrolyte Solutions". *J. Chem. Phys.*, **52**(6232), (1970).

[68] J. A. Barker and D. Henderson. "What is "liquid"? Understanding the states of matter". *Rev. Mod. Phys.*, **48**(587), (1976).

[69] G. C. A. M. Mooij M. H. J. Hagen, E. J. Meijer and D. Frenkel. "Does C60 have a liquid phase?". *Nature*, **365**(6445), (1993).

[70] A. Cheng and M. L. Klein. "Prediction of the Phase Diagram of Rigid C_60 Molecules.". *Phys. Rev. Lett.*, **71**(8), (1993).

[71] Yunus A. Cengel. *"Thermodynamics An Engineering Approach" 4th Edition.* Mc Graw Hill, (2002).

[72] P. Perrot. *"A to Z of Thermodynamics".* Oxford University Press ISBN 978-0-856552-9, (1998).

[73] E. Claperyon. "Memoire sur la puissance motrice de la chaleur". *Jounal de l'Ecole Polytechnique*, **XVI**(153-90), (1834).

[74] R. A. Alberty R. J. Silbey and M. G. Bawendi. *"Physical Chemistry (4t edition)".* Wiley, (2004).

[75] H. W. Habgood and W. G. Schneider. "PVT measurements in the critical region of xenon". *Contribution from the Division of Pure Chemistry, National Council of Canada, Ottawa, Canada*, **N. R. C.**(3161), (1953).

[76] J. N. S. Redlich, Otto; Kwong. "On the Thermodynamics of Solutions". *Chem. Rev*, **44**(233-244), (1949).

[77] D. Y.; D. B. Peng. "A New Two-Constant Equation of State". *Industrial and Engineering Chemistry: Fundamentals*, **15**(59-64), (1976).

[78] R. Freze A. Peneloux, E. Rauzy. "A consistent Correction for Redlich-Kwong-Soave Volumes". *Fluid Phase Equilibria*, **8**(7-23), (1982).

[79] K.E. Gubbins W.G. Chapman and M. Radosz G. Jackson. "SAFT: Equation-of-State Solution Model for Associating Fluids". *Elsevier Science Publishers*, **52**(31-38), (1989).

[80] PJ. Whitehead SJ Mills G. Jackson AN. Burgess A. Gil-Villegas, A. Galindo. "Statistical associating fluid theory for chain molecules with attractive potentials of variable range.". *J. Chem. Phys.*, **106**(10), (1997).

[81] G. Sadowski J. Gross. "Perturbed-chain SAFT: An equation of state based on perturbation theory for chain molecules". *Industrial & engineering chemistry research*, **40**(4), (2001).

[82] Sadowski G. Gross J. "Application of the perturbed-chain SAFT equation of state to associating systems.". *Industrial & engineering chemistry research*, **41**(22), (2002).

[83] P. Uusi-Kyyny M. Saajanlehto and V. Alopaeus. "A modified continuous flow apparatus for gas solubility measurements at high pressure and temperature with camera system.". *Fluid Phase Equilibria*, **382**(150-7), (2014).

[84] Kamerlingh Onnes H. "Expression of state of gases and liquids by means of series". *KNAW Proceedings, 1901-1902, Amsterdam*, **125-147**(4), (1902).

[85] H. D. Ursell. "The evaluation of Gibbs' phase-integral for imperfect gases". *Proc. Cambridge Phil. Soc.*, **23**(685), (1927).

[86] V. Chaudhary C. Feng, A. J. Schultz and David Kofke. "Eight to sixteenth virial coefficients of the Lennard-Jones model". *J. Chem. Phys.*, **143**(044504), (2015).

[87] W. G. Hoover and A. G. De Rocco. "Sixth and Seventh Virial Coefficients for the Parallel Hard-Cube Model". *J. Chem. Phys.*, **36**(12), (2004).

[88] K. W. Kratky. "Equation of state of a hard-disk fluid. I. The virial expansion". *J. Chem. Phys.*, **69**(2251), (1978).

[89] D. Chandler and J. D. Weeks. "Equilibrium structure of simple liquids". *Phys. Rev. Lett.*, **25**(3), (1970).

[90] D. Chandler J. D. Weeks and H. C. Andersen. "Role of repulsive forces in determining the equilibrium structure of simple liquids". *J. Chem. Phys.*, **54**(12), (1971).

[91] Y. Song and E. A. Mason. "Statistical-mechanical theory of a new analytical equation of state". *J. Chem. Phys.*, **91**(7840), (1989).

[92] C. Braga and K. P. Travis. "A configurational temperature Nose-Hoover thermostat.". *J. Chem. Phys.*, **123**(134101), (2005).

[93] B. L. Holian and D. J. Evans. "Shear viscosities away from the melting line: A comparison of equilibrium and non equilibrium molecular dynamics". *J. Chem. Phys*, **78**(5147), (1983).

[94] B. Hafskjold and T. Ikeshoji. "Partial specific quantities computed by non equilibrium molecular dynamics". *Fluid Phase Equilibria*, **104**(173-184), (1995).

[95] K. Onnes and H. Crommelin. "The virial equation of state.". *Commun Phys Lab Leiden*, **120**(a), (1911).

[96] R. Clausius. "XVI. On a mechanical theorem applicable to heat.". *Ann. Phys.*, **141**(124), (1870).

[97] J. W. Tester and M. Modell. *"Thermodynamics and its applications"*. Prentice Hall, (1997).

[98] H. K. Kamerlingh. "New evidence for the rotation of the earth.". *Wolters*, **1**, (1879).

[99] J. Wisnak. "Heike Kamerlingh - The Virial Equation of State". *Indian Journal of Chemical Technology*, **10**(564-572), (2003).

[100] W. Hoover. *"Computational statistical mechanics"*. Elsevier, (2012).

[101] F. H. Ree and Wm. G. Hoover. "Fifth and Sixth Virial Coefficients for Hard Sphere and Hard Disks". *J. Chem. Phys.*, **40**(939), (2004).

[102] K. W. Kratky. "Fifth to tenth virial coefficients of a hard sphere fluid". *Physica*, **87**(A), (1976).

[103] J. A. Barker and J. J. Monaghan. "Virial Coefficients for Square-Well Potentials". *J. Chem. Phys*, **36**(2558), (1962).

[104] 1994-2019 The MathWorks Inc. *"Evaluating Goodness of Fit"*, (2018). Math-Works version R2018b, https://uk.mathworks.com/help/curvefit/evaluating-goodness-of-fit.html.

[105] R. H. Perry and D. W. Green. *"Perry's Chemical Engineers' Handbook"*. McGraw-Hill, (1984).

[106] O A. Guerrero, S. Bassi, and BM. Adalberto. "On Padé approximants to virial series". *J. of Chem. Phys.*, **129**(4), (2008).

[107] GA. Vliegenthart and H. NW. Lekkerkerker. "Predicting the gas–liquid critical point from the second virial coefficient". *J. Chem. Phys.*, **112**(12), (2000).

[108] J. A. Barker and D. Henderson. "Perturbation Theory and Equation of State for Fluids. II. A Successful Theory of Liquids.". *J. Chem. Phys.*, **47**(4714), (1967).

[109] R. W. Zwansig. "High-Temperature Equation of State by a perturbation Method. I. Non polar Gases.". *J. Chem. Phys.*, **22**(8), (1954).

[110] D. Levesque and L. Verlet. "Perturbation Theory and Equations of State for Fluids". *Phys. Rev.*, **182**(307), (1969).

[111] N. F. Carnahan and K. E. Starling. "Equation of State for Nonattracting Rigid Spheres". *J. Them. Phys.*, **51**(635), (1969).

[112] D. M. Heyes and J. G. Powles. "Thermodynamic, mechanical and transport properties of fluids with steeply repulsive potentials.". *Molecular Physics*, **95**(2), (1997).

[113] A. Trokhymchuk and D. Henderson. "Hard-sphere radial distribution function again". *J. Them. Phys.*, **123**(024501), (2005).

[114] E. A. Mason Y. Song and R. M. Stratt. "Why Does the Carnahan-Starling Equation Work So Well?". *J. Phys. Chem.*, **93**(6916-6919), (1989).

[115] A. Mulero F. Cuadros and W. Ahumada. "An extensive study of the Helmholtz free energy of Lennard-Jones fluids using WCA theory". *Thermochimia Acta*, **277**(85-105), (1996).

[116] D. Henderson. "Monte Carlo and perturbation theory studies of the equation of state of the two-dimensional Lennard-Jones fluid.". *Mol. Phys.*, **34**(301), (1977).

[117] M. Baus and J L. Colot. "Theoretical structure factors for hard-core fluids". *J. Chem. Phys.*, **84**(1050), (1986).

[118] K. Zhang. "On the Concept of Static Structure Factor". *arXiv*, (1606.03610), (2016).

[119] F. Lado. "Numerical Fourier transforms in one, two and three dimensions for liquid state calculations.". *Journal of Computational Physics*, **8**(3), (1971).

[120] C. M Colina and E. A. Müller. "Joule-Thomson Inversion curves by molecular simulation". *Molecular simulation*, **19**(237-246), (1997).

[121] D. M. Heyes and C. T. Llaguno. "Computer simulation and equation of state of the Boyle and inversion temperature of simple fluids.". *J. Chem. Phys.*, **168**(61-68), (1992).

[122] L. I. Kioupis and E. J. Maginn. "Pressure-enthalpy driven molecular dynamics for thermodynamic property calculation I. Methodology". *Fluid Phase Equilibria*, **200**(75-92), (2002).

[123] G. Arya L. I. Kioupis and E. J. Maginn. "Pressure-enthalpy driven molecular dynamics for property calculation II: applications". *Fluid Phase Equilibria*, **200**(93-110), (2002).

[124] H. C. Andersen. "Molecular dynamics simulations at constant pressure and/or temperature". *J. Chem. Phys.*, **72**(2384), (1980).

[125] J. M. Haile and H. W. Gaben. "Molecular dynamics simulations extended to various ensembles. I. Equilibrium properties in the isoenthalpic-isobaric ensemble.". *J. Chem. Phys.*, **73**(2412), (1980).

[126] W. G. Hoover. "Constant-pressure equations of motion". *Phys. Rev. A*, **34**(2499), (1986).

[127] D. J. Evans and G. P. Morriss. "The isothermal/isobaric molecular dynamics ensemble". *Physics Letters A*, **98**(8-9), (1983).

[128] J-C Wang and K. A. Fichthorn. "Achieving constant pressure in molecular-dynamics simulations with constraint methods.". *J. Chem. Phys.*, **109**(10138), (1998).

[129] D. Cardwell. *"From Watt to Clausius: the rise of thermodynamics in the early industrial age"*. Ithaka, N.Y. : Cornell Univ. Press, (1971).

[130] E. Mach. *"Principles of the theory of heat"*. D. Reidel Publishing Company, Holland, (1896).

[131] M. J. Moran and H. N. Shapiro. *"Fundamentals of Engineering Thermodynamics"*. John Wiley & Sons Ltd, The Atrium, Southern Gate, Chichester, (2006).

[132] A. T. A. M. De Waele. "Basics of Joule-Thomson Liquefaction and JT Cooling". *Journal of Low Temperature Physics*, **186**(385-403), (2007).

Appendices

A The Virial Equation of state from the Partition Function. Following the method by Ursell

The Boltzmann factor $W_N(\mathbf{r^N})$ can be expressed as a sum of products of the *U-functions* $U_l(\mathbf{r}^\lambda)$. The *U-functions* are defined as:

$$U_1(\mathbf{r_i}) = W_1(\mathbf{r}_i)$$

$$U_2(\mathbf{r}_i, \mathbf{r}_j) = W_2(\mathbf{r}_i, \mathbf{r}_j) - W_1(\mathbf{r}_i)W_2(\mathbf{r}_j)$$

$$U_3(\mathbf{r}_i, \mathbf{r}_j, \mathbf{r}_k) = W_3(\mathbf{r}_i, \mathbf{r}_j, \mathbf{r}_k) - W_2(\mathbf{r}_i, \mathbf{r}_j)W_1(\mathbf{r}_k) \qquad \text{(A.1)}$$

$$- W_2(\mathbf{r}_j, \mathbf{r}_k)W_1(\mathbf{r}_i) - W_2(\mathbf{r}_k, \mathbf{r}_i)W_1(\mathbf{r}_j)$$

$$+ 2W_1(\mathbf{r}_i)W_1(\mathbf{r}_j)W_1(\mathbf{r}_k)$$

The idea is that the sum of products of W-functions corresponds to the number of way N particles can be arranged. In front of all the terms is the coefficient $(-1)^{n-1}(n-1)!$, where n is the number of groups in the term. The Boltzmann factor for $N = 1, 2$ and 3 are

$$W_1(\mathbf{r}_i) = U_1(\mathbf{r}_i) = 1$$

$$W_2(\mathbf{r}_i, \mathbf{r}_j) = U_2(\mathbf{r}_i, \mathbf{r}_j) + U_1(\mathbf{r}_i)U_1(\mathbf{r}_j)$$

$$W_3(\mathbf{r}_i, \mathbf{r}_j, \mathbf{r}_k) = U_3(\mathbf{r}_i, \mathbf{r}_j, \mathbf{r}_k) + U_2(\mathbf{r}_i, \mathbf{r}_j)U_1(\mathbf{r}_k) \qquad \text{(A.2)}$$

$$+ U_2(\mathbf{r}_j, \mathbf{r}_k)U_1(\mathbf{r}_i) + U_2(\mathbf{r}_k, \mathbf{r}_i)U_1(\mathbf{r}_j)$$

$$U_1(\mathbf{r}_i)U_1(\mathbf{r}_j)U_1(\mathbf{r}_k)$$

which is identical to the relation in equation (A.1), except that in this case the constant is equal to 1. In general equation (A.2) may be written as:

$$W_N(\mathbf{r}^N) = \sum \prod U_l(\mathbf{r}^\lambda) \tag{A.3}$$

Note that the sum of products must be carried over all possibilities of arranging N number of particles in m_l groups of l particles. Considering a set of groups m_l and the relation in equation (A.3) the sum of all the terms is:

$$\prod_{l=1}^{N}(Vl!b_l)^{ml} \tag{A.4}$$

The number of terms are

$$N! \prod_{l=1}^{N} \frac{1}{(l!)^{m_l}m_l!} \tag{A.5}$$

Multiplying equations (A.4) and (A.5) and summing over all sets of m_l results in the configurational integral:

$$Q_N = \frac{1}{N!} \int W_N(\mathbf{r}^N)d\mathbf{r}^N = \sum \prod_{l=1}^{N}(Vb_l)^{m_l}/m_l! \tag{A.6}$$

The *cluster integral, b_l,* is

$$b_l = (Vl!)^{-1} \int_V U_l(\mathbf{r_1}, \mathbf{r_2}, \cdots, \mathbf{r_l})d\mathbf{r_1}d\mathbf{r_2}\cdots d_{\mathbf{r_l}} \tag{A.7}$$

B Random number generator basis of MC hit and miss algorithm

The basis of any Monte Carlo algorithm is a random number generator. This algorithm uses the random number generator is written by Hoover in FORTRAN [55].

```fortran
FUNCTION XRAN(IDUM)
IMPLICIT NONE
INTEGER, PARAMETER :: K4B = SELECTED_INT_KIND(9)
INTEGER(K4B), INTENT(INOUT) :: IDUM
REAL :: XRAN
INTEGER(K4B), PARAMETER :: IA = 16807, IM = 2147483647
INTEGER(K4B), PARAMETER :: IQ = 127773, IR = 2836
REAL, SAVE :: AM
INTEGER(K4B), SAVE :: IX = -1, IY = -1, K
IF(IDUM <= 0. .OR. IY < 0) THEN   !initialise
    AM = NEAREST(1.0, -1.0)/IM
    IY = IOR(IEOR(888889999,ABS(IDUM)),1)
    IX = IEOR(777755555, ABS(IDUM))
    IDUM = ABS(IDUM) + 1
END IF
IX = IEOR(IX, ISHFT(IX,13))
IX = IEOR(IX, ISHFT(IX,-17))
IX = IEOR(IX, ISHFT(IX,5))
K = IY/IQ
IY = IA*(IY - K*IQ) - IR*K
IF(IY < 0) IY = IY + IM
XRAN = AM*IOR(IAND(IM,IEOR(IX,IY)),1)
END FUNCTION XRAN
```

C Relation between $S(k)$ and $g_0(r)$ in 3D

This derivation is repeated from "Theory of Simple liquids" (2nd edition p. 98). The radial distribution function is given by

$$\rho g_0(\mathbf{r}) = \frac{1}{(2\pi)^3} \int \exp(i\mathbf{k} \cdot \mathbf{r}[S(\mathbf{k}) - 1]) \tag{C.1}$$

If the system is isotropic, $S(\mathbf{k})$ is a function only dependent on the magnitude of the wavenumber $k = |\mathbf{k}|$.

$$S(k) = 1 + 2\pi\rho \int r^2 g_0(r) \int_{-1}^{1} \exp(-ikr\cos(\Theta))d(cos(\theta))$$
$$= 1 + 4\pi\rho \int r^2 g_0(r) \frac{sin(kr)}{kr} dr \tag{C.2}$$

This relationship is in cartesian coordinates. For this work, the relationship is required in spherical polars. Therefore, let $\mathbf{k} \cdot \mathbf{r} = kr\cos\Theta$ and $e^{i\mathbf{k} \cdot \mathbf{r}} = e^{ikr\cos\theta}$. Translating equation (C.1) into

$$\rho g_0(\mathbf{r}) = \frac{1}{(2\pi)^3} \int_0^\infty \int_{-1}^{+1} \int_0^{2\pi} \exp(i\mathbf{k} \cdot \mathbf{r})[S(\mathbf{k}) - 1]k^2 d(\cos\Phi)dkd\phi$$
$$= \frac{1}{(2\pi)^3} \int_0^\infty [S(k) - 1]k^2 \int_{-1}^{+1} \exp(ikr\cos\Theta)dk \tag{C.3}$$

The second integral can be written as

$$\int_{+1}^{-1} \exp(ikr\cos\Theta)d(\cos\Theta) = \left[\frac{1}{ikr} \exp(ikr\cos\Theta) \right]_{+1}^{-1} = \frac{e^{ikr} - e^{-ikr}}{ikr} \tag{C.4}$$

resulting in the radial distribution function expressed in spherical coordinates

$$\rho g_0(r) = \frac{2}{(2\pi)^2} \int_0^\infty [S(k) - 1]k^2 \frac{\sin(kr)}{kr} dk \tag{C.5}$$

D   The VdW equation and its inversion curve

In this appendix we derive an analytical expression for the Joule-Thomson inversion curve from the VdW equation of state. In molecular units, the VdW EoS is given by

$$P = \frac{Nk_BT}{V - Nb} - \frac{N^2a}{V} \tag{D.1}$$

By integrating equation (D.1) the energy of a VdW gas is obtained

$$E = \frac{3Nk_BT}{2} - \frac{N^2a}{V} \tag{D.2}$$

The critical temperature follows from solving the pair of equations

$$\left(\frac{\partial p}{\partial V}\right)_T = \left(\frac{\partial^2 p}{\partial V^2}\right)_T = 0 \tag{D.3}$$

The solutions are

$$k_BT_c = \frac{8a}{27b}$$
$$V_c = 3Nb \tag{D.4}$$
$$p_c2 = \frac{a}{27b^2}.$$

By introducing dimensionless variables, $T_r = T/T_c$, $P_r = P/P_c$ and $V_r = V/V_c$. the dependence of the VdW equation on a and b can be removed, yielding a universal VdW equation.

$$k_BT = \frac{T_r8a}{27b} \quad ; \quad p = \frac{p_ra}{27b^2} \quad ; \quad V = V_r3bN \tag{D.5}$$

$$P_r = \frac{8T_r}{3V_r - 1} - \frac{3}{V_r^2} \tag{D.6}$$

A similar non-dimensionalisation of the energy yields

$$E_r = 4T_r - \frac{3}{V_r} \tag{D.7}$$

Since the enthalpy is $H = E + PV$ it can be written in reduced units as

$$H_r = \frac{4T_r(5V_r - 1)}{(3V_r - 1)} - \frac{6}{V_r} \tag{D.8}$$

$$T\left(\frac{\partial p}{\partial T}\right)_V + V\left(\frac{\partial \rho}{\partial V}\right)_T = 0 \tag{D.9}$$

$$\left(\frac{\partial p}{\partial T}\right)_V = \frac{8}{3V - 1} \tag{D.10}$$

$$\left(\frac{\partial p}{\partial V}\right)_T = -\frac{-24T}{(3V - 1)^2} + \frac{6}{V^3} \tag{D.11}$$

Solving for the reduced temperature T_r gives a parabolic dependence on volume.

$$T = \frac{3}{4}\left(\frac{(3V - 1)}{V}\right)^2 \tag{D.12}$$

However, in order to produce an inversion curve, temperature as a function of pressure is required. By combining equations (D.6) and (D.12)

$$T = \frac{3}{4}\left[1 \pm \frac{(9 - P_r)^{1/2}}{6}\right] \tag{D.13}$$

In figure D.1, a VdW inversion curve is shown, using equation (D.13). It is displayed along with associated isenthalps, so it can be seen that the inversion curve passes through their maxima.
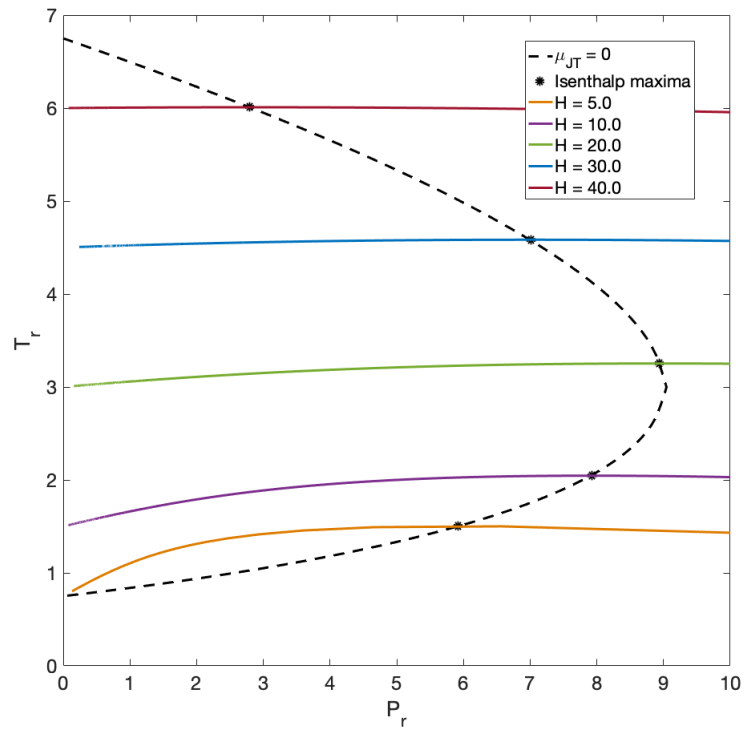
Figure D.1: The VdW inversion curve (broken line), shown with a handful of isenthalps H = [5.0; 10.0; 20.0; 30.0; 40.0] and their maxima (star). It is clear that the inversion curve goes through the maxima of the isenthalps.